



**POLITECNICO**  
MILANO 1863

SCUOLA DI INGEGNERIA INDUSTRIALE  
E DELL'INFORMAZIONE

# High-Fidelity Star Simulator for Cameras and Star Trackers

TESI DI LAUREA MAGISTRALE IN  
SPACE ENGINEERING - INGEGNERIA SPAZIALE

Author: **Davide Gravina**

Student ID: 10570605

Advisor: Prof. Paolo Panicucci

Co-advisors: PhD. Mattia Pugliatti, Prof. Francesco Topputo

Academic Year: 2022-23



# Abstract

The adoption of star trackers is now extending to small satellites and CubeSat, thanks to their capability for high-precision attitude determination and compact size. Considering that over this decade the launches of small satellites will increase to 2500 per year, a need arises to research and develop new star trackers to meet the specific design requirements of this kind of satellite. The specifics of these new devices are characterized by the trend to implement multipurpose cameras qualified to perform accurate attitude determination and efficient scientific space observation. Therefore, it is necessary to develop new tools to accelerate and improve the research in design procedures and algorithms training, which are needed to meet the multipurpose requirements, that represent a trade-off between the attitude determination performance and the specific space observation demand. In star tracker research three methodologies are employed to obtain these results: digital simulation, hardware-in-the-loop simulation, and field testing of star observation. Consequently, the development of star image simulation software becomes imperative to accurately replicate the real-space environment and diverse configurations of star sensors. This thesis focuses on developing a high-fidelity star simulation software capable of fulfilling this new research branch. In particular, an accurate simulation model for the brightness of the stars in the image signal, which considers the colour index and differentiates the spectral class of stars through the black-body theory, is introduced. Additionally, the simulation is completed with a reliable model of the most significant camera noises, such as source, temporal, position, fixed pattern, and environmental background noises. The results show that the developed simulator can generate detailed star images with high versatility in testing different parameters of cameras and simulated background conditions. The final step of this work is the study of the comparison between this high-detailed model, called Discrete Gray Scale (DGS), what respect to the most common simplified model, called Average Gray Scale (AGS).

**Keywords:** star tracker; image simulator; star simulator; star map simulator; camera; satellite; attitude determination; multipurpose camera; space observation;



## Abstract in lingua italiana

L'adozione di star tracker negli ultimi anni si sta estendendo anche ai CubeSat e Small-Sat, grazie alle dimensioni compatte e alla loro capacità di determinare l'assetto con elevata precisione. Si prevede che in questo decennio i lanci di piccoli satelliti aumenteranno fino a raggiungere i 2500 all'anno. Quindi, nasce l'esigenza di ricercare e sviluppare nuovi strumenti per accelerare e migliorare la ricerca sulle procedure di progettazione e sull'allenamento degli algoritmi necessari. In particolare, questi nuovi star tracker hanno la tendenza di implementare camere multifunzioni in grado di lavorare sia come star tracker che come camere per osservazioni scientifiche. Di conseguenza, i requisiti per queste camere multiuso devono essere un compromesso tra le prestazioni di misurazione e quelle di osservazione. Nello specifico, per la ricerca sugli star tracker vengono impiegate tre metodologie: la simulazione digitale, la simulazione hardware-in-the-loop e test in ambientazione reale. Di conseguenza, lo sviluppo di un software di simulazione delle immagini stellari diventa imperativo per replicare accuratamente l'ambiente spaziale e le diverse configurazioni possibili per le fotocamere. Questa tesi si concentra sullo sviluppo di un software di simulatore stellare ad alta fedeltà in grado di seguire questa nuova tendenza di ricerca. In particolare, viene introdotto un modello di simulazione accurato per la luminosità delle stelle nel segnale dell'immagine, che considera l'indice di colore e differenza per la classe spettrale delle stelle simulate. Inoltre, la simulazione è completata da un modello affidabile dei rumori più significativi delle camere, come i rumori di sorgente, temporali, di posizione, i fixed pattern e lo scenario ambientale. I risultati dimostrano che il simulatore sviluppato è in grado di generare immagini stellari dettagliate con un'elevata versatilità nel testare diversi parametri di camera e in svariate condizioni ambientali. Il risultato finale di questo lavoro è lo studio del confronto tra questo modello dettagliato, chiamato Discrete Gray Scale (DGS), e il modello semplificato più comunemente utilizzato, chiamato Average Gray Scale (AGS).

**Parole chiave:** star tracker; cercatore stellare; simulazione; simulatore di immagini stellari; stelle; fotocamera; satellite; fotocamere multifunzione; osservazioni spaziali;



# Contents

<b>Abstract</b>	<b>i</b>
<b>Abstract in lingua italiana</b>	<b>iii</b>
<b>Contents</b>	<b>v</b>
<b>List of Figures</b>	<b>vii</b>
<b>List of Tables</b>	<b>ix</b>
<b>1 Introduction</b>	<b>1</b>
<b>2 Theoretical knowledge and Parameters definition</b>	<b>5</b>
2.1 Structure of star map simulators . . . . .	5
2.2 Star Catalog Selection and Properties Evaluation . . . . .	7
2.3 Astrometric Parameters and Reference Systems . . . . .	14
2.3.1 Celestial Equatorial Frame . . . . .	14
2.3.2 Camera Body Frame . . . . .	15
2.3.3 Astrometric parameters procedure . . . . .	16
2.4 Photometric Parameters . . . . .	19
2.4.1 Johnson-Cousins UBVRI Filters . . . . .	21
2.4.2 Visual Apparent Magnitude and BV Index Color . . . . .	22
2.4.3 Calibration and Zero-Points . . . . .	22
<b>3 Simulator Models Description</b>	<b>25</b>
3.1 Characteristics of AGS and DGS model . . . . .	26
3.2 Black-body model of stars and Irradiance determination . . . . .	28
3.3 Black-body Temperature from B-V index color . . . . .	32
3.4 Determination of Zero-Point Reference . . . . .	36
3.5 Models Procedure . . . . .	37
<b>4 Camera Model</b>	<b>39</b>

4.1	Pixel Coordinate Projection . . . . .	39
4.1.1	Perspective Projection . . . . .	39
4.1.2	Weak-Perspective Projection . . . . .	42
4.1.3	Star selection in the Field of View . . . . .	43
4.2	Point Spread Function . . . . .	45
4.2.1	PSF Model . . . . .	46
4.2.2	Calibration of PSF parameters . . . . .	47
4.3	Camera Noises . . . . .	49
4.3.1	Photon Shot Noise . . . . .	51
4.3.2	Dark Signal Noise . . . . .	54
4.3.3	Non-Uniformity Noises . . . . .	57
4.3.4	Quantization Noise . . . . .	59
4.3.5	Read-Out Noise . . . . .	61
4.3.6	Application of noise models . . . . .	62
<b>5</b>	<b>Presentation of results</b>	<b>65</b>
5.1	First Output Simulation . . . . .	68
5.2	Second Output Simulation . . . . .	73
5.3	Third Output Simulation . . . . .	78
5.4	Analysis of Results . . . . .	85
<b>6</b>	<b>Conclusions and future developments</b>	<b>91</b>
6.1	Final Considerations . . . . .	91
6.2	Future Works . . . . .	92
	<b>Bibliography</b>	<b>95</b>



# List of Figures

2.1	Typical star image simulator workflow. . . . .	6
2.2	Hipparcos number of observed stars. . . . .	8
2.3	Catalog accuracy data of $BV$ index. . . . .	10
2.4	Catalog accuracy data of Right Ascension. . . . .	10
2.5	Catalog accuracy data of Declination. . . . .	11
2.6	Catalog accuracy data of Parallax. . . . .	11
2.7	Catalog accuracy data of Right Ascension Progress Motion. . . . .	12
2.8	Catalog accuracy data of Declination Progress Motion. . . . .	12
2.9	Vernal Equinox representation. . . . .	15
2.10	Camera Body Frame representation . . . . .	16
2.11	Reference frames of stars position vectors . . . . .	18
2.12	Johnson-Cousins UBVRI photometric filters. . . . .	21
2.13	Vega spectrum in linear and logarithmic scales . . . . .	23
3.1	Sun observed spectrum with black-body comparison. . . . .	29
3.2	Johnson V Photometric filter. . . . .	31
3.3	Spectral radiation Emittance of stars for black-body model. . . . .	33
3.4	Spectral radiation Emittance of stars in the B and V bands. . . . .	34
3.5	Stellar spectral class relationship of $BV$ index and Temperature. . . . .	35
3.6	Comparison between models of $BV$ - Star Temperature relation. . . . .	35
3.7	Vega observed spectrum with black-body comparison . . . . .	36
4.1	Pinhole camera model. . . . .	40
4.2	Perspective projection model. . . . .	41
4.3	Weak-Perspective projection model. . . . .	43
4.4	Camera Field of Views computations. . . . .	44
4.5	Stars Field of View detection procedure. . . . .	45
4.6	Gaussian Point Spread Function model. . . . .	46
4.7	Gaussian Point Spread Function for $\sigma = 0.55$ . . . . .	48
4.8	Gaussian Point Spread Function for $\sigma = 1.00$ . . . . .	48

4.9	Gaussian Point Spread Function for asymmetrical $\sigma$ .	49
4.10	Typical imaging process workflow.	50
4.11	Background light noises in near-Earth orbits.	54
4.12	Dark signal noise of CCD47-20 sensor.	56
4.13	Typical pattern DSNU noise for CCD and CMOS sensors.	58
4.14	An ideal 3 bit A/D converter.	60
4.15	Read-Out noise for CCD47-20.	61
5.1	Spectral Quantum Efficiency of CCD47-20	66
5.2	Spectral Transmissivity of BK-7 optical glass.	67
5.3	Centroid star coordinates of First image simulation.	69
5.4	Visual apparent magnitude parameters of First image simulation.	70
5.5	Effective surface temperatures parameters of First image simulation.	70
5.6	Simulated images without noises modelling of First output.	71
5.7	Simulated images with noises modelling of First output.	72
5.8	Centroid star coordinates of Second image simulation.	74
5.9	Visual apparent magnitude parameters of Second image simulation.	75
5.10	Effective surface temperatures parameters of Second image simulation.	75
5.11	Simulated images without noises modelling of Second output.	76
5.12	Simulated images with noises modelling of Second output.	77
5.14	Centroid star coordinates of Third image simulation.	81
5.15	Visual apparent magnitude parameters of Third image simulation.	81
5.16	Effective surface temperatures parameters of Third image simulation.	82
5.17	Real images of ROSETTA mission ( <i>ROS, CAM1, 20140513T202033C</i> ).	83
5.18	Simulated images of ROSETTA mission.	84
5.19	Comparison between DGS and AGS models for CCD48-20	86
5.20	Spectral radiation Emittance of stars for DGS model.	87
5.21	Spectral Quantum Efficiency of KAI4021	89
5.22	Comparison between DGS and AGS models for KAI4021	89

## List of Tables

2.1	Star parameters extracted from the catalog. . . . .	9
2.2	Hipparcos catalog photometric data origin. . . . .	9
2.3	Results of the catalog parameter accuracy analysis. . . . .	13
2.4	Angular directions of camera pointing. . . . .	18
2.5	Zero-Points of Johnson UBVRI photometric filters. . . . .	24
2.6	Zero-Points of bolometric magnitudes. . . . .	24
4.1	Summary table of camera noise models. . . . .	63
4.2	Noise values computed from camera datasheet (CCD47-20). . . . .	64
5.1	Fixed camera parameters. . . . .	66
5.2	Variable camera models parameters for First image simulation. . . . .	68
5.3	Variable camera models parameters for Second image simulation. . . . .	73
5.4	Variable camera models parameters for Third image simulation. . . . .	79



# 1 | Introduction

During the next decade, the already high number of satellites launched yearly will increase, reaching an average value of 2500 satellites annually. However, this number is mainly due to the new trend in the space industry to miniaturize satellites and use them coordinated, thanks to constellations. The reason behind this miniaturization is attributable to the decrease in costs of developing and manufacturing small satellites. These trends lead to the demand for decreasing the costs of instruments, sensors, and development for satellites [78]. Thus, this is followed by a further inclination to implement multipurpose cameras qualified to perform accurate attitude determination and efficient scientific space observation.

For these reasons, it is essential to develop new methodologies to test and develop these camera sensors and star trackers more cheaply. Generally, star trackers are optical devices capable of determining the attitude of a satellite through the images of the star field observable by the sensor. The attitude estimation accuracy of these sensors is highly dependent on the accuracy of camera calibration and the performance of the algorithms [11], both of which demand strict requirements to ensure the quality of the results. However, the implementation of multipurpose cameras is guided by different requirements that must represent a trade-off between the attitude determination performance and the specific space observation demand. Therefore, it is necessary to develop new tools to accelerate and improve the research in design procedures and algorithms training, which are needed to design these new devices. Consequently, for algorithm training and to perform a camera design capable of adapting the instrument to these new features, several tests of the possible outcomes these devices may experience are essential. These tests can be performed using images produced by optical instruments, night-sky experiments, or star image simulators. These outputs are then implemented throughout Optical Ground Support Equipment (*OGSE*) to perform a high-quality test [59]. Thus, the importance of star image simulators arises when a large number of possible requirements need to be tested to evaluate the best trade-off between several usage scenarios.

The star image simulators are developed following different methods in order to simulate some details rather than others; in particular, the main categories are, as stated in refer-

ence [33], the star map display method, the dynamic star map simulation method, and the blurred star map simulation methods. Mainly, star image simulators need to follow always the same fundamental steps in detail: Celestial Sphere Rotation, Camera Matrix projection, and Point Spread Function [65], which have a different level of detail based on the type of simulator we want to focus on. Thus, in order to perform these steps, the development of simulators has fundamental features that are:

- Catalogue selection;
- Camera Matrix Projection;
- Camera Detector Simulation.

For the first step, it is often preferred to use the Hipparcos Catalog [60]. This catalogue contains 118.218 stars with apparent magnitudes of up to 12. Moreover, it is one of the first complete catalogs made with satellite observations and published in 1997. However, newer catalogs obtained with more recent space missions contain almost 2 billion stars and celestial objects. Thus, the catalog selection is a trade-off between the level of complexity introduced and the computational time required. In fact, a large catalog introduces a high level of sources and parameters that require more time to be analyzed.

Instead, the second step regarding ‘Camera Matrix Projection’ is composed of two mathematical computations, the first regarding the transformation from the catalog frame to the camera frame; the second regarding the transformation from camera frame to image frame, which is characterized by the features of the camera system, in particular sensor and optical parts [11]. This step is crucial because it represents how the camera sees the real world; hence, it is fundamental for simulating star field scenarios, like the dynamic or the blurred ones.

Finally, the third step of the simulator regards how the camera detector retrieves and delivers the information about the real world. Also, in this case, the camera’s features are strictly related to the results. This step is characterized by the photoelectric equation that converts the number of photons arriving on the sensor from the star to the electrons used to recover the greyscale signal value of the final image. Many possible photoelectric equations can be used to model a star map simulator. The most common is the Average Gray Scale (AGS) model [33], which uses the average value of the sensor quantum efficiency and light wavelength to simplify the computation of the results. It is worth pointing out that the level of approximation chosen to adopt in this step is strictly related to the quality of the final synthetic image. Finally, another important feature of the star image simulator is the capability to easily change the simulated scenario, from the night sky simulation on Earth to the satellite orbiting around the Moon. The different

scenarios are mainly characterized by different behaviours of the noises, which are caused by the camera and environmental conditions. The camera noises are all the noises that refer to the optical and electrical components of the camera system, specifically, Source noise, Temporal noise, Position noise, and Random noise. These noises are not standardized and behave differently for any camera system. They can be generally defined as: Photon shot noise, Photon shot non-uniformity (*PRNU*), Dark current noise, Dark signal non-uniformity (*DSNU*), Quantization noise (*ADC*), Readout noise, Temporal noise, Fixed-Pattern noise, Reset noise [51, 73]. Instead, the environmental noises are all the noises due to the environment where the instrument is working. They can be generally defined as, Background light, Zodiacal light (for space) or Sky glow (for atmospheric light), Stray light due to cosmic rays, nebulae or Sun, planets, and moons [51, 61].

After developing a precise model for star image simulation, validating the result obtained with the simulations is important. The typical way to test all the algorithms and the simulations relative to star trackers is to examine them with real data. Since the images of the star trackers equipped on current space missions are mainly confidential, the best choice falls on acquiring images of the night sky with a workstation made to perform an outdoor test. This approach enables the replication of environmental conditions, including atmospheric diffraction and light pollution, thereby facilitating a comparative analysis between simulated and actual images. This procedural method aligns with established practices as documented in References [33, 59, 64] for evaluating the aforementioned algorithms and simulation models.

In conclusion, this thesis explain the procedures and the technical knowledge necessary to describe the implemented high-fidelity star image simulator. In particular, it is developed a complex model for the stars brightness signal computation, which consider black-body approximations of the stellar spectrum and color index of stars to increase the accuracy of the simulation. Finally, it is implemented a complete, but general, model of cameras capable to adapt the image simulation to any possible camera devices. In fact, computation precision and simulation versatility are the two primary features of the star image simulator developed in this work. Thus, it is structured into several chapters:

- Chapter 2 provides technical knowledge of simulators environment and regarding the parameter needed for the implementation of the star image simulator developed in this work.
- Chapter 3 describes the physical knowledge that defines the procedures and the

approximations implemented for the realization of this simulator.

- Chapter 4 presents the model implemented to simulate the camera behaviour for the image simulation and describe the camera noise models introduced to increase the accuracy of the simulation.
- Chapter 5 shows the achievable results provided by the simulator and perform a comparative analysis of the simulation model, with a common one, to obtain useful information regarding the improvements and the accuracy provided by these new models.
- Chapter 6 finally conclude the work with some considerations regarding the effective capability of this simulator and provide the discussion of the suggested future works.





# 2 | Theoretical knowledge and Parameters definition

## 2.1. Structure of star map simulators

The star map simulator is an important device used to assist in the training and validation of star trackers and in general cameras for the space application. One of its best features is the flexibility to change the tested scenario, allowing it to easily test several possible conditions in the space environment.

Thanks to that flexibility, these simulators are preferred for several experiments and studies. In fact, since the environment is modeled starting from any astronomical data, it is possible to produce a performance assessment and test the theoretical limits of star trackers, and in general any camera, simulating faint celestial objects over a multiplicity of possible noises, errors, or specific environmental conditions. These conditions can be used to train algorithms under adverse or particular circumstances in order to select the appropriate strategy for any space mission. Thus, summing up these capabilities, a reliable star map simulation is used for any design phase to optimize the space mission's design and simulate the operations of a camera device during the different phases of the mission. Despite the versatility of the star map simulators, the logical workflow that these software follow is always the same, as reported in 2.1. Therefore, the main differences between different types of simulators are in selecting the inputs and implementing different models to simulate some features more thoroughly than others.

Thus, for the different types of star simulators that can be developed, a possible classification is: *star map display simulator* [35]; *dynamic star map simulator* [76, 80]; *blurred star map simulator* [75, 82]; and *mixed star map simulator* [81].

The *star map display* is a simulator by which the typical purpose is to maximize the reliability of the software reproduction in an LED test bench. This one should be capable of reproducing the brightness of the stars directly on the camera. Furthermore, it is usually implemented to test the optical features and behaviors of the camera device.

The *dynamic star map* is a simulator by which the typical purpose is to maximize the reliability of the software of reproducing the satellite, or other objects, dynamic movements, and rotations. This can be used to analyze the limits of the camera devices or the limits of the algorithms of star detection or centroid extraction of the star trackers.

The *blurred star map* is a simulator by which the typical purpose is to maximize the reliability of the blur simulation of the camera during the image acquisitions. This can be very important in the cases of low SNR or in general to test algorithms of denoising or image restorations.

Finally, the *mixed star map* is a simulator where different features are developed together in order to test the accuracy of combined effects of image acquisition or to simulate complex behaviors of star trackers.

It is worth pointing out that each category of star map simulator is optimized to study and test specific features of the star trackers and cameras' working principle. Therefore, the simulation and the accuracy of errors and noises of the process will be different based on which application they will be optimized for.

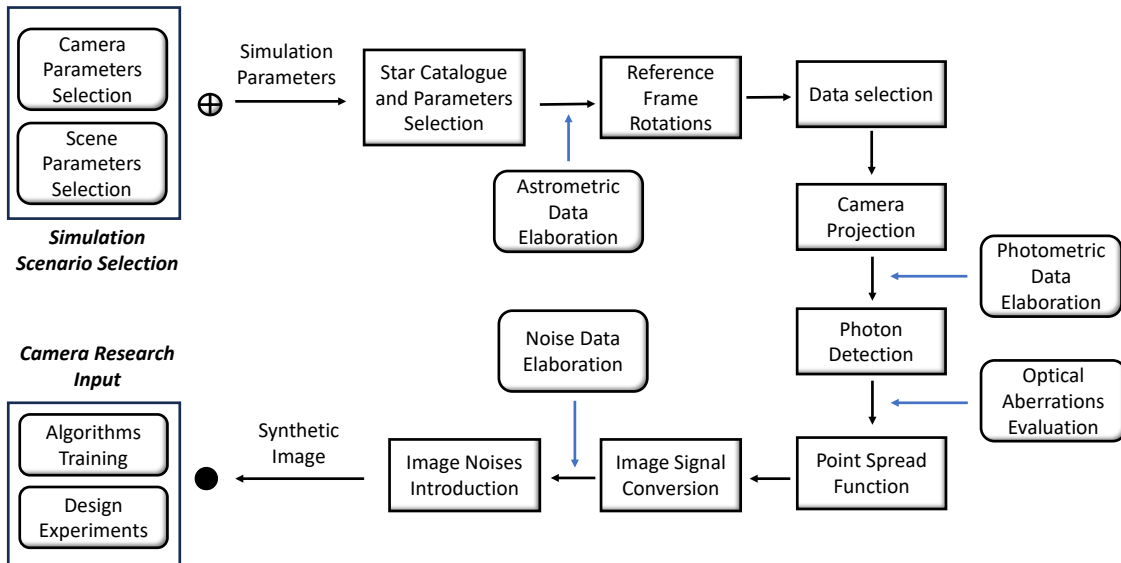


Figure 2.1: This figure schematize the typical Star Image Simulator working process. Note that the precision of the model could vary based on the type of simulator. The input and output results are freely chosen based on the desired usage conditions.

The simulator developed in this work follows the same logical workflow reported in the image 2.1 and can be classified as *mixed star map simulator*. In particular, it is optimized to simulate with detailed accuracy the photometric data of stars and the noises typical

of the entire camera system, from optical to sensor and electronic parts of the camera. A further specific feature is the model of astrometric data that also considers the proper motion of stars. Despite the precise simulation of these features, some others are not taken into consideration or less accurate since they were not the object of this thesis work. Some examples are the absence of galaxies and moon-planets systems and the static modeling of the images, so missing any dynamic behavior of the simulation.

It is worth underlining that the primary purpose of this work is to create a reliable baseline for the star map simulators that include high-precision models for star brightness and camera simulation. Additional features like dynamic motion and astronomical extra light sources can be modeled, starting from this simulator, based on the requirement of the specific application.

## 2.2. Star Catalog Selection and Properties Evaluation

The selection of an appropriate Star Catalog is fundamental for the implementation of a star image simulator. Star catalogs contain several stars information and are mainly characterized by three parameters: number of stars, information available, and accuracy of data. Therefore, considering these three parameters need to be selected the appropriate catalog for the desired application. In particular, the Star Catalog selected for this work is the HIPPARCOS Catalog [60], thanks to its properties that will be explained in this section.

The Hipparcos ESA's mission was a pioneering European project, launched in 1989, to retrieve astrometric information of many stars without interfering with the Earth's atmosphere. The mission's scientific goals were fulfilled throughout three years of optical observations of the entire sky. The measurements were performed with two instruments forming the HIPPARCOS and TYCHO catalogs, where the first one contains a lower amount of data, but with a higher precision, and the second contains many more sources information, but with a coarser precision. Note that the two catalogs have different precision and retrieve several information about the stars. In particular, the main instrument of Hipparcos's mission was an *Image dissector tube* to retrieve high accuracy astrometric values of the star, instead the secondary instrument was a *Photomultiplier tubes* to obtain mainly photometric values. Thus, the final version of the catalog collects data from the overall system and other experiments to maximize the data reliability [17].

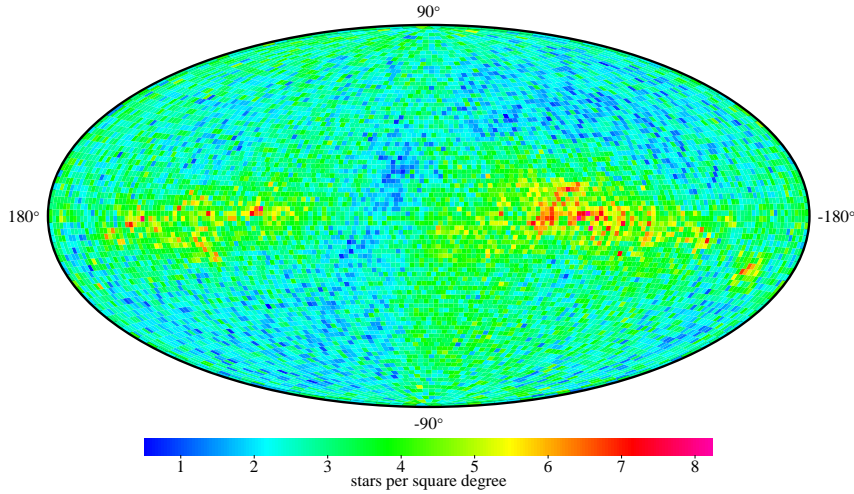


Figure 2.2: This figure show the Hipparcos observed number of stars per square degree for the entire sky. Source: figure acquired from [17].

Finally, the HIPPARCOS catalog contains the astrometric and photometric information of almost 118.218 stars<sup>1</sup>. The astrometric data of the stars are reported in the ICRS reference frame at the specific epoch J1991.25, outlined in the following section. While the photometric data of the stars are mainly reported in magnitudes, depending on the parameters. One noticeable feature of these data is that the catalog provides information on stars with apparent magnitude up to 12.4 mag.

The data collected by the star catalog for this work, as previously said, are divided into *Photometric Data* and *Astrometric Data*. In particular, the Photometric data, reported with type (P), and the Astrometric data, reported with type (A), used for the model are reported in table 2.1.

---

<sup>1</sup>Note that the catalog is missing information on some data due to non-stars sources, uncertain multiple-star systems, or unforeseen problems. In particular, the Astrometric values of 263 sources and the Photometric values of 1143 sources are missing. The real number of serviceable stars in the catalog is: 116.812 stars.

Type	Data	Symbol
(P)	Apparent Visual Magnitude	$m_v$
(P)	B-V index color	$BV$
(A)	Right Ascension	$RA$
(A)	Declination	$DEC$
(A)	Proper Motion in RA	$RA_{pm}$
(A)	Proper Motion in DEC	$DEC_{pm}$

Table 2.1: Star parameters extracted from the catalog.

It is worth mentioning that not all these values come from the main instrument of Hipparcos mission, so they can have different precision. In particular this is valid for the photometric data since the main instrument of Hipparcos's mission was optimized to obtain astrometric information of stars.

Hence, from the catalog is retrieved the origin of data and other helpful information that scholars can use to assess the reliability of parameters utilized. In table 2.2 are presented the origin of the photometric data of the catalog, instead in the figures 2.3, 2.4, 2.5, 2.6, 2.7, 2.8, indicate the accuracy data of the measurements in the catalog. Moreover, table 2.3 resumes the average evaluation of the parameter's errors.

Source	Visual Magnitude ( $m_v$ )	$BV$ index color
(Ground based Data) <sup>2</sup>	23139 sources	41205 sources
(Hipparcos Data)	94669 sources	0 sources
(Tycho Data)	409 sources	75732 sources

Table 2.2: Hipparcos catalog photometric data origin.

---

<sup>2</sup>The Ground Based information come from ground telescope measurement and from previous star catalog, like Yale Bright Star catalog.

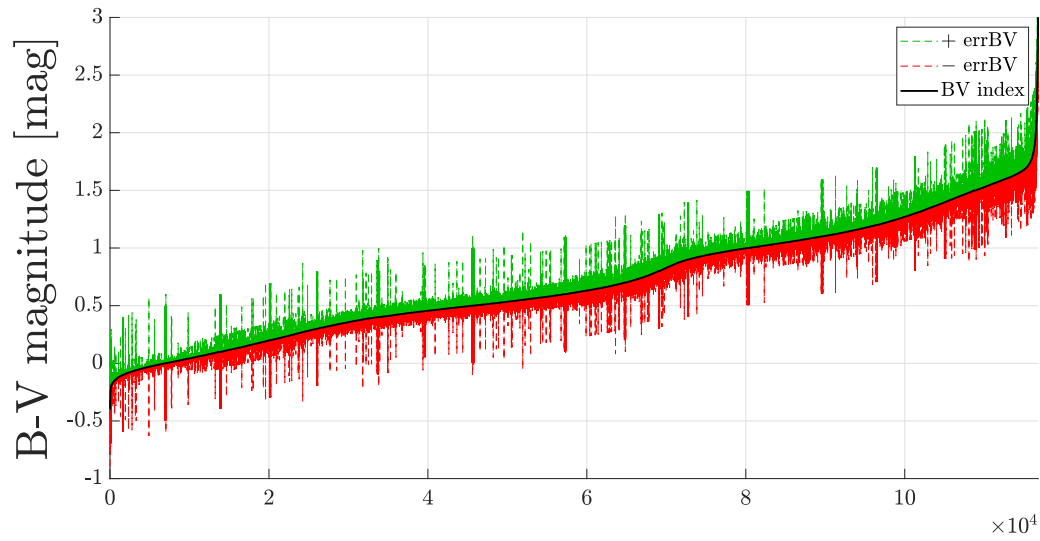


Figure 2.3: This figure shows the accuracy of catalog measurements regarding the stars  $BV$  index parameter.

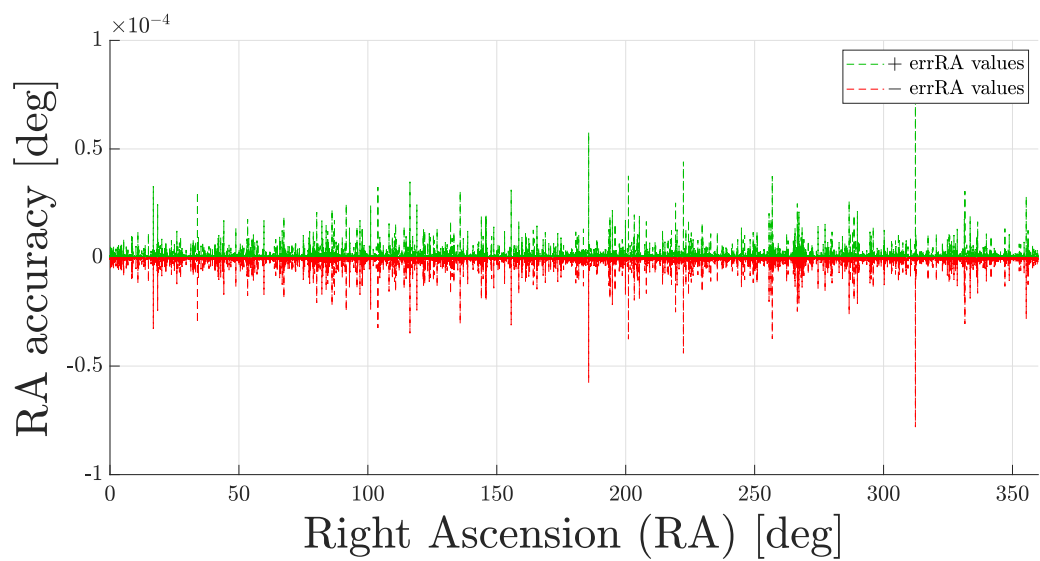


Figure 2.4: This figure shows the accuracy of catalog measurements regarding the stars Right Ascension parameter.

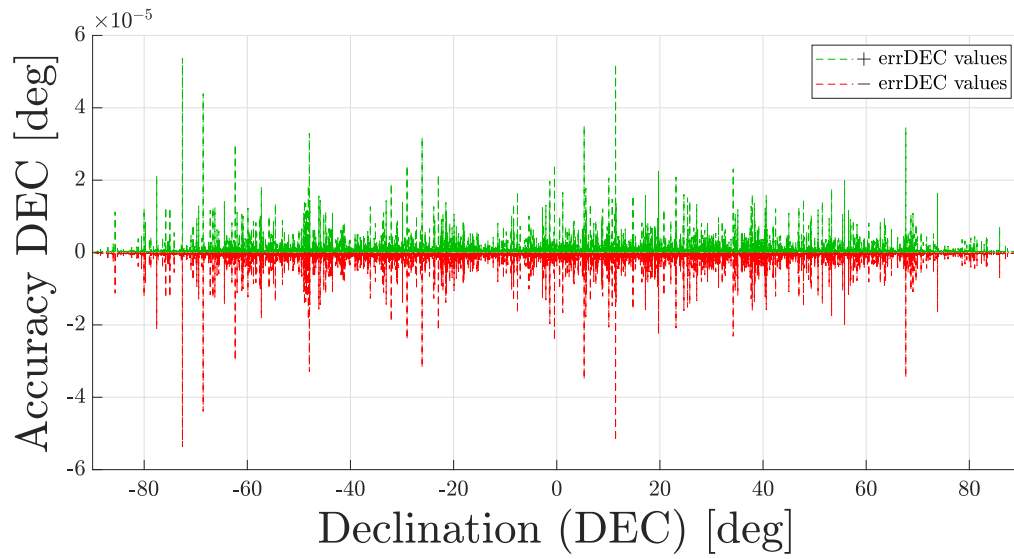


Figure 2.5: This figure shows the accuracy of catalog measurements regarding the stars Declination parameter.

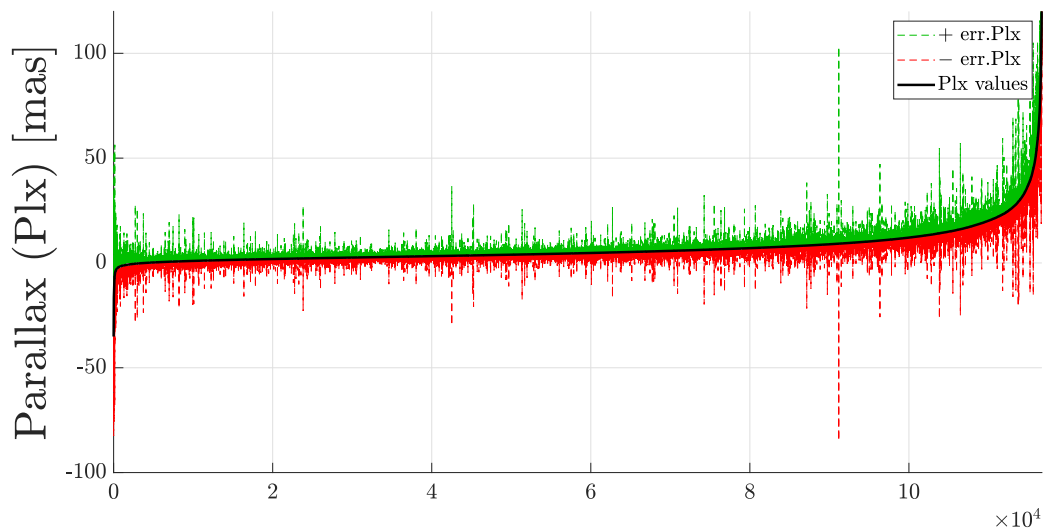


Figure 2.6: This figure shows the accuracy of catalog measurements regarding the stars Parallax parameter.



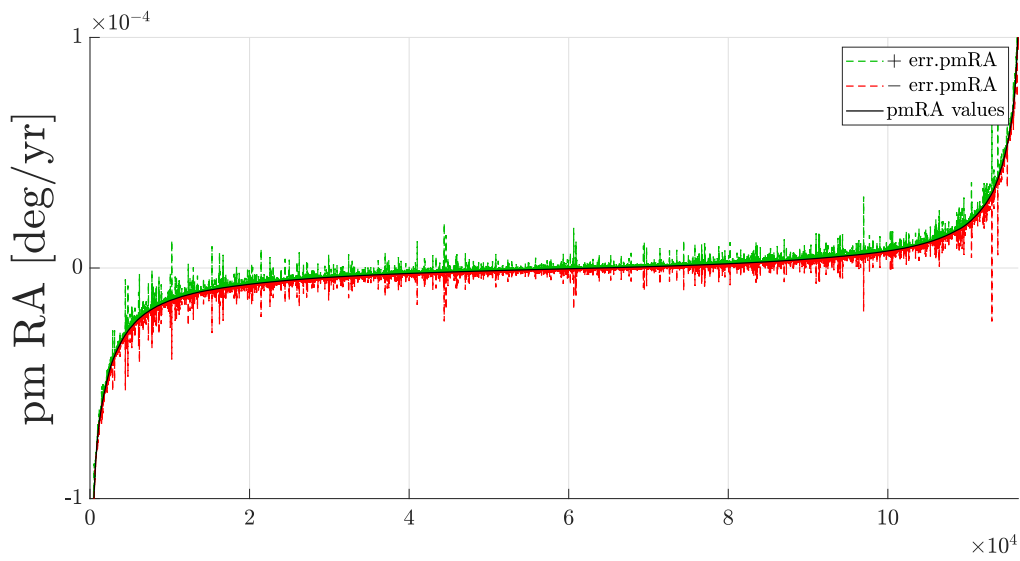


Figure 2.7: This figure shows the accuracy of catalog measurements regarding the stars Right Ascension Progress Motion parameter.

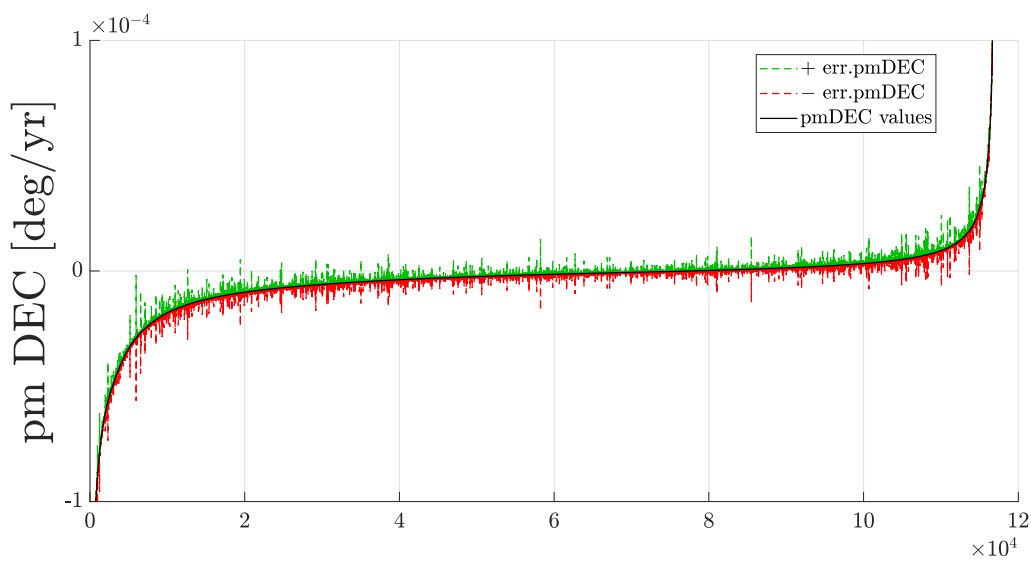


Figure 2.8: This figure shows the accuracy of catalog measurements regarding the stars Declination Progress Motion parameter.

Data	Accuracy Value
Mean BV mag.	0.0281 [ <i>mag</i> ]
Median Right Ascension	0.77 [ <i>mas</i> ]
Median Declination	0.64 [ <i>mas</i> ]
Median Parallax	0.97 [ <i>mas</i> ]
Median P.M. Right Ascension	0.88 [ <i>mas/yr</i> ]
Median P.M. Declination	0.74 [ <i>mas/yr</i> ]

**Table 2.3:** This table resume the accuracy analysis results of the catalog parameters. Where P.M. stands for Progress Motion. Others error analysis results are available in reference [60].

Note that the accuracy data evaluated in these figures are reported per unit measure, so it is possible to understand the behaviour of the error what respect the intensity of measurement. Another visualization option can be the spatial evaluation of accuracy values in the sky chart for every *RA* and *DEC* position. Thanks to the different results representation it is possible to assess whether the parameters suffer from particular error patterns for specific portions of the space. This last evaluation was performed through the data reported in ESA website [16]. Consequently, some measurement error patterns are identified, but the amount of the errors differences were estimated to be non-compromising for the final measurement, as reported in reference [18]. It is important to underline in regards to the error value of photometric data, in table 2.3, that these values are retrieved from a mean number of 110 photometric observations per star. However, the accuracy strictly depends on the conditions of each observed star. In fact, the median photometric precision for stars with  $H_p$  *apparent magnitude*<sup>3</sup> less than 9 mag is approximately 0.0015 mag, but note that for the natural variability of some particular stars' brightness, given by many factors, this value can grow up to an error greater than 0.6 mag.

Based on these outputs, the reliability and accuracy level of the catalog is then considered adequate for the aim of this work since the mean values of errors on the catalog are lower than the highest possible precision for real star sensors [23], and in general, for the majority of applications of a space camera.

In any case, a more accurate analysis on he reliability should be performed based on the desired application for which the image simulator wants meant to be applied.

---

<sup>3</sup>It is another system used to measure the apparent magnitude, very similar to the visual system, explained in Section 2.4.

## 2.3. Astrometric Parameters and Reference Systems

### 2.3.1. Celestial Equatorial Frame

This reference frame is an inertial reference frame usually adopted by catalogs to give a unique position information about stars; these values are expressed by two angles: Right Ascension (*RA*) and Declination (*DEC*).

Since the catalog used in this work is HIPPARCOS [60], the Celestial frame adopted is stated through the convention of the International Celestial Reference System<sup>4</sup> (*ICRS*). This model is defined from hundreds of extra-galactic radio sources, primarily quasars, distributed throughout space, and is derived at the reference epoch of J-2000. However, note that the data in the catalog are listed to a different epoch the J-1991.25<sup>5</sup>, since the measurements of the Hipparcos mission have been made during the years 1989-1993. Thus, the overall alignment of the catalog frame to the ICRS model at that epoch is estimated to be within 0.6 milliarcseconds, with any spurious rotation or distortion less than 0.25 milliarcsecond/year [52].

Specifically, the Hipparcos realization of the ICRS (International Celestial Reference System) is established with its origin at the center of mass of the Solar System. Its fundamental axes are defined in a manner that ensures backward compatibility with the traditional equatorial coordinate system known as the Fifth Fundamental Catalog (*FK5*), which astronomers have historically used, but with the equinox and poles of epoch J-2000.0. To better understand the definition of this inertial reference frame, as shown in figure 2.9, the x-axis is approximately aligned with the vernal equinox of the year 2000, which corresponds to the straight line originating from Earth and extending in the direction of the Sun during the spring equinox of March 2000. The z-axis is oriented nearly toward the north pole of the celestial sphere, and the y-axis is defined in a way that ensures the x, y, and z axes are a right-handed coordinate system.

---

<sup>4</sup>The ICRS adopted for the Hipparcos Catalog realization is not the latest one, since it updated periodically using the most recent measurements of the sky

<sup>5</sup>Means that the parameters reported are measured in a precise date, specifically in this catalog used the Julian days calendar and the epoch J-1991.25, that correspond to the 02 April 1991 at 12.00 am.

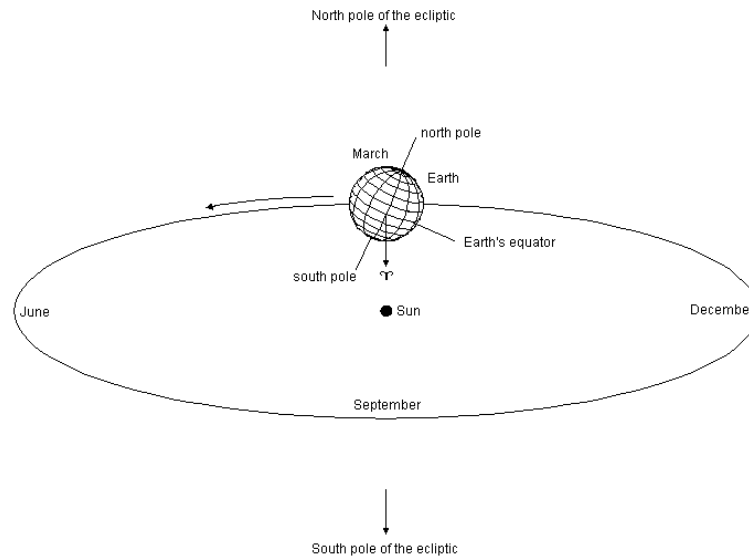


Figure 2.9: This figure show the Earth and Sun positions during the Vernal Equinox. Source: figure acquired from [22].

### 2.3.2. Camera Body Frame

The Body Fixed Frame of a satellite is the reference frame used to define the positions of the satellite components with respect to an origin that can be any point inside the spacecraft. Thus, the axis of this frame are fixed on the satellite toward three directions that define a right-handed coordinate system, and usually are aligned with the principal inertia axes of the satellite. Since the axes are fixed, they rotate with the satellite.

In our case, for simplicity, it is considered directly the Camera Body Frame, that is a body fixed frame with its origin in the star camera, or observation device, and the axis aligned with the device. In particular, the axes of this frame are aligned as in the figure 2.10, thus the x-axis and y-axis define the camera plane and the z-axis is pointed like the boresight direction of the observation.

Finally, this reference frame is serviceable to develop an easy conversion of the observed stars to the *Sensor Pixel Coordinates* of the simulated image, as described in section 4.

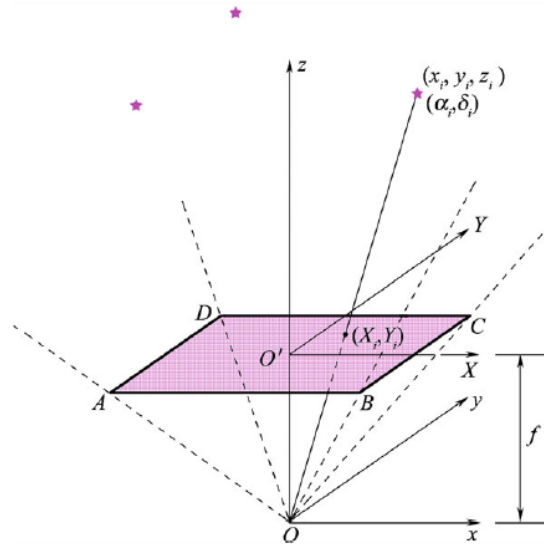


Figure 2.10: This figure represents the mathematical description of the Camera Body Frame, where the point (O) is the Center of Projection and the Purple Plane represent the Image Plane of the observation. Source: figure acquired from [30].

### 2.3.3. Astrometric parameters procedure

The Astrometric parameters are the 5 parameters by which it is possible to retrieve the information about position, movements and distance for any star, then the description of these data is well explained in the Hipparcos guide [18]. However, the employed parameters in this simulator are, as previously reported: *Right Ascension*, *Declination* and *Proper Motions* of stars. These data needs to be rotated to a precise Reference Frame that must be consistent with the operations of the simulator. In particular, RA and DEC are expression of the Celestial Equatorial Frame and are listed in the catalog using the International Celestial Reference System (ICRS) at the epoch of J-1991.25, as reported in [60]. Instead, the direction of the camera is reported in Camera Body Frame, but for simplicity it is selected from the boresight direction parameters in Celestial coordinates. The procedure followed in this work to align all the data to a unique reference frame is now reported:

- Retrieve RA, DEC and Proper Motions of stars, from the catalog, in the ICRS J-1991.25 Reference Frame.
- Provide the Proper Motion corrections to the RA and DEC catalog data, selecting

a data of the observation epoch, expressed in Julian calendar. In particular, for this work it has been selected the observation epoch ( $obs_{epoch}$ ): J-2000, then the correction is developed through these equations:

$$\begin{cases} RA_{corrected} = RA + pm_{RA} \cdot (obs_{epoch} - catalog_{epoch}) \\ DEC_{corrected} = DEC + pm_{DEC} \cdot (obs_{epoch} - catalog_{epoch}) \end{cases} \quad (2.1)$$

- Convert the spherical coordinates of the star's positions, expressed with RA and DEC, into Cartesian coordinates to provide a unitary direction vector of the position in the ICRS reference frame:

$$\begin{cases} x = \cos(DEC) \cdot \cos(RA) \\ y = \cos(DEC) \cdot \sin(RA) \\ z = \sin(DEC) \end{cases} \quad (2.2)$$

- Boresight direction of the camera, expressed through Right Ascension ( $\alpha_0$ ) and Declination ( $\delta_0$ ) spherical coordinates, in ICRS frame, are converted into Cartesian coordinates, using the equations 2.2. Then, it is possible to retrieve a subset of stars from the catalog choosing the parameter of the camera Field of View
- Rotation of the Celestial Reference Frame, so ICRS, to the Body Reference Frame, by which the directions of the camera can be described, through a rotation matrix expressed with Direction Cosine Matrices. This operation is needed to obtain the direction of stars with Cartesian coordinates in the Body Frame of the camera.

$$\mathbf{A}_1(\alpha) = \begin{bmatrix} 1 & 0 & 0 \\ 0 & \cos(\alpha) & -\sin(\alpha) \\ 0 & \sin(\alpha) & \cos(\alpha) \end{bmatrix} \quad \mathbf{A}_2(\alpha) = \begin{bmatrix} \cos(\alpha) & 0 & -\sin(\alpha) \\ 0 & 1 & 0 \\ \sin(\alpha) & 0 & \cos(\alpha) \end{bmatrix} \quad (2.3a)$$

$$\mathbf{A}_3(\alpha) = \begin{bmatrix} \cos(\alpha) & -\sin(\alpha) & 0 \\ \sin(\alpha) & \cos(\alpha) & 0 \\ 0 & 0 & 1 \end{bmatrix} \quad (2.3b)$$

$$\mathbf{A}_{313}(\alpha_1, \alpha_2, \alpha_3) = \mathbf{A}_3(\alpha_3) \cdot \mathbf{A}_1(\alpha_2) \cdot \mathbf{A}_3(\alpha_1) \quad (2.3c)$$

Note that equations 2.3, with the angles of rotation reported in the table, 2.4 expresses the rotation from the Camera Body Frame to the Celestial Frame, so  $\mathbf{A}_{313}$

must be transposed to define the desired rotation matrix. The results of these operations are shown in the figure 2.11.

Angle	Definition
$\alpha_1 = \phi_0$	Roll angle of the camera.
$\alpha_2 = \delta_0 - \frac{\pi}{2}$	Declination angle of the camera boresight, plus 90 deg.
$\alpha_3 = \alpha_0 - \frac{\pi}{2}$	Right Ascension angle of the camera boresight, minus 90 deg.

**Table 2.4:** This table shows the angles of Rotation Matrix from Camera Body Frame to Celestial Frame.

It is important to point out that this model takes into account only one type of correction on the position of stars: the proper motion correction. However, many other possible corrections can be implemented in order to increase the precision during observations, as reported in [47, 55]. Some examples are the *nutaton* and *precession* corrections of the Earth, or the *stellar aberration* of the light due to the velocity of the observer what respect the stars. Furthermore, this procedure is completed with the model of the camera, or the scenario, that is intended to simulate. In particular the model developed for this work are explained in the section 4 .

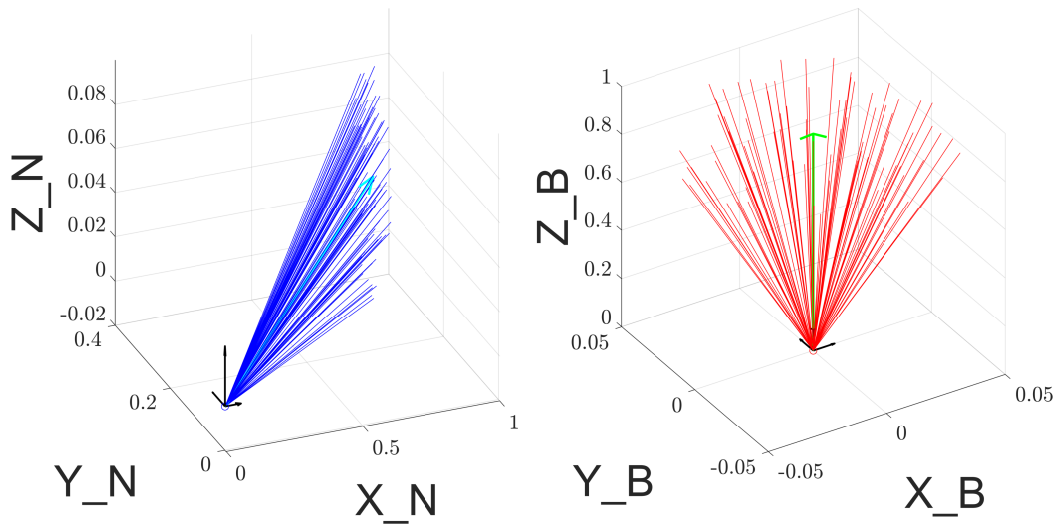


**Figure 2.11:** This figure shows the resulting stars position vector in both reference frame. On the left is represented the Celestial Frame (N), on the right is represented the Body Frame (B). Note that Celestial Frame represent the star directions in the catalog, instead Body Frame offers the vision from camera point of view.

## 2.4. Photometric Parameters

The Photometric parameters are all the parameters that measure the flux or the intensity radiated by astronomical objects, then the description of these data is well explained in section 1.3 of Hipparcos guide [18]. However, the employed parameters in this simulator, as previously reported, are: *Apparent Magnitude*, and *BV index color* of stars. Before explaining the procedure and the models of the parameters used, it is worth introducing a brief explanation of the different magnitudes measurements in order to avoid any ambiguity on the terms<sup>6</sup> used in this section.

### Apparent Magnitude

The measure of apparent magnitude ( $m$ ) of a celestial objects offer the information about brightness of the object as it appears when observed from Earth, above the atmosphere. This measurement describes the Flux Density, or Irradiance, of a celestial object, which strictly depends by their intrinsic luminosity, size, distance and any extinction of object's light caused by interstellar dust along the line of sight to the observer. Thus, this value, indicated with the unit of measure of *magnitude*, expresses in a reverse logarithmic scale a comparison between the brightness of an object ( $F_{obj}$ ) and a reference brightness ( $F_0$ ), stated as:

$$m_{obj} = m_0 - 2.5 \cdot \log_{10}\left(\frac{F_{obj}}{F_0}\right); \quad (2.4)$$

where ( $m_{obj}$ ) is the magnitude of the measured object, and ( $m_0$ ) is the magnitude of the reference object, usually set to 0. A more precise definition of the apparent magnitude states that the comparison between brightness is exploited within spectral flux densities, so Spectral Irradiances, explained through the concept of *Bolometric* and *Filtered Magnitude*.

### Absolute Magnitude

The measure of absolute magnitude ( $M$ ) of celestial objects offers almost the same information of apparent magnitude but it is scaled to indicate the relative Luminosity of stars. In fact, it is defined as the apparent magnitude that the objects would have if they were viewed from a fixed distance of 10 parsec, without considering any extinction process of light. The formula that defines this value is the following :

$$M_{obj} = m_{obj} - 5 \cdot \log_{10}\left(\frac{d}{10}\right); \quad (2.5)$$

---

<sup>6</sup>The following nomenclature is stated from SI radiometry units.



where ( $d$ ) is the real distance of the observed object, measured in *parsec*. Note that through this value it is possible to classify the celestial objects based on their luminosity, but the data of real distance of stars, with high reliability, are not easy to achieve.

## Bolometric Magnitude

The measure of bolometric magnitude takes into account spectral properties at all the wavelength of celestial objects, respectively spectral Irradiance ( $F_{obj}(\lambda)$ ) e spectral Luminosity ( $L_{obj}(\lambda)$ ) for apparent and absolute magnitudes. In particular, the first equation reports the *apparent bolometric magnitude* ( $m_{bolo}$ ) and *absolute bolometric magnitude* ( $M_{bolo}$ ) :

$$\begin{aligned} m_{bolo} &= m_{bolo,ref} - 2.5 \cdot \log_{10} \left( \frac{\int_0^{\infty} F_{obj}(\lambda) d\lambda}{F_{bolo,ref}} \right); \\ M_{bolo} &= M_{bolo,ref} - 2.5 \cdot \log_{10} \left( \frac{\int_0^{\infty} L_{obj}(\lambda) d\lambda}{L_{bolo,ref}} \right); \end{aligned} \quad (2.6)$$

where ( $M_{bolo,ref}$ ) and ( $L_{bolo,ref}(\lambda)$ ) are the absolute bolometric magnitude and the bolometric Luminosity of the reference object, ( $m_{bolo,ref}$ ) and ( $F_{bolo,ref}(\lambda)$ ) are the apparent bolometric magnitude and the bolometric Irradiance of the reference object; while the parameter of integration ( $\lambda$ ) is the light's wavelength. Note that the reference points for bolometric magnitudes is expressly regulated by IAU, from 2015, as reported in [56].

## Photometric Filtered Magnitude

The measure of filtered magnitude ( $m_x$ ) of celestial objects offers the information by specific intervals of the light's spectrum from the object. In particular, it extends the concepts of apparent and absolute magnitudes considering only limited portions of the spectrum given by a set of photometric filters, as opposed to bolometric properties that evaluate the entire spectrum. There are several photometric filters developed during the years for astronomy, all developed to measure or recreate specific properties of the objects. In particular, the creation of these filters starts with the use of photography for astronomical measurements, since the camera is capable of seeing the light in several ways, thus the different filters are useful to standardize the various measurements. In general, the filtered magnitude can be computed through the formulation :

$$m_x = m_{x,ref} - 2.5 \cdot \log_{10} \left( \frac{\int_0^{\infty} F_{obj}(\lambda) \cdot R_x(\lambda) d\lambda}{\int_0^{\infty} F_{ref}(\lambda) \cdot R_x(\lambda) d\lambda} \right); \quad (2.7)$$

where ( $m_{x,ref}$ ) is the magnitude of the reference developed with a general filter ( $R_x(\lambda)$ ).

It is worth pointing out that this category of magnitudes required the exploitation of the spectral properties of the simulated objects, otherwise it is necessary a simplification of the equation where it is considered an average value instead of the integration.

### 2.4.1. Johnson-Cousins UBVRI Filters

The Johnson-Morgan UBV wide-band system stands as the most extensively employed photometric system. Its inception dates back to the early 1950s, with the subsequent addition of the longer wavelength R and I bands as detailed in reference [9]. The B band was designed to approximate the unfiltered photographic magnitude (excluding the ultraviolet), while the V band was intended to approximate the visual magnitude system. The U band filled the crucial gap between B and the atmospheric cutoff wavelengths.

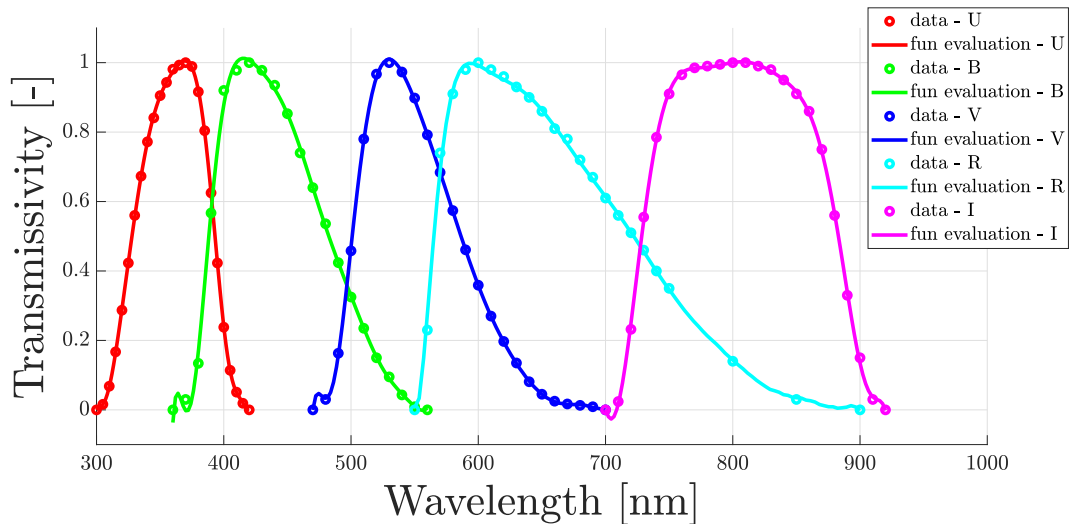


Figure 2.12: This figure shows all the photometric filters of the Johnson-Cousins UBVRI system. Source: functions evaluation of data retrieved from reference [7].

In particular, the UBVRI filters used in this work are retrieved through specific functions evaluation starting from the Bessel approximation, explained in [7], depicted in the figure 2.12. It is worth pointing out that Johnson's filters are not the exclusive ones, there are many other filters that are created to optimized to fit particular system or to measure several effects in the light's spectrum, some of them are reported in [9]. For example, Hipparcos photometric measurements are initially performed using the Hipparcos filter, denoted as  $Hp$ , that is a very broad filter with peak response between the V and B bands, this filter and the transformation procedures are described in detail in [8, 19].

### 2.4.2. Visual Apparent Magnitude and BV Index Color

Historically, star brightness was determined only by the human eye's perception and was consequently referred to as visual magnitude. Since the Johnson V filter simulates the eye's vision and is also more sensitive in the green wavelengths (550 nm), the photometric data of star's magnitude in the catalog are listed using this filter, thus are *visual apparent magnitudes*. This choice is prevalent among the star catalogs in fact, when no further information is given, any apparent magnitude is actually a visual magnitude ( $m_v$ ). In particular, this filter is applied using the equation 2.7 to the measurements of stellar Irradiance provided by the instruments.

The other parameter used is the BV index color corresponding to the subtraction of the two filtered magnitudes, with Johnson's B and V filters, as reported in equation 2.8. This operation is used to retrieve the characteristics of the spectrum of the celestial object, like the surface temperature. In fact, any celestial object emits light along the spectrum with a different peak wavelength of emission, mainly due to the surface temperature of the object. In the case of stars, this is represented by the categorization into spectral classes, which divide from stars in the main sequence to super-giant and dwarf stars.

$$B - V = m_B - m_V; \quad (2.8)$$

These filters are represented in the figure 2.12 instead, the procedure for the determining of the star surface temperature will be explained in the section 3.3.

### 2.4.3. Calibration and Zero-Points

The photometric calibration is the process of linking the brightness measurements made by a device to define the radiant, or spectral, flux of celestial objects. This process is usually strictly dependent on the parameters of each devices and offers specific measurements of the physical quantities that can hardly be replicated in a simulation. The Zero-points, conversely, offers a calibration reference point for specific photometric systems. These values represent the reference parameters by which the relations of the magnitude, as reported in section 2.4, can be determined for an observed object.

Historically, the magnitude system zero-point reference was based on Vega ( $\alpha Lyrae$ ) Spectrum, reported in figure 2.13, since it was readily observable in the northern hemisphere for a significant portion of the year, and it exhibited a relatively regular spectral energy distribution when compared to later-type stars. The main characteristics of Vega star are that the star own to the main sequence, in fact its spectral type is A0V, the effective

temperature is  $9602\text{ K}$ , the visual magnitude ( $m_v$ ) is  $0.03$  and the magnitude in any band (UBVRI) is approximately constant, so the Index colors, like  $B - V$ , are all equal to zero. In particular, the adoption of Vega as reference star is still used in Johnson-Cousins photometric systems. Then, the computation of zero-points for each filter can be computed starting from the flux of Vega, although the measurement of Vega spectrum may vary slightly due to the greater precision of the instruments during the years, or due to several effects if measured from the ground. Thus not all computations may have the same results and various solution are adopted during since now, as it is shown in table 2.5. Note that the reference zero-point computation adopted in this simulator is different, but expresses the same theoretical concept explained here and that will be explain in details in the section 3.4.

Other possible reference zero-points adopted for the magnitude computations are the bolometric ones. These points are conventionally estimated thanks to the International Astronomical Union (IAU), as reported in [56]. In particular, is needed two zero-points that specify the Luminosity and the Irradiance corresponding to the 0 magnitude bolometric reference source, these values are reported in table 2.6.

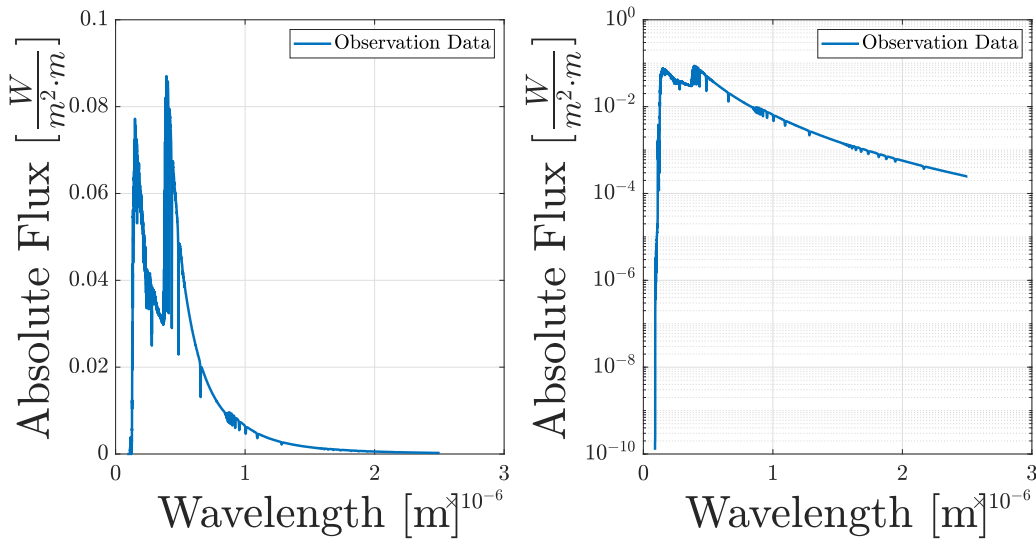


Figure 2.13: These figures show the observed Vega spectrum il linear scale, on the left, and in logarithmic scale, on the right. Source: Observation Data retrieved by reference [68].

Band	$\lambda_{eff}$ [ $\mu m$ ]	$Flux^*$ at 0 mag	$\lambda_{eff,2}$ [ $\mu m$ ]	$Flux_2^*$ at 0 mag
U	0.36	4.35e-9	0.366	4.175e-9
B	0.44	7.20e-9	0.438	6.32e-9
V	0.55	3.92e-9	0.545	3.631e-9
R	0.64	1.76e-9	0.641	2.177e-9
I	0.90	8.3e-10	0.798	1.126e-9

\* The unit of measure of the Spectral Flux Density reported here is:  $erg/(s\ cm^2\ \text{\AA})$ .

**Table 2.5:** This table shows the Zero-Points of Johnson UBVRI photometric filters. Note the difference between Johnson's calibration using Vega as a reference, as ( $Flux$ ); and Bessell's calibration utilizing a combination of Vega and Sirius spectra and slightly different filters shapes, as ( $Flux_2$ ). These values comes from the papers [48] and [10], respectively from H.Johnson and M.Bessel authors.

Band	$\lambda_{eff}$	Value	Formula
Apparent Bolometric	all	$F_0 = 2.518e-8 \left[ \frac{W}{m^{-2}} \right]$	$m_{bolo} = -2.5 \log_{10} \left( \frac{F_{obs}}{F_0} \right)$
Absolute Bolometric	all	$L_0 = 3.0128e28 [W]$	$M_{bolo} = -2.5 \log_{10} \left( \frac{L_{obs}}{L_0} \right)$

**Table 2.6:** This table shows the Zero-Points of bolometric magnitudes:  $L_0$  is a value of Luminosity for 0 *mag* source,  $F_0$  is a value of Irradiance for 0 *mag* source. The values observed ( $F_{obs}$ ,  $L_{obs}$ ) are intended as bolometric, so over all the wavelengths of the spectrum.



# 3 | Simulator Models Description

The star map simulator baseline developed in this work use a specific high-precision model for star brightness computation that is described in this chapter. As mentioned before, it follows the standard workflow of a star map simulator, reported in figure 2.1, that now will be explained with more details.

- Initially, the HIPPARCOS catalogue is selected, and by extrapolating the data, explained in section 2.4, a star map with accurate information about any star is created. Data accuracy is then analyzed for the purpose of this work as reported in section 2.2.
- Subsequently, a camera model is proposed to create a subset of stars within a constrained observed scene. This point is needed to simulate the selected camera projection, capable of elaborating the conversion from 3D-world to the 2D-image. Another advantage is the capability to allow different characteristics for each observed scenario along all directions, as explained in chapter 4.
- Hence, the brightness of observed stars is computed and converted into image values, through the photo-electrons equation and camera system parameters. The final unit of measure will be chosen between these equivalent quantities: Analog to Digital Unit [ $ADU$ ], Digital Number [ $DN$ ], or also Gray Values in this case.
- Afterwards, the image values of the scene are revised to model the optical distortions and the focus capability of the cameras' optics. Again, a generic model of the camera Point Spread Function ( $PSF$ ) is used to model these effects. This model will be explained in section 4.2.1.
- Finally, are added the typical noises of the camera system (due to: sensor, optic, electronic) and the environmental noises of the background scene analyzed. These models will be explained in details in section 4.3.
- In the end, it is possible to simulate an image of the selected star field, with an accurate model of star brightness, camera model and model of noises.

It is worth underlining that the models used to simulate some behaviors, especially regarding camera projections and background noises, are knowingly selected generic in order not to limit the flexibility of the simulator and to set this work as a proper baseline for many applications. Indeed, for further optimization of specific features, these kinds of models will require elaboration. Otherwise, if the models' complexity is appropriate for the desired application of simulation, it is only necessary to retrieve the expected parameters and substitute them to the reference values used to simulate a typical space scenario. Note that all the parameters selected came from standard devices among the most used in the space sector, like those reported in these references [20, 37, 58, 62, 69].

### 3.1. Characteristics of AGS and DGS model

The most precise feature of this simulator is the model to compute the star brightness in the simulated image. This accurate computation is performed through the Discrete Grey Scale (*DGS*) model that allows to work with spectral properties of the simulator's parameters. This model is opposed to the most common one: the Average Grey Scale (*AGS*) model, used in many works like [53, 66, 79], which is less complex since it uses the average approximations of the parameters needed.

In particular, the *DGS* model is essential to perform an accurate simulation of the star brightness, taking into account the spectral behavior of observation devices and stars' flux density which can vary greatly depending on the desired scenario.

Then, in this work, the simulation through the *AGS* model is presented to give a comparison between the two models and to show the errors due to the approximations of *AGS*, shown in section 5.4. A similar comparison between models is performed in the scientific paper [33], which claims, through a night-sky ground test experiment, to decrease the error of star brightness simulation from 5% up to 15%, depending on the observed scenario. It is worth pointing out that both the models used for this work, *AGS* and *DGS*, are slightly different from the models used in the aforementioned paper since, in this work, the aim is to develop a more general star map simulator baseline capable of being used with different devices in many other scenarios. Specifically, the main distinction lies in how the zero reference point is determined in the *AGS* model, which will be explained in section 3.4.

Now are analyzed the main differences between the two models, *AGS* and *DGS*, considering: *assumptions* and *formulations*.



### Discrete Gray Scale (*DGS*)

In order to make the model computation feasible, some assumptions need to be taken into account. In particular, the procedures and the theoretical basis of this method are explained in detail in the following section, but the basic assumptions are reported here:

- Stellar spectra and their Effective surface temperatures are approximated using Blackbody models;
- Stars are considered point sources of light and are approximated as Lambertian sources;
- Solar system' celestial objects, like Sun, planets, moons, and asteroids are disregarded;
- Any dynamics of the observation device is disregarded;
- The Optical Aperture of the observation device is simulated with circular shaped.

Other more specific assumptions are directly expressed in the section were that concept is explained, for example as UBVR Johnson filters with the Bessel approximation in section 2.4.1.

The resulting formula, the photo-electrons equation, of this method to compute the camera's detected signal ( $G_{DGS}$ ) of a star is the equation 3.1. Where,  $D_{cam}$  is the Circular Aperture Diameter of the camera, evaluated in [ $m$ ];  $time$  is the Exposure Time by which the image is simulated, evaluated in [ $s$ ];  $Gain$  is the System Gain of the device, evaluated in [ $\frac{e^-}{ADU}$ ];  $QE(\lambda)$  is the Quantum Efficiency of the device per unit wavelength;  $\tau_{opt}(\lambda)$  is the Optical Transmissivity of the device per unit wavelength;  $F_m(\lambda)$  is the spectral Flux Density of the star, evaluated as [ $\frac{W}{m^2 \cdot m}$ ];  $hc/\lambda$  is the evaluation of the photon's energy at any wavelength, evaluated in [ $J$ ].

$$G_{DGS} = \frac{\pi}{4} \cdot D_{cam}^2 \cdot \frac{time}{Gain} \cdot \int_{\lambda_1}^{\lambda_2} \frac{F_m(\lambda)}{hc/\lambda} \cdot QE(\lambda) \cdot \tau_{opt}(\lambda) d\lambda ; \quad (3.1)$$

### Average Gray Scale (*AGS*)

The basic assumptions of this common model are used to simplify the computation, allowing a certain approximation on the final result. Again, the procedures and the theoretical basis of this method are explained in detail in the following section, but the basic assumptions are reported here:

- Stellar spectra and all spectral properties are considered flat, using an average value.

- Stars are considered point sources;
- Solar system' celestial objects, like Sun, planets, moons, and asteroids are disregarded;
- Any dynamics of the observation device is disregarded;
- the magnitude data, in Johnson V-band, are considered valid in the complete spectrum of each star, which is considered as Vega-type spectral class (A0);
- The reference zero-point considered follows a particular procedure developed through the DGS model and its assumptions;
- The Optical Aperture of the observation device is simulated with circular shaped.

Note that some assumptions are equivalent to the DGS model, since these are common in star map simulators and are approximation very near to the reality.

The resulting formula, the photo-electrons equation, of this method to compute the camera's detected signal ( $G_{AGS}$ ) of a star is the equation 3.2. Where, the parameters are the same of the *DGS* model, but every spectral property expressed per unit wavelength is now reported as a single average value, in particular:  $\lambda_{avg}$ ,  $QE_{avg}$ ,  $\tau_{opt,avg}$ .

$$G_{AGS} = \frac{\pi}{4} \cdot D_{cam}^2 \cdot \frac{time}{Gain} \cdot \frac{F_{m,AGS} \cdot \lambda_{avg}}{hc} \cdot QE_{avg} \cdot \tau_{opt,avg} ; \quad (3.2)$$

## 3.2. Black-body model of stars and Irradiance determination

The Black-Body model assumes that the body, which in this case are stars, absorbs all the incident radiation and emits thermal radiation as a function of its temperature, which distribution is continuous across all wavelengths. This radiation follows a specific spectral distribution known as Planck's law and allows to exploit the spectral properties of stars. It represents an ideal model that fits very close to reality, for most of the stars, although it does not consider the absorption lines of the spectrum corresponding to the elements on the stars' surface as shown in figure 3.1.

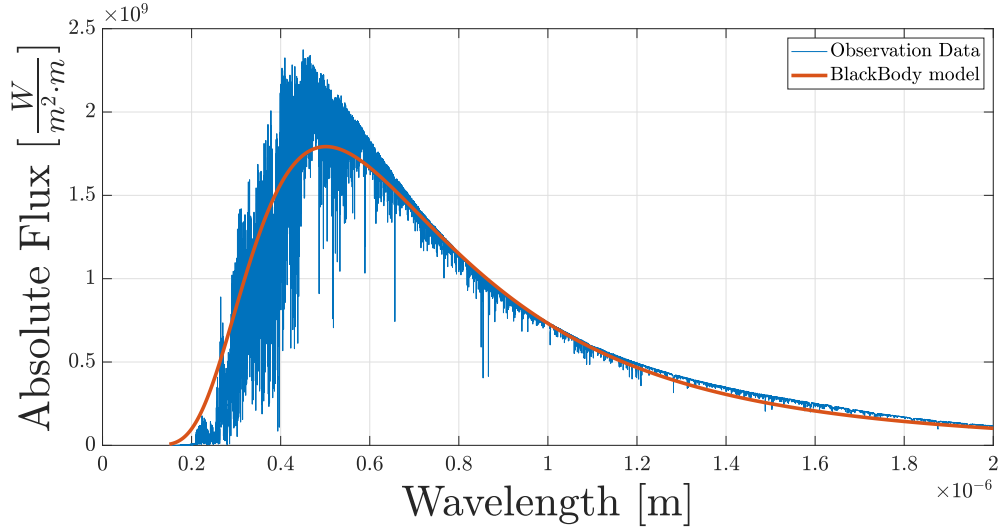


Figure 3.1: This figure shows the comparison between the observed Sun spectrum and its approximation through Black-Body approximation. Source: Observation Data retrieved by reference [67]

The Planck's Law is used to approximate the Spectral Radiance<sup>1</sup> of stars across wavelengths, which is computed using SI units of measure  $[\frac{W}{sr \cdot m^2 \cdot m}]$ , and it is reported in equation 3.3. Where  $K$  value is the Boltzmann constant measured in  $[\frac{J}{K}]$ ; the  $h$  value is the Planck constant measured in  $[J \cdot s]$ ;  $c$  value is the speed of light constant measure in  $[\frac{m}{s}]$ .

However, the assumption of Lambertian source allows us to define the Spectral Exitance of stars, measured as  $[\frac{W}{m^2 \cdot m}]$ , starting from the integration of Plank's law across the solid angle of stars' emission direction, as reported in equation 3.4. Where the value  $\pi$  is measured in  $[sr]$ .

The Lambertian approximation consists of sources which emitting radiation is directly proportional to the cosine emission law. The result of this approximation is that the emitting surface Radiance is completely independent from the viewing angle. Thanks to the black-body and point-source approximations, it is possible to simplify the solid angle parameter of observed stars. However, note that, for example, this is no longer valid in the case it is desired to add the simulation of galaxies or other diffuse celestial objects as an additional source of light.

$$f(\lambda, T) = \frac{2hc^2}{\lambda^5 (e^{hc/\lambda kT} - 1)} \quad (3.3)$$

<sup>1</sup>The following nomenclature is stated from SI radiometry units.

$$f_{rad}(\lambda, T) = \int_0^{2\pi} \int_0^{\frac{\pi}{2}} f(\lambda, T) \cdot \cos(\theta) \cdot \sin(\theta) d\theta d\phi = \pi \cdot f(\lambda, T) \quad (3.4)$$

Accordingly to these theoretical basis it is possible to link the Spectral Irradiance of stars, to the Planck's law following the procedure reported by equations: (3.5, 3.6, 3.7, 3.8, 3.9, 3.10).

In particular, the black-body model states that the luminosity ( $S$ ) of a star, measured in  $[W]$ , is computed by equation 3.5. Where  $\sigma$  is the Stefan-Boltzmann constant measured in  $[\frac{W}{m^2 \cdot K^4}]$ ;  $T$  is the effective temperature of the star, near to Surface Temperature, measured in  $[K]$ ;  $S$  is the radius of the spherical star measure in  $[m]$ . While, the Irradiance ( $I$ ) of a star is computed by equation 3.6 and is measured in  $[\frac{W}{m^2}]$ . Where  $d$  is the distance of the star from Earth<sup>2</sup> measured in  $[m]$ . Thus, thanks to Lambertian approximation it is possible to compute the total Radiant Exitance ( $R$ ) over all the wavelengths, measured in  $[\frac{W}{m^2}]$ , that is directly linked to the Luminosity ( $L$ ) of stars by equation 3.7. Where  $\lambda$  is the wavelength measured in  $[m]$ . Then, it is defined the Dilution Factor ( $P_x$ ) of stars' Irradiance, that is specific for each star and reported in equation 3.8, this parameter is dimensionless. In order to evaluate the Dilution Factor ( $P_x$ ) using only available star data, like total Irradiance ( $F_{bolo}$ ) from bolometric magnitudes or other spectral sources, the equation 3.9. Finally, the procedure is completed by equation 3.10 where is defined the Spectral Irradiance parameter<sup>3</sup> ( $I(\lambda)$ ), which is measured in  $[\frac{W}{m^2 \cdot m}]$ , through the use of Planck's law and Dilution Factor parameters.

$$L = 4\pi S^2 \cdot \sigma T^4 ; \quad (3.5)$$

$$I = \frac{L}{4\pi d^2} = \frac{4\pi S^2}{4\pi d^2} \cdot \sigma T^4 ; \quad (3.6)$$

$$R = \int_0^{\infty} f_{rad}(\lambda, T) d\lambda = \sigma T^4 ; \quad (3.7)$$

$$P_x = \frac{S_x^2}{d_x^2} = \frac{I}{\sigma T^4} ; \quad (3.8)$$

---

<sup>2</sup>This parameter can be computed from the Parallax data of the catalog, but this introduce a non-negligible source of error.

<sup>3</sup>Note, the Irradiance parameters reported in this work have a double nomenclature, in fact can be reported with the symbol ( $I$ ) or with the symbol ( $F$ ).

$$P_x = \frac{I}{\sigma T^4} = \frac{F_{bolo}}{\int_0^\infty f_{rad}(\lambda, T) d\lambda} ; \quad (3.9)$$

$$I(\lambda) = P_x \cdot f_{rad}(\lambda, T) ; \quad (3.10)$$

It is worth pointing out that this procedure allows to determine the Spectral Irradiance ( $F(\lambda)$ ) of stars, starting from the parameters: Effective Surface Temperature ( $T_{star}$ ) and Bolometric Irradiance ( $F_{bolo}$ ). However, linking these parameters to the catalogue's visual magnitude data ( $m_v$ ) is fundamental. This operation comes from the substitution of equation 3.10 into equation 2.7 of filtered magnitude developed for Johnson V-band.

Thus, the general Spectral Irradiance of a star is computed through the equations 3.11, 3.12. Where  $P_m$  value is the Dilution Factor for a general "m" star;  $T_m$  value is the Effective Temperature of a general star;  $m_V$  is the visual magnitude of a general star;  $F_{ref}(\lambda)$  parameter is the Reference Spectral Irradiance and  $m_{V,ref}$  value is the corresponding visual magnitude of the reference parameter, those are defined in section 3.4;  $R_V(\lambda)$  parameter is the Johnson V-band filter defined in section 2.4.1 and shown in figure 3.2. Finally, this procedure allows to retrieve the Spectral Irradiance ( $F_m(\lambda)$ ) of any star using only the data contained in the catalog.

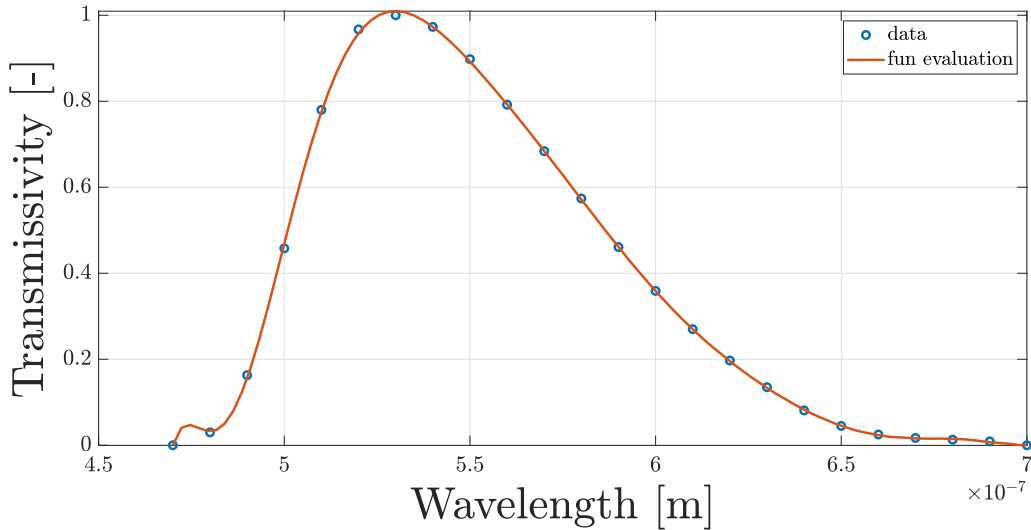


Figure 3.2: This figure represent the Bessel approximation of the Johnson V photometric filter. Source: function evaluation of data retrieved from reference [7].

Note that the origin of the additional  $\lambda$  parameters in the equation 3.11 comes from the assumption that all the visual magnitude included in the HIPPARCOS catalog are measured with a photon-counting detector, so the main instrument of Hipparcos Mission, as reported in [15] , or are converted into it. Accordingly, these instruments evaluate the photon rate of the sources, and then the expression of photon rate is:  $F_m(\lambda) \cdot \lambda/hc$ .

$$P_m = 2.512^{-(m_V - m_{V,ref})} \cdot \frac{\int_0^\infty F_{ref}(\lambda) \cdot R_V(\lambda) \cdot \lambda d\lambda}{\int_0^\infty f_{rad}(\lambda, T_m) \cdot R_V(\lambda) \cdot \lambda d\lambda} ; \quad (3.11)$$

$$F_m(\lambda) = P_m \cdot f_{rad}(\lambda, T_m) ; \quad (3.12)$$

### 3.3. Black-body Temperature from B-V index color

In astronomy, there is a classification of stars based on their spectral characteristics, from luminosity to spectral lines that indicate chemical composition of stars' photosphere.

The Morgan–Keenan (MK) system is currently the primary classification system for most stars. It utilizes the letters O, B, A, F, G, K, and M, representing a sequence from the hottest (O type) to the coolest (M type). Within each letter class, further subdivision occurs through a numeric digit, with 0 denoting the hottest and 9 the coolest (e.g., A8, A9, F0, and F1 form a sequence from hottest to coolest). Then, a luminosity class is added to the spectral class using Roman numerals. This classification is based on the width of specific absorption lines in the star's spectrum, which varies according to the density of the atmosphere and thus differentiates giant stars from dwarfs. Luminosity class 0 or Ia+ is assigned to hypergiants, class I to supergiants, class II to bright giants, class III to regular giants, class IV to subgiants, class V to main-sequence stars, class sd (or VI) to subdwarfs, and class D (or VII) to white dwarfs. For example, the complete spectral class for the Sun is designated as G2V, denoting a main-sequence star with a surface temperature of approximately 5,800 K.

Whereas that in the presented model of simulator the spectral lines of stars' chemical composition is not considered and the main characteristic of spectral proprieties of stars is provide by the Effective Temperature of the surface with the Black-body model. An example of different Spectral Radiance of stars is then shown in figure 3.3.

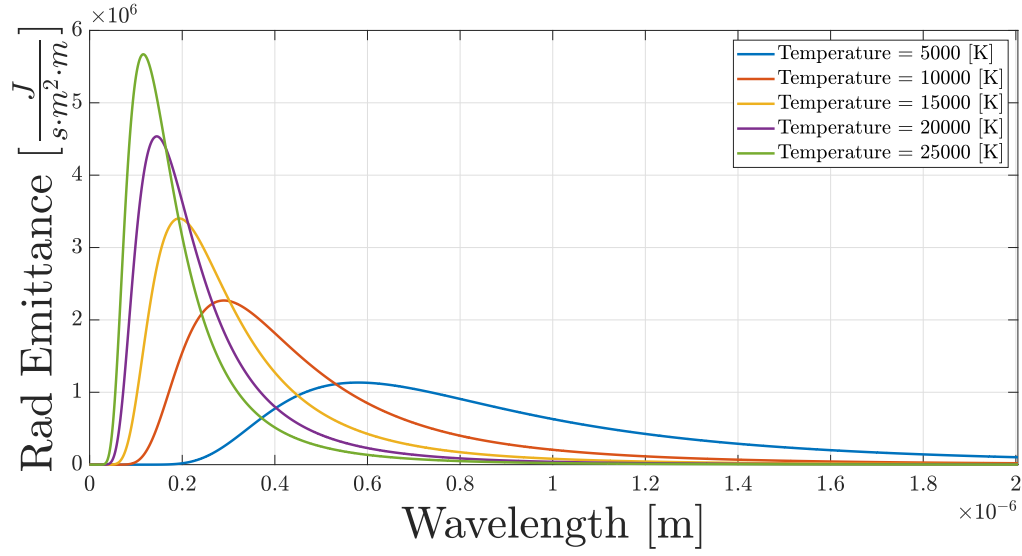


Figure 3.3: This figure shows the various spectral Emittance of stars for different Effective Surface Temperatures. Note that these results represent the Black-Body model approximation.

Considering that the stars' temperature is not a catalog parameter, it needs to be retrieved thanks to the Black-body model. In fact, from figure 3.4 is shown that every star, thanks to its unique spectral emission, has the possibility to retrieve the information about the effective temperature of the curve using two measurements of the spectrum in different bands. In particular, the brightness measurements of stars across two different Johnson's Filters, the U-band (reported in black) and V-band (reported in blue), enable the possibility to define the temperature information of the emission spectrum, dismissing any influence of magnitude values of equivalent stars. This operation is known as Color-Temperature Correlation, where as Color is considered the subtraction of brightness measurements with two different filters, in this case is considered the catalog parameter BV index color, reported in equation 2.8.

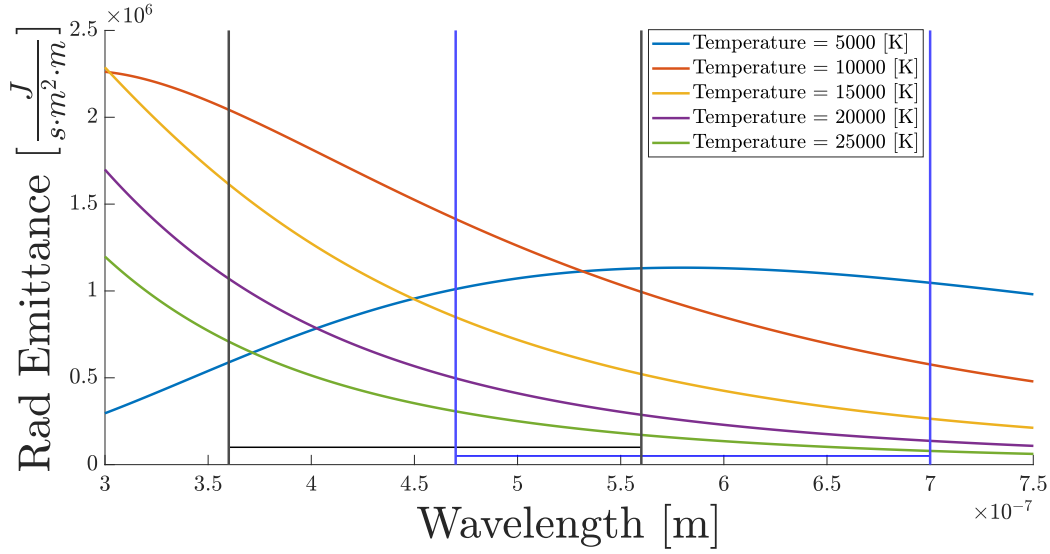


Figure 3.4: This figure shows the behaviour of star spectral Emittance in the ranges of two typical filters, the Johnson-B (in black) and the Johnson-V (in blue).

The exact procedure for the color-temperature correlation is reported in equation 3.13, and this model is retrieved from [33]. Note that this procedure still implies an approximation, since it does not distinguish between the spectral classification of stars given by their size. In fact, as shown in figure 3.5, different class of stars can have different temperature with the same  $BV$  value. Accordingly, there are many other possible correlations to retrieve this parameter, even considering stars' spectral classes, like the one present in the work by Flower [24].

$$T_m = \begin{cases} 1079.20644e^{-BV/0.09824} + 8180.59419 & BV < 0 \\ 8906.09411e^{-BV/1.59761} + 3.633 & BV \geq 0 \end{cases} \quad (3.13)$$

This model has been chosen because it generally fits well for any spectral class under consideration, with the exception of dwarf stars, which are not accounted for even in the model by Flower. It is reported through the figures 3.6 a comparison analysis between the two Color-Temperature Correlation. Where, with the index (3) is mentioned the model by Flower, computed for two categories respectively Supergiants stars, and Others that comprises Main-Sequence, Subgiants, and Giants stars. Instead, with the index (1) is mentioned the model used in this work.



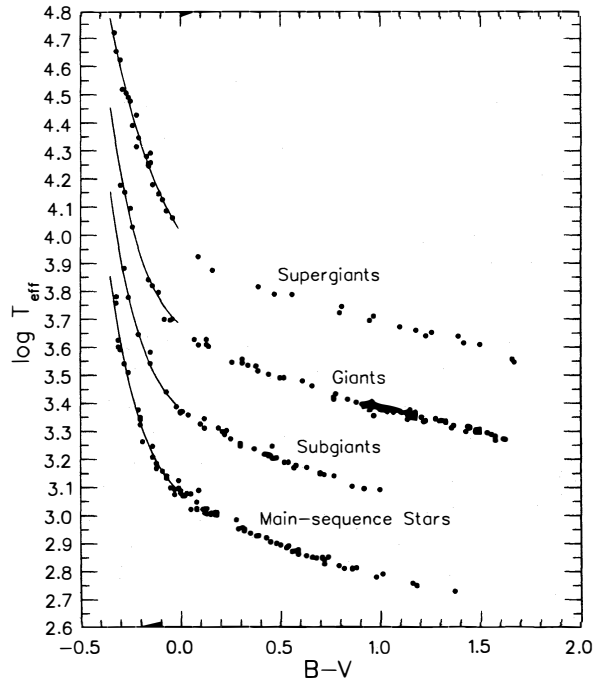


Figure 3.5: This figure shows the relation between  $BV$  index color and Effective Surface Temperature for different classes of stars. Source: figure acquired from reference [24]

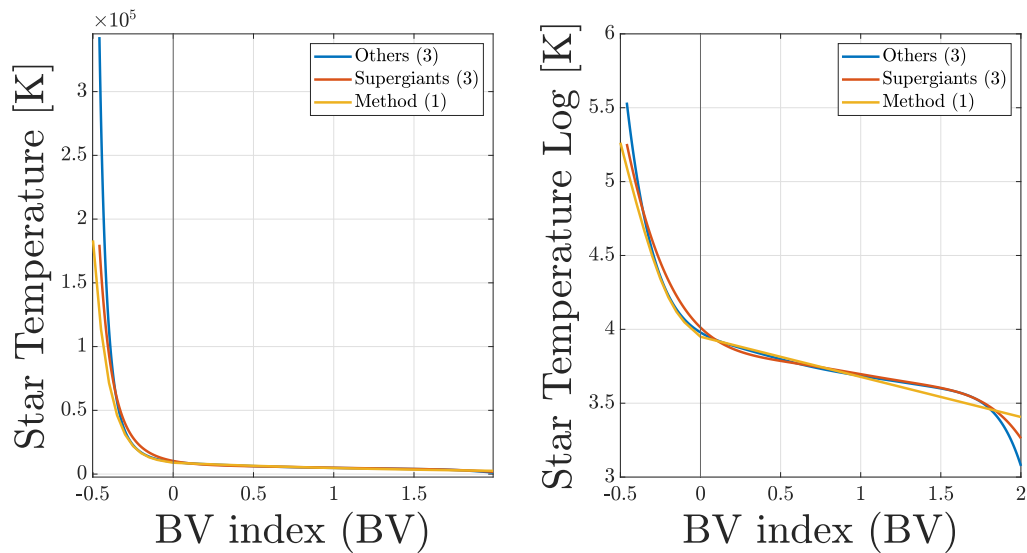


Figure 3.6: This figure shows the comparison between the model of Flower [24] and the model selected for this work. In the left figure is present the linear temperature output, instead in the right figure is present the logarithmic temperature output. Note that the Method (1) is the model reported in 3.13, the Supergiant (3) and Other (3) is the Flower model, respectively for Supergiants star and for all the other classes of stars.

It is worth pointing out that the large differences between models for negative values of  $BV$  parameter is less significant for the HIPPARCOS catalog data, since there are only 13 stars with  $BV < -0.3$ . In general, the range of greatest interest for the catalog is between:  $BV = [0; 2]$ , where are included 99.1% of the stars.

### 3.4. Determination of Zero-Point Reference

One of the most important steps of the magnitude scale measurement is defining the zero-point reference from which the magnitude must be computed. Historically, the reference point selected was the Vega star spectrum, applied for visual apparent magnitude and then for Johnson's UBV filters, for the reasons mentioned in 2.4.3. However, for the *DGS* model, it is selected to use the reference value of bolometric flux density for 0 magnitudes ( $F_{0,bolo}$ ), defined in [56], applied on the black-body model of a Vega-like star, so with the same Effective Surface Temperature:  $T_0 = 9602 [K]$ . Thus, this computation is implemented by equations 3.14, 3.15.

This choice has been made because of the black-body model's bad approximation of the Vega spectrum due to its intrinsic characteristics, as shown in 3.7. In addition, the uncertainties about information on the Vega Bolometric Flux Density forces us to use approximations like the Bolometric Correction reported in [24]. Consider that, obviously, it is not feasible to measure the spectrum of a star along all the wavelengths up to infinity; it is only possible to measure up to significant spectrum values if the sensor detection allows that.

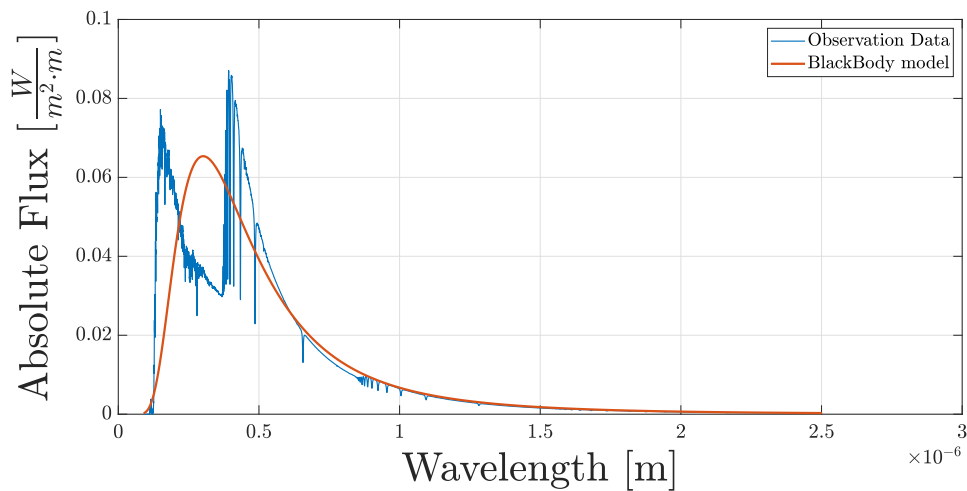


Figure 3.7: This figure shows the comparison between the observed Vega spectrum and its approximation through Black-Body approximation. Source: Observation Data retrieved by reference [68].

$$P_0 = \frac{F_{0,bolo}}{\int_0^\infty f_{rad}(\lambda, T_0) d\lambda} ; \quad (3.14)$$

$$F_{ref}(\lambda) = P_0 \cdot f_{rad}(\lambda, T_0) ; \quad (3.15)$$

Considering the *AGS* model used in this work, a particular zero-point reference is selected, since this model is needed for comparison with the *DGS* one. Commonly, the selection of the zero-point reference of *AGS* model is selected equals to the value of Bolometric Flux Density for 0 magnitude ( $F_{0,ref}$ ). However, in this case results a wrong selection because in that case the computation of star irradiance ( $F_{m,AGS}$ ), reported in equation 3.16, is calculated over the bolometric wavelength and not over the relevant bandwidth of the simulation. In fact, this simulator is able to calculate the brightness of stars as if they were observed by a specific camera device, which therefore has a limited detection wavelength range.

Thus, a particular procedure has been created to calculate the exact zero-point reference for any selected observation device, depending on its detection wavelength range and using the *DGS* model. This procedure is reported in equation 3.17. Where,  $P_0$  and  $T_0$  values are the same selected for *DGS* model, and the values  $\lambda_{C,1}$ ,  $\lambda_{C,2}$  identify the boundary of the device's detectable wavelength range. Finally, through the reported procedure it is possible to compare the two models in order to understand the differences.

$$F_{m,AGS} = 2.512^{-(m-m_0)} \cdot F_{0,ref} ; \quad (3.16)$$

$$F_{0,ref} = P_0 \cdot \int_{\lambda_{C,1}}^{\lambda_{C,2}} f_{rad}(\lambda, T_0) d\lambda ; \quad (3.17)$$

### 3.5. Models Procedure

This chapter resumes the complete procedures to develop both simulated models, *DGS* and *AGS*, and it is useful to reproduce the correct workflow followed for this simulator. It is worth underling that the procedures already described report only the first half of the simulator, since the models used to reproduce the camera behaviors are described in the next chapter.

Starting from the most important model, for this work, the *DGS* procedure followed is:

- Identification of a subset of observed stars, from catalog, to be simulated with their photometric and astrometric properties.
- Definition of Zero-Point Reference ( $F_{ref}(\lambda)$ ), through the procedure reported in 3.4.
- Definition of Johnson V-band Filter function ( $R_V(\lambda)$ ) to compute the values of  $P_m$ , reported in equation 3.11, for the entire subset of simulated stars. Thus, determine the Spectral Flux Density values ( $F_m(\lambda)$ ), equation 3.12.
- Identify a camera device to simulate and define its parameters:  $D_{cam}$ ,  $time$ ,  $Gain$ ,  $QE(\lambda)$ ,  $\tau_{opt}(\lambda)$ . Thus, compute the electrons detected by the sensor for any simulated star through the photo-electrons equation 3.1.
- Compute Optical Point Spread Function ( $PSF$ ) and Camera Noises of the simulated scenario.
- In conclusion, assemble values from the various sources: stars, background, noises, and produce the simulated image.

Instead, regarding the *AGS* model the procedure followed is similar to the previous one, but with further simplifications given by the model definition :

- Identification from catalog of a subset of observed stars to be simulated with their photometric and astrometric properties.
- Definition of Zero-Point Reference ( $F_{ref}(\lambda)$ ), through the particular procedure reported in 3.4 and described in equation 3.17. Thus, compute the Flux Density values ( $F_{m,AGS}$ ), equation 3.16.
- Identify a camera device to simulate and define its average parameters:  $D_{cam}$ ,  $time$ ,  $Gain$ ,  $QE_{avg}$ ,  $\tau_{opt,avg}$ . Thus, compute the electrons detected by the sensor for any simulated star through the photo-electrons equation 3.2.
- Compute Optical Point Spread Function ( $PSF$ ) and Camera Noises of the simulated scenario.
- In conclusion, assemble values from the various sources: stars, background, noises, and produce the simulated image.

Note that for both the reported procedures the last two steps are just stated and will be explained in the next chapter.



# 4 | Camera Model

This chapter will describe all the models used to simulate the camera behavior, relating to its projections, distortions and noise sources. In particular, the projection matrix by which the camera sees the 3D real world will be analyzed, along with the projections used in this work and their properties. Then, the contribution of the Point Spread Function (*PSF*), used to simulate the optical spreading of the point source and the focus capability of the simulated device, will be explained. Finally, the primary noise sources of a camera device will be examined and how they can be modelled.

## 4.1. Pixel Coordinate Projection

The projection of a camera device requires the optical and sensor parameters to create the Camera Matrix Model. This matrix is usually obtained by experimental calibration of the device or using simulation software like ZEMAX or CODEV, where it is possible to design an optical system. The peculiarity of a complete Camera Matrix Model is the capability to retrieve and then simulate any distortions and aberrations created by the camera and its optical system. In this work, a simplified projection model is used since the exact Camera Matrix can be obtained only through the calibration of a specific device, but the aim of this work is to create a baseline by which it is possible to simulate a wide range of scenarios and devices.

This section is composed of an introduction of the Camera Models used in this work, namely the Perspective and the Weak-Perspective projection, which differ from the typical use simulation; then it is reported the procedure developed to retrieve only the stars present in the Field of View, thus creating the subset of stars from the catalog.

### 4.1.1. Perspective Projection

The Perspective projection represent the projection of the simplest camera model, known as Pinhole Camera. This projection consider a camera without any lens, with the light that is projected into the image plane passing entirely through a single point, called center of projection, as shown in figures 4.1.

This model can be described using a  $[3 \times 3]$  matrix, called Calibration Matrix ( $\mathbf{M}_{\mathbf{P}}$ ), that is reported in equation 4.1. Where,  $\alpha$  and  $\beta$  are conversion parameters from the Camera Body Frame to the Pixel Coordinate Frame, evaluated in  $[\frac{pixel}{mm}]$ ;  $f$  is the focal length of the device, evaluated in  $[mm]$ ;  $n_{pix,H}$  and  $n_{pix,V}$  are the number of pixel in the sensor, respectively aligned with horizontal and vertical direction;  $size_{sens,H}$  and  $size_{sens,V}$  are the size of the sensor in horizontal and vertical directions, evaluated in  $[mm]$ ;  $c_x$  and  $c_y$  are the optical center offset of the image, evaluated in  $[pixels]$ , usually images start with the coordinates  $[0, 0]$  in the upper-left corner.

This matrix needs to be multiplied by the Cartesian vector ( $\mathbf{s}_{star}$ ) that expresses the stars position in the Camera Body Frame, already described in section 2.3.2. Then, using the homogeneous coordinates system to maintain the linearity of the problem, it is possible to determine the pixel coordinates in the simulated image for each star, through the procedure in equation 4.2, as reported in [31]. Where,  $\mathbf{u}_{\mathbf{c}}$  is the vector in pixel coordinates of the star position;  $\mathbf{M}_{\mathbf{P1,h}}$  and  $\mathbf{s}_{star,h}$  are respectively the Perspective Camera Model and the Star Vector Position with the Homogeneous Coordinate system.

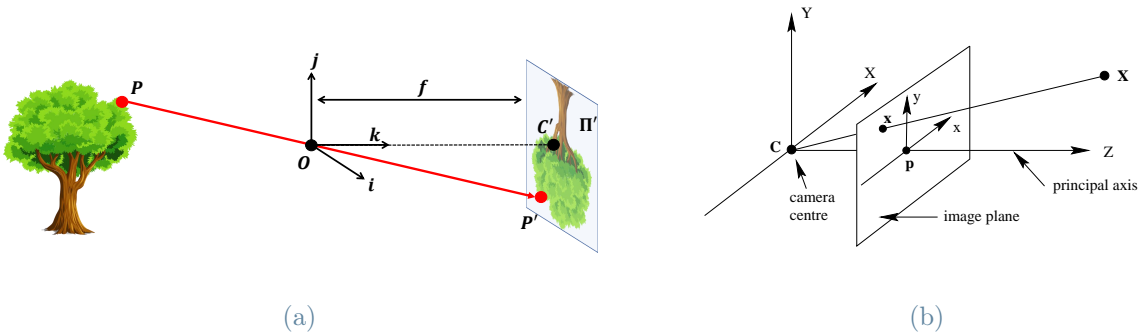


Figure 4.1: These figures show the Pinhole Camera Model. Figure 4.1a represent the basic working principle of the pinhole model, instead Figure 4.1b represent the mathematical description in the pinhole model. Sources: 4.1a reference [31]; 4.1b reference [30].

$$\mathbf{M}_{\mathbf{P}} = \begin{bmatrix} \alpha & 0 & c_x \\ 0 & \beta & -c_y \\ 0 & 0 & 1 \end{bmatrix}; \quad \text{Where : } \alpha = \frac{f \cdot n_{pix,H}}{size_{sens,H}}; \quad \beta = \frac{f \cdot n_{pix,V}}{size_{sens,V}}; \quad (4.1)$$

$$\mathbf{u}_{c1} = \begin{bmatrix} u_x \\ u_y \\ 1 \end{bmatrix} = \begin{bmatrix} \alpha \cdot s_1/s_3 + c_x \\ \beta \cdot s_2/s_3 - c_y \\ s_3/s_3 \end{bmatrix} = \frac{1}{s_3} \cdot \begin{bmatrix} \alpha & 0 & c_x & 0 \\ 0 & \beta & -c_y & 0 \\ 0 & 0 & 1 & 0 \end{bmatrix} \begin{bmatrix} s_1 \\ s_2 \\ s_3 \\ 1 \end{bmatrix} = \mathbf{M}_{P,h} \cdot \mathbf{s}_{star,h} \quad (4.2)$$

The main feature of this projection is the capability to represent the scaling and the foreshortening properties in the projected image plane. This model fits particularly well when the simulated scenario presents celestial objects at different distances and with relatively large sizes, like, for example, planets, moons and galaxies. A more accurate consideration for this camera model, as compared to the subsequent one to be discussed (the Weak-Perspective model), is to employ it in simulations involving a large Field of View or a small Focal length. Notably, a distinctive feature of this model, illustrated in image 4.2, is the vertical tilting of the simulated image concerning the real world.

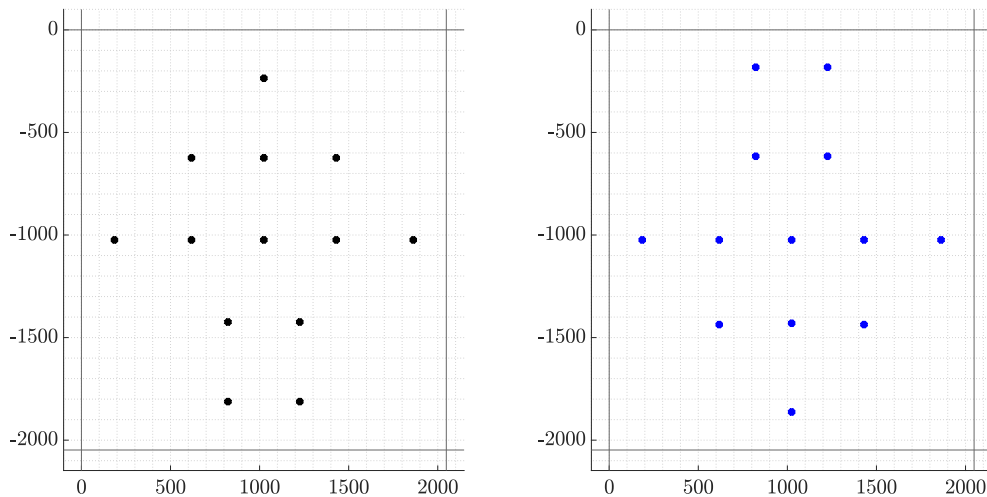


Figure 4.2: This figure shows the Perspective projection of the camera. Note that the figure on the left represent the real world, instead the figure on the right represent the camera projection.



### 4.1.2. Weak-Perspective Projection

The Weak-Perspective projection represents an approximation of the Affine Camera model, that is a model in which points are placed to a plane at infinity. In details, the Weak-Perspective projection considers all the points into the same plane which is arbitrarily scaled from infinity. Also in this case the projection is considered without any lens and the light will converge to a point, called center of projection.

This model can be described using a  $[3 \times 3]$  matrix, called Calibration Matrix ( $\mathbf{M}_{\mathbf{WP}}$ ), that is reported in equation 4.3. This matrix needs to be multiplied by the Cartesian vector ( $\mathbf{s}_{\text{star}}$ ) that expresses the stars position in the Camera Body Frame, already described in section 2.3.2. However, in this model the dependency on the Z direction drops, since the points are all considered on the same plane. Then a preliminary operation on the star vector is required, it is also reported in equation 4.3. Where, the parameters are the same of the previous section 4.1.1. Then, using the homogeneous coordinates system to maintain the linearity of the problem, it is possible to determine the pixel coordinates in the simulated image for each star, through the procedure in equation 4.4, as reported in [30]. Where, again, the parameters are the same of the previous section 4.1.1. Note that in this case the homogeneous coordinates is a  $[3 \times 1]$  vector, since the Z axis is dropped and can be neglected by the position vector. Furthermore, even if the points at infinity need to have the homogeneous coordinate equal to 0, in this case is considered a scaled plane with the same property of the infinity plane, but scaled to allow the matrices operations with the optical center offset parameters.

$$\mathbf{M}_{\mathbf{WP}} = \begin{bmatrix} \alpha & 0 & c_x \\ 0 & \beta & -c_y \\ 0 & 0 & 1 \end{bmatrix}; \quad \text{Whit} : \mathbf{s}_{\text{star}}^* = \frac{\mathbf{s}_{\text{star}}}{\mathbf{k} \cdot \mathbf{s}_{\text{star}}}; \quad \mathbf{k} = [0, 0, 1]; \quad (4.3)$$

$$\mathbf{u}_{\mathbf{c2}} = \begin{bmatrix} u_x \\ u_y \\ 1 \end{bmatrix} = \begin{bmatrix} \alpha \cdot s_1 + c_x \\ \beta \cdot s_2 - c_y \\ 1 \end{bmatrix} = \begin{bmatrix} \alpha & 0 & c_x \\ 0 & \beta & -c_y \\ 0 & 0 & 1 \end{bmatrix} \begin{bmatrix} s_1 \\ s_2 \\ 1 \end{bmatrix} = \mathbf{M}_{\mathbf{WP}} \cdot \mathbf{s}_{\text{star,h}}^* \quad (4.4)$$

The main feature of this projection is that all the points are placed into the same plane, consequently they are all considered at the same distance from the image plane. Thus, the direction of the stars projection is approximately orthogonal to the image plane and they are parallel between each other. This model fits particularly well when the simulated

scenario presents only distant celestial objects, like stars. Consequently, it should be preferred for simulations of devices with small Field of View and large focal length. Notably, a distinctive feature of this model, illustrated in image 4.3, is the horizontal tilting of the simulated image concerning the real world.

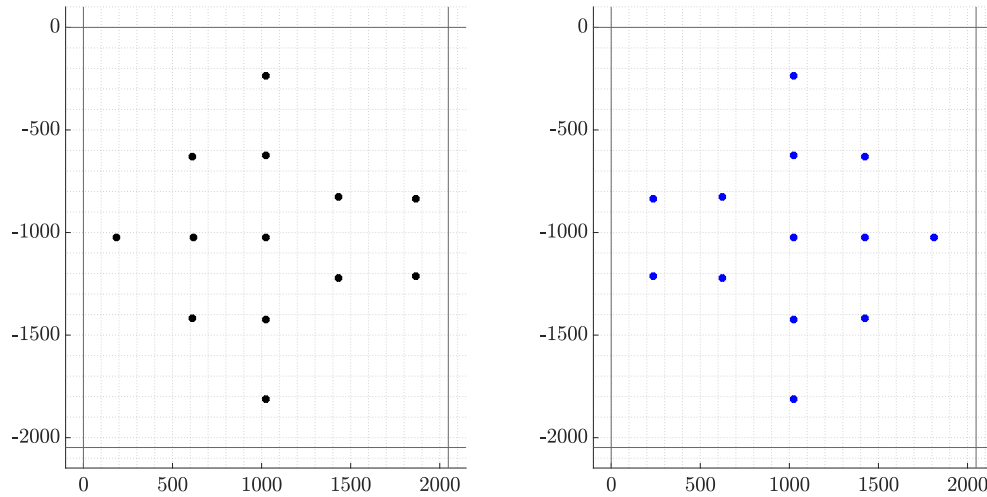


**Figure 4.3:** This figure shows the Weak-Perspective projection of the camera. Note that the figure on the left represent the real world, instead the figure on the right represent the camera projection.

### 4.1.3. Star selection in the Field of View

The creation of a subset of stars is fundamental in order to simulate only the observed stars in the image, without considering the complete catalog. This speed up the computational time of the simulation, allowing to produce multiple differentiated images. In particular, the subset creation procedure starts with a first definition of the approximative Field of View of the observation. In this work, it is considered that an optical device is used to perform the observation, then some parameters are necessary for the camera to produce the information needed on the Field of View. The procedure used comes from the rectilinear lens model and is reported in equation 4.5. Where the parameters used are:  $dim_X$  and  $f$ , respectively, the dimension of the sensor along the direction ( $X$ ), horizontal and vertical, and the focal length of the camera simulated.

Finally the approximative Circular Field of View radius ( $R$ ) is defined as in equation 4.6.

$$FOV_X = 2 \cdot \text{atan} \left( \frac{\text{dim}_x/2}{f} \right) ; \quad (4.5)$$

$$R = \frac{1}{2} \cdot \sqrt{FOV_H^2 + FOV_V^2} ; \quad (4.6)$$

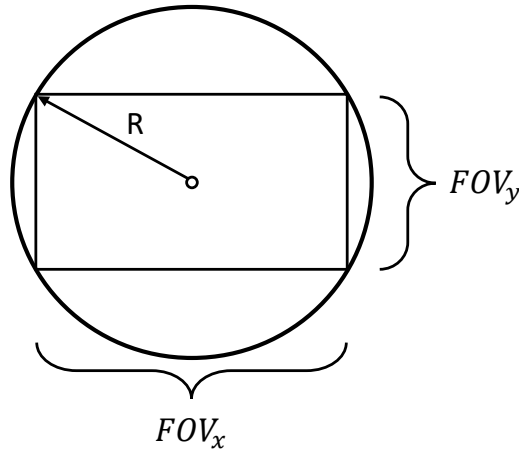


Figure 4.4: Camera Field of Views computations.

Thus, once the first subset of stars has been defined, it needs to be refined, since the real Field of View of cameras is commonly rectangular or squared as the shape of sensors. An example of this peculiarity is shown in image 4.4. Note that not the entire area of the Circular Field of View is covered by the real Rectangular Field of View, for this reason, a selection of stars from the subset is performed, considering only the ones that can be truly observed. The output of this procedure is shown in figure 4.5, and consists in the selection of stars comprised in the rectangular simulated image.

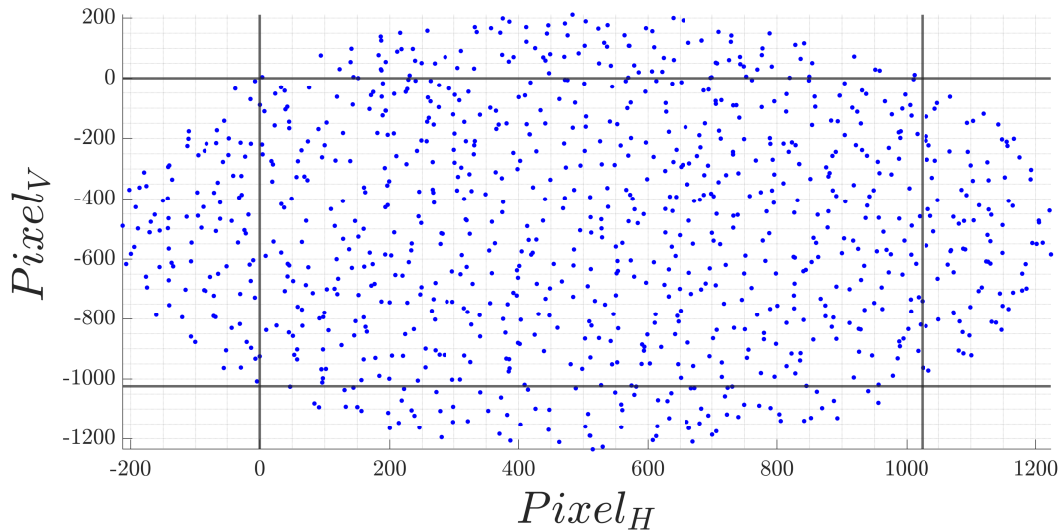


Figure 4.5: Stars Field of View detection procedure.

## 4.2. Point Spread Function

The Point Spread Function ( $PSF$ ) is a mathematical representation of how a point source of light, such as a star, distributes its light in the image plane of an observation device. In particular, it models some inherent aberrations of optical systems and the focusing capability of the device.

It is worth pointing out that the inherent aberrations considered are summarized with a general model of  $PSF$  that approximates the typical behaviour of these aberrations. For example, the model of  $PSF$  developed in this work tries to combine the approximated effects of: Optical Field Curvature, Spherical Aberration, Light Diffraction, Light Distortion, and Defocus Aberration. However, it is worth highlighting that this model is specifically tailored to address the Defocus Aberration. The emphasis on Defocus Aberration is significant in the context of simulations related to Star Tracker experimentation. In fact, achieving the required positioning accuracy for star locations necessitates sub-pixel precision, which is typically facilitated through intentional defocusing of the image, spreading the point source across multiple pixels.

The following sections describes the  $PSF$  model used in this work, explaining its rationale, working principles, computations, and the criterion for selecting its parameters.

### 4.2.1. PSF Model

A point source, such as stars, observed through a camera device generally covers a certain pixel region, forming a circular area influenced by a combination of optical aberrations and defocusing measures. This distribution model is referred to as the Point Spread Function (*PSF*). In many instances, the energy distribution of the imaging spot closely aligns with a two-dimensional Gaussian distribution, as depicted in Figure 4.6. In reality, the optical head of observation devices strictly determines the PSF and any device needs to be simulated with its proper Spread Function. In other cases, it is possible to retrieve the proper PSF of a device through the design of the optical part, using simulator software like ZEMAX or CODEV.

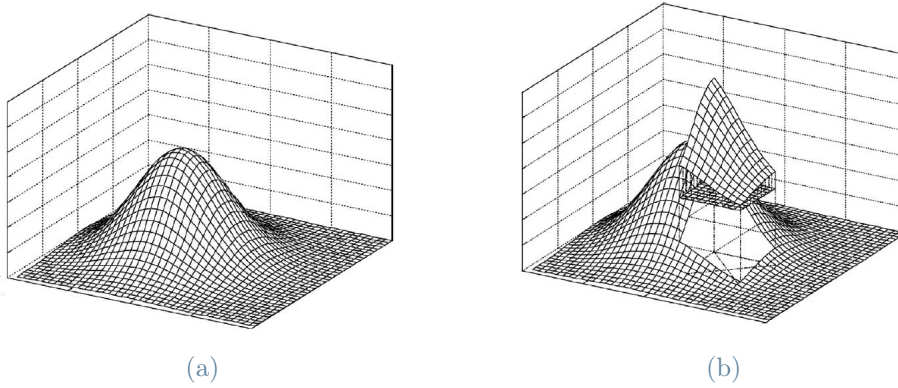


Figure 4.6: These figure represent the Gaussian PSF model for point source. Source : reference [74].

In specific terms, the employed PSF model in this study disperses the energy of a point source through a 2D Gaussian Distribution, delineated by the procedure in equations 4.7. Thus, the energy contribution for each pixel is determined by integrating the Gaussian distribution within the confines of the pixel. Where, the coordinates of the peak energy point in the distribution correspond to each simulated star's position in the image, which are derived from the catalog through the procedure outlined in Section 4.1. In particular, in equation 4.7, the used parameters are:  $\sigma_x$  and  $\sigma_y$  are respectively the Gaussian Radius of the horizontal direction ( $x$ ) and vertical direction ( $y$ );  $[x_c; y_c]$  are the pixel coordinates of the star centre position;  $[x_i; y_i]$  are the pixel coordinates around the star location, that can vary with the terms  $i$  and  $j$  to describe the pixel region ( $D$ ) in which the point source is spread;  $h(i, j)$  are the parameters of energy distribution in the pixels region;  $A$  is the energy value of the point source;  $g(i, j)$  is the energy distribution in the pixels region.

$$h(i, j) = \begin{cases} \frac{1}{2\pi\sigma_x\sigma_y} \cdot \int_{i-0.5}^{i+0.5} \int_{j-0.5}^{j+0.5} e^{-\left(\frac{(x_i-x_c)^2}{2\sigma_x^2} + \frac{(y_j-y_c)^2}{2\sigma_y^2}\right)} dx dy & (x, y) \in D \\ 0 & \text{Else} \end{cases} \quad (4.7)$$

$$g(i, j) = A \cdot h(i, j)$$

The procedure of this model requires the definition of the two Gaussian Radius ( $\sigma_x, \sigma_y$ ) and the definition of an acceptable region ( $D$ ) in which the point sources need to be spread. The calibration of these parameters is defined in the next section. Once these are defined, it is necessary to apply this procedure for any star, or celestial object, present in the simulated image, taking care to consider overlapping regions between nearby point sources.

#### 4.2.2. Calibration of PSF parameters

The calibration of the two parameters needed for the selected PSF model strictly depends on the scenario that is intended to be simulated. To comprehend their calibration for a specific application, a detailed explanation of their meaning follows.

The Gaussian Radius ( $\sigma$ ) represent the Standard Deviation of the Gaussian distribution, and it is used to simulate the defocusing level of the image. In particular, it is possible to differentiate this value for the  $x$  and  $y$  direction of the images. This could be necessary to simulate particular sensors or optics that do not have symmetrical behaviour between the two directions, which results into an ellipsoidal spreading of the point sources. Thus, the variation of the  $\sigma$  parameters will concentrate the point source spreading as the value of this parameter decreases. Some examples are reported in figures 4.7 4.8. Where are represented two distributions with Gaussian radius, respectively  $\sigma = 0.55$  and  $\sigma = 1.0$ , with symmetrical behaviours. After that, for completeness, an image showing the behaviour described by two different sigmas, in  $x$  and  $y$ , for this model is also shown in figure 4.9. From these observations, it is possible to select an appropriate value for the  $\sigma$  parameter. Specifically, in this work it is selected a  $\sigma$  value equal to 0.55 has typical value for multipurpose cameras of satellites, as stated in the manual papers of Rosetta Mission for its NAVCAM, in reference [26].

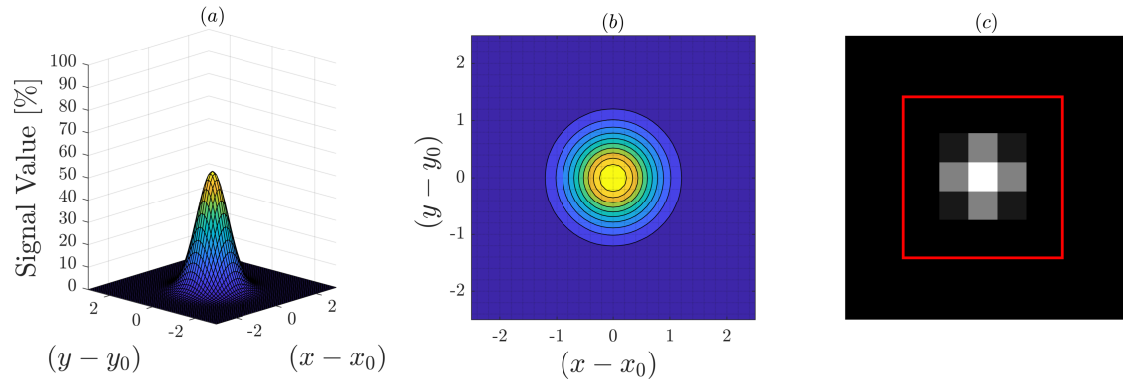


Figure 4.7: These figures show the signal behaviour under the Gaussian PSF model for a value of  $\sigma = 0.55$ . The figure (a) show the 3D distribution of the signal; the figure (b) shows the contour of the spatial distribution of the signal; the figure (c) shows the simulation of a point source in a synthetic image.

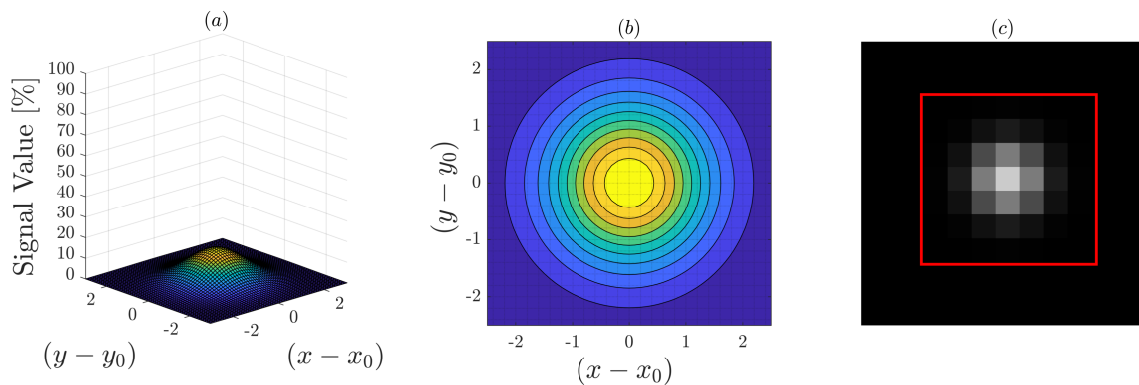
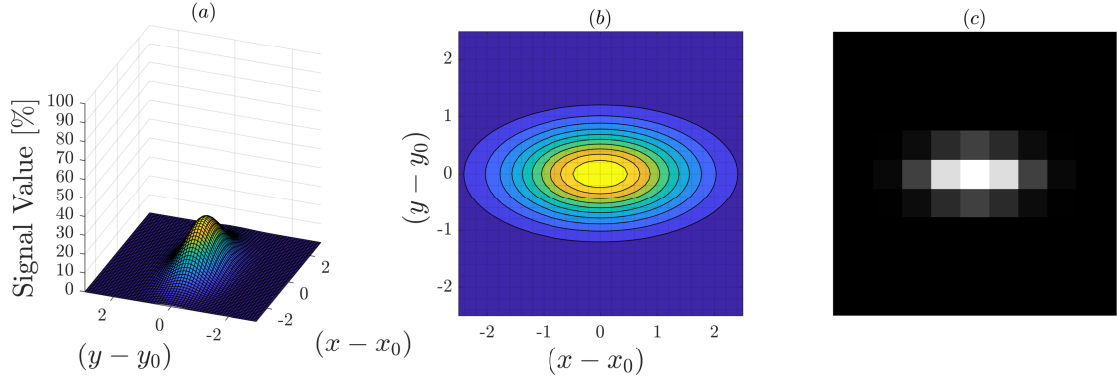


Figure 4.8: These figures show the signal behaviour under the Gaussian PSF model for a value of  $\sigma = 1.00$ . The figure (a) show the 3D distribution of the signal; the figure (b) shows the contour of the spatial distribution of the signal; the figure (c) shows the simulation of a point source in a synthetic image.



**Figure 4.9:** These figures show the signal behaviour under an asymmetrical Gaussian PSF model with different values of  $\sigma$  for horizontal and vertical directions. The figure (a) show the 3D distribution of the signal; the figure (b) shows the contour of the spatial distribution of the signal; the figure (c) shows the simulation of a point source in a synthetic image.

The region ( $D$ ) is the other parameter of this model that needs to be calibrated based on the desired simulation. Regarding the stars point sources, with symmetrical spreading behaviour, it is commonly selected a square of  $[n \times n]$  pixels that must contain all the energy information of the source, as it is shown in figures 4.7 , 4.8. The calibration of this parameter is developed starting from the procedure explained in the reference [66] , where is defined a procedure to state the energy concentration in a squared region of a star point source what respect to the total one. In particular, it is stated that for the star tracker simulation applications, the 95% of the energy is contained within a square of  $n$  pixel, in which the value of  $n$  is computed with this simple formula:  $n \geq \sigma \cdot 4.48$  . From these considerations, it is selected a parameter  $n$  equal to 12 pixels capable of satisfying a variety of simulation conditions.

### 4.3. Camera Noises

One of the important features of this simulator is the modelling of the camera noises. A camera device is typically composed by an optical head that deviates the light in a specific way, a sensor to detect and convert the light into electrons, and an electronic



part to convert and elaborate the sensor signal into an image. All these components own noise sources and introduce errors in the final image, as previously seen for the optical part with the aberrations. Regarding the sensor and electronic parts of a camera, they introduce several sources of noise that are analyzed in this section and modelled in the simulator to increase the fidelity of the simulated images.

The typical noises introduced by these last components can be categorized into three main groups:

- *Source Noises*: are all the noises that depend on the sources present in the image.
- *Temporal Noises*: are all the noises that depend on the acquisition time of the image.
- *Electronic Noises*: are all the noises that depend on the electronic components of the device, or are related to them.

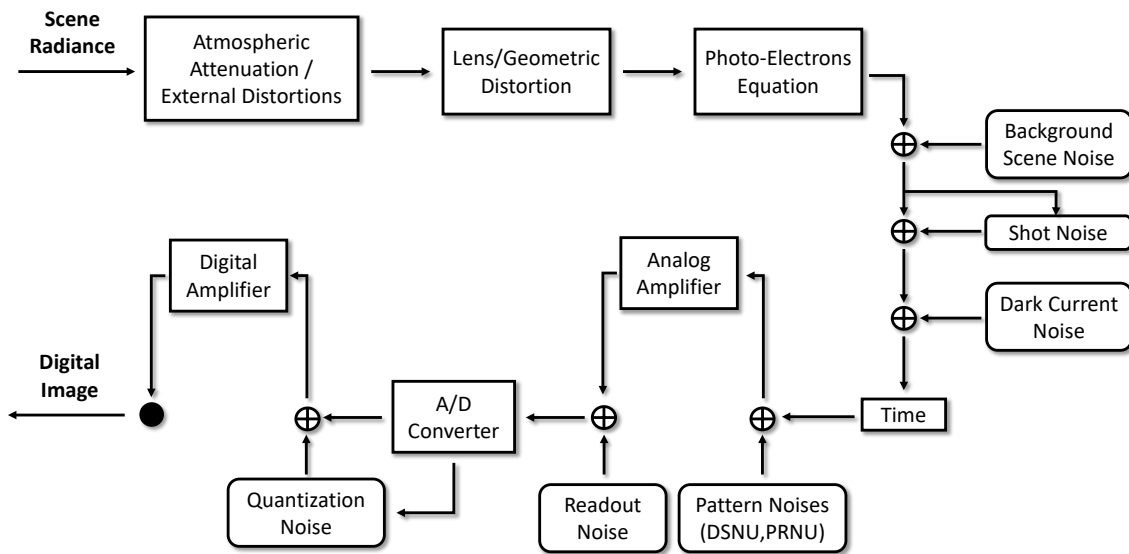


Figure 4.10: This figure schematize the typical imaging process workflow. Note that in the rounded boxes are reported the implemented noise sources, and in the squared boxes are reported the main working passages of an imagining simulation process.

The process of Camera Imaging, depicted in figure 4.10, helps to understand where the noises are introduced in the modelling process. Note that the presented imaging process is a simplified version created to illustrate the impact of the key noises in the operational workflow of a camera. In fact, the explanation of the complete working principle of the camera is not a goal of this section, and the details in the figure are retrieved from these

papers [50, 54, 71]; consequently, they will be not explained here.

Thus, the noises modeled in this work are: *Photon Shot Noise*, *Photon Response Non-Uniformity Noise (PRNU)*, *Dark Signal Noise*, *Dark Signal Non-Uniformity Noise (DSNU)*, *Quantization Noise*, *Readout Noise*.

Two main factors govern the selection of these noises. Firstly, they prove to be some of the most impactful in the image simulation process, as reported in [57]. Secondly, the model for these noises needs to be implemented using only information commonly found in sensors and camera datasheets, along with parameters from scenario simulations such as device temperature and background noise sources. As a consequence, the models of noise introduce an approximation to reproduce their correct working principle only with datasheet retrievable parameters<sup>1</sup>. Thus, allowing to avoid any further experiments with devices, which would often be impracticable during any preliminary or initial design phases.

It is worth pointing out that every camera has different noise parameter values. Specifically, there are often important differences in the physics of the noise generation between the two most used types of camera sensors, the Charge Coupled Device (*CCD*) and the Complementary Metal Oxide Semiconductor (*CMOS*). These differences are analyzed in detail in the following sections, and in addition to the technological advancement, they are examined in the reference [39–43, 46].

### 4.3.1. Photon Shot Noise

The Photon Shot Noise is a *source dependent noise*, which means that it is conditioned by the intensity of the signal itself. In particular, this is the most effective noise in image acquisition and often characterized the accuracy limit in light detection by a device<sup>2</sup>. This noise source affects equally any photodetector, so it is the same for CCD e CMOS sensors because it is due to the quantum nature of light that, when detected, produces a random fluctuation of measurement expressed through a probability distribution.

The probability distribution that best describes photon arrival events is the Poisson Distribution, reported in equation 4.8. Where,  $\lambda$  is the mean signal level, and  $k$  is the observed signal level, both evaluated in [*photons*];  $P(k)$  is the probability that there are  $k$  events. Nevertheless, in case of long exposure or high levels of light sources, in particular with more than 1000 arrival events of photons [36], it is possible to approximate the Poisson Distribution with a Normal Distribution with standard deviation equal to the square root

---

<sup>1</sup>Note that, unfortunately, the datasheet parameters of sensors and cameras are not standardized, then could be required to ask additional information to the manufacturers.

<sup>2</sup>It is still possible to implement several denoising procedures to decrease the effect Photon Shot Noise, for example multiple acquisition can be a valid denoising strategy.

of the expected number of photons.

$$P(k) = \frac{\lambda^k e^{-\lambda}}{k!} ; \quad (4.8)$$

Thus, the absolute value of photon shot noise increases with the expected number of collected photons, but its significance diminishes in brighter scenes since the signal increases with a faster rate.

In general, many different light sources can affect the detected scenario, depending also on the camera's position and direction during the observations. Since there are a large number of possible sources that can be simulated, only two light sources are selected to simulate the most common scenario with star trackers.

Before explaining the procedure introduced, it is fundamental to point out that this noise, even if it is proper of the photon nature, is applied on the photoelectron detection, hence on the electrons detected by the sensor. The reason for this choice is due to the nature of the photon detection; in fact, the fluctuation given by this distribution can be applied to the effective detection of photons, which in the case of the camera device is the photoelectron signal detection<sup>3</sup>. This option also allows to include the quantum efficiency of the device in the computation, as reported in [1, 3].

Primarily, the starlight is simulated through the procedures in Chapter 2. These sources can be computed individually, and their noise can be adapted singularly to optimize the simulation for every star in the scenario. Note that the global value of Photon Shot Noise in the simulated image depends on the average of all sources present; therefore, since stars are the brightest sources considered in this work, this value will increase when a larger number of stars is placed in the scene.

Secondly, the background light source present in the image can be affected by several contributions, such as: Zodiacal Light, Galaxies, Stray Light from planets and moons, Sun, and Cosmic Rays. Subsequently, in this work, it is considered a single value to approximate the resulting combination of all the possible background sources. However, for common scenarios, this strategy involves that the most significant parameter simulated is the Zodiacal Light of the space. The reason for this choice is mainly due to the possibility of easily identifying this value, knowing only the approximate location where the camera will have to work. Based on this approximation, it is also possible to consider the average Sky Glow when the simulation has to be performed for a camera operating on Earth or, in general, on a planet; in this case, some useful data can be retrieved by [21].

---

<sup>3</sup>As the reference [1] establish, this consideration required the assumption of linear image sensor. Otherwise, this consideration is no longer valid, and one must instead account for the number of photons.

In detail, the procedure followed starts with the computation of the average background source, reported in equations 4.9, which result corresponds to the Specific Intensity, or Spectral Radiance, of Zodiacal Light, evaluated as  $[\frac{photons}{s \cdot m^2 \cdot arcsec^2}]$ . Where,  $\lambda_{ZL1}$  and  $\lambda_{ZL2}$  are the boundaries of integration of the Spectral Zodiacal Light, written as  $f_{ZL}(\lambda)$ ;  $E_{zodiacal\ light}^{mag=22.1}$  is the Zodiacal Light photons flux<sup>4</sup>, evaluated in  $[\frac{photons}{m^2 \cdot s \cdot arcsec^2}]$ .

Note that the term (mag = 22.1) means that this value corresponds to the photon flux of an equivalent source with a visual apparent magnitude equal to 22.1. Afterwards, the computation proceeds with the computation of the angular pixel resolution of the specific camera with equation 4.10. Where,  $FOV_H$  and  $FOV_V$  are respectively the horizontal and vertical Field of View of the camera, evaluated in  $[arcsec]$ ;  $n.pix_H$  and  $n.pix_V$  are the number of active pixels<sup>5</sup> in the sensor;  $pixel_{res}$  is the value of pixel resolution, measured in  $[\frac{arcsec}{pixel}]$ . Then, these results are applied to compute the Zodiacal Light Photoelectron Flux in the specific scenario of the simulation, so like in equation 3.1. Nonetheless, some adjustments need to be reported in order to compute the background signal value for every pixel of the scene, resulting in equation 4.11. Where,  $\lambda_{C1}$  and  $\lambda_{C2}$  are the extremities of wavelength detection of the camera considered;  $S_{ZL}$  is the final value of the background light signal, evaluated in  $[\frac{e^-}{pixel}]$ .

This procedure is modified starting from the procedure present in the reference [25], whereas the data regarding Zodiacal light are reported from [14] and shown in the figure 4.11.

$$E_{zodiacal\ light}^{mag=22.1} = \int_{\lambda_{ZL1}}^{\lambda_{ZL2}} \frac{f_{ZL}(\lambda)}{hc/\lambda} d\lambda ; \quad (4.9)$$

$$pixel_{res} = \frac{FOV_H}{n.pix_H} \cdot \frac{FOV_V}{n.pix_V} ; \quad (4.10)$$

$$S_{ZL} = \frac{\pi}{4} \cdot D_{cam}^2 \cdot time \cdot \int_{\lambda_{C1}}^{\lambda_{C2}} \frac{f_{ZL}(\lambda)}{hc/\lambda} \cdot QE(\lambda) \cdot \tau_{opt}(\lambda) d\lambda ; \quad (4.11)$$

---

<sup>4</sup>Note that the term "flux" is used only to facilitate the understanding of the parameter, in fact as previously reported it is a Specific Intensity of Photons.

<sup>5</sup>Note that it is considered a sensor with a Fill Factor equal to 1; otherwise, this equation need to contain also the influence of the sensor Fill Factor.

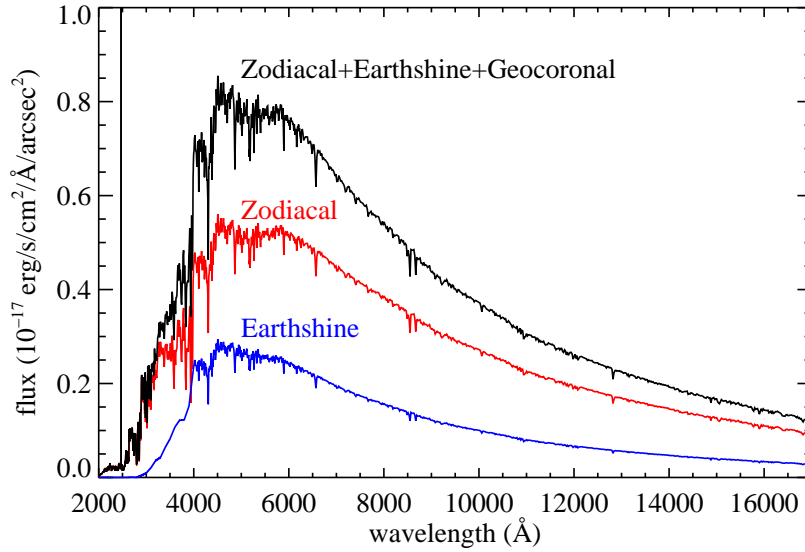


Figure 4.11: This figure shows the spectral flux densities of background noises in near-Earth orbits. Source: reference [14]

Finally, these noises are modelled in two steps, described for the developed MATLAB program.

The first step consists of adding the average background signal noise ( $S_{ZL}$ ), already evaluated in  $[\frac{e^-}{pixel}]$ , in all the pixels of the simulated image. Instead, the second step is to replace the previously calculated values of detected photons in the simulated image with the number of photoelectrons corresponding to the Poisson Distribution for each individual pixel, representing the brightness fluctuations of any stellar source. This procedure is performed thanks to the MATLAB command: `poisdrnd(Signal)`. Where,  $S$  is the final signal of a pixel, in photoelectrons, and this computation is repeated for any pixel in the image.

### 4.3.2. Dark Signal Noise

The Dark Signal Noise is a *temporal dependent noise*, which means that it is conditioned to the observation time of the device. In particular, this noise is mainly dependent on the temperature of the device, and it is one of the major sources of noise that limits the long exposure of cameras. This noise is present even if no light is incident, in fact, the Dark Current of the sensor determines it and increases exponentially with the increase of the operating temperature of the device.

The Dark Current noise source is present in any photodetector but affects the CCD and

CMOS sensors differently. In particular, dark current is the thermally generated electrons that generally arise from surface defects in the silicon semiconductor layer of the photodetector. The physical explanation of the Dark Current generation is complex and requires accurate knowledge of the camera sensor structure and working principles. Some references help to understand these topics [22, 45].

Thus, a very simplified explanation is proposed. Mainly, the Dark Current ( $De^-$ ) generation comes from defects in the semiconductor junctions, like p-n junctions, and defects in the materials interfaces between the different layers, like the Si/SiO<sub>2</sub> interface, which cause the diffusion of electrons. Then, the main contributions of Dark Current are: *Diffusion Dark Current* and *Depletion (or Bulk) Dark Current*. The Diffusion Dark Current is due to material interface defections that randomly decrease or increase the energy band gap for any sensor, which means that it is different for each sensor but constant inside the sensor. Instead, the Depletion Dark Current is due to defections in the semiconductor junctions, which generates unforeseen electrons generation-recombination in the depletion region, which is different for any sensor and any pixel in the sensor. The equation 4.12 resumes the dependencies in this noise generation, and a more detailed description of the parameters and the procedures to obtain this formula are explained in [77]. Where,  $T$  is the temperature of the sensor;  $k$  is the Stephan-Boltzman constant;  $E_{\text{gap}}$  is the band-gap energy needed for the sensor, typically it is used the value for Silicon (*Si*) and varies with the temperature;  $De_{0,\text{diff}}^-$  is the reference parameter for dark diffusion electrons generation, depends by manufacturing impurities and it is typically an experimental value;  $De_{0,\text{dep}}^-$  is the reference parameter for dark depletion electrons generation, depends by impurities and manufacturing design parameters and it is typically an experimental value. In summary, this procedure underlines that both noise sources are strictly generated by the thermal energy in the sensor and the unavoidable manufacturing impurities of the sensor components. Furthermore, it is noted that for low temperatures, up to almost room temperature (293.15 [K]), the Depletion Dark Current is dominant, and for high temperatures the Diffusion Dark Current is dominant.

$$De^- = De_{0,\text{diff}}^- \cdot T^3 \cdot \exp\left(-\frac{E_{\text{gap}}}{kT}\right) + De_{0,\text{dep}}^- \cdot T^{3/2} \cdot \exp\left(-\frac{E_{\text{gap}}}{2kT}\right) \quad (4.12)$$

The Dark Current generation description is generally valid for any sensor, including CCD and CMOS; however, its relevance is strictly related to the working principle, the manufacturing process, and the materials of any sensor. Consequently, with this level of detail, it is difficult to evaluate this noise for any camera, avoiding setting a specific experiment to retrieve the necessary parameters. Thus, it becomes essential to retrieve a simplified

procedure needs to be performed.

Since the dark signal noise is one of the primary sources of noise specific to any camera sensor, it is often reported as a noticeable parameter in most sensors' datasheets. Thus, it is possible to model how the Dark Signal varies with the trend of the sensor temperature using Datasheet information, like in figure 4.12 retrieved from the Datasheet of Teledyne Camera: CCD47-20, reported in [69]. It is worth pointing out that in some cases, these values could not be present for any working temperature of the sensor, in that cases it is still possible to use a simplified procedure, modelling the Dark Signal trend with Temperature with Arrhenius Law, as performed in [77] for CCD and in [2] for CMOS. Consider that in reality the Dark Signal depends not only on temperature but also on other parameters like the Substrate Voltage of the detector, whose dependency, in this case, is also reported in [69]. In any case, for this work's aim, the Dark Signal Noise is approximated depending only on sensor temperature and retrieved from Datasheet information.

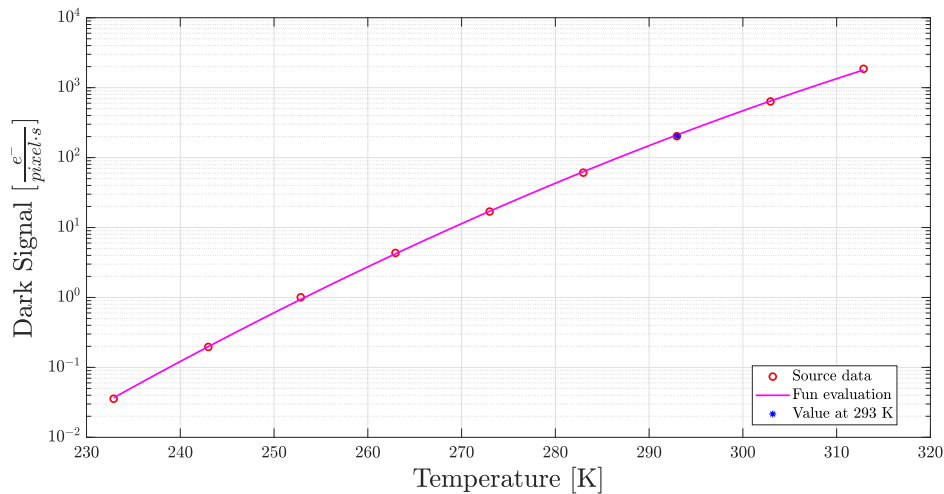


**Figure 4.12:** This figure shows the trend of Dark Signal noise as sensor temperature changes for CCD47-20 detector. Source: retrieved from reference [69]

Finally, the Dark Signal Noise is simulated for the desired working temperature; in this work, it is used a Sensor Temperature of 293 [K], for which the Dark Signal Noise is equal to almost 200 [ $\frac{e^-}{pixel \cdot s}$ ]. Then, it is multiplied by the observation time of the detector to evaluate the Dark Signal Noise during the entire image acquisition time.

Once the evaluation of the total Dark Signal is computed, it is important to underline that, assuming the uniform temperature of the sensor, this noise is considered equal for all the sensor's pixels. Similarly to the Photon Shot Noise, the Dark Signal can be represented as a shot noise due to the random arrival of the generated electrons and, therefore,

is described through a distribution across the sensor's pixels. For this work, the Poisson distribution, shown in equation 4.8, is selected to model the spreading of this noise. The selection of this particular distribution follows almost the same reasoning reported for Photon Shot Noise. In fact, since the Dark Signal Noise can be represented as the detection of an event, in this case detection of an electrons' signal, the Poisson distribution can properly represent these noises, as reported in [38]. Thus, the computation of this noise corresponds to adding the Dark Signal Noise to all the pixels, but following the Poisson Distribution, so with the MATLAB command: `poisdrnd(Signal)`. Where,  $S$  is the Dark Signal of a pixel, evaluated in  $\frac{e^-}{pixel}$ , hence, this computation is performed for the entire simulated image.

It is important to underline out that the Poisson distribution is used in this model to simulate both CCD and CMOS sensors. However, since this noise depends on the technology adopted by the sensor, its working principles, and the manufacturing process, which can therefore also vary significantly between sensors, there are also other distributions that can represent this noise, but some experiments must often be performed to identify the most suitable ones. In particular, in the work of reference [6], the Gamma distribution is identified as the distribution that best fits Dark Signal Noise of a selected CCD sensor. Meanwhile, the Log-Normal Distribution is identified as the best for a selected CMOS sensor. The necessity of running tests to determine the best distribution is one of the main reasons why the Poisson distribution is chosen a priori to represent each sensor in general.

### 4.3.3. Non-Uniformity Noises

The Non-uniformity noises vary between sensors but remain fixed for all the images of a single sensor; this is why they are also called Fixed Pattern Noises (*FPN*). Essentially, the cameras' detectors have two basic non-uniformity behaviours: the Photo Response Non-Uniformity (*PRNU*) and the Dark Signal Non-Uniformity (*DSNU*).

Specifically, the *PRNU* noise is a *source noise* which is proportional to the input signal of the sensor and causes spatial inhomogeneity of signal in the detected images, even if a uniform source is detected over the entire sensor<sup>6</sup>. Instead, the *DSNU* noise is a *temporal noise*, since it is proportional to the dark signal noise and causes spatial inhomogeneity in that noise. These noises are characterized by a common source definition, that is, the pixels manufacturing inhomogeneities. In the case of *PRNU*, the main inhomogeneity is caused by the surface area variations between photodiodes, mainly due to substrate

---

<sup>6</sup>A uniform source over the whole sensor is commonly called Flat Field and is one of the principal ways to test a sensor in order to establish the *PRNU* noise.



material variations during the sensor fabrication, as reported in [12]. Regarding *PRNU*, instead, the pixels inhomogeneities are mainly addressed to surface defects in the sensor material interface, like SiO<sub>2</sub>/Si one, and to the discrete randomly distributed charge generation centers, as reported in [5, 63]. Consequently, these two noise sources cause a random spatial distribution of error across the pixels' sensor that must be simulated to allow a more reliable simulation of the images.

These noises are common for all the sensors, CCD and CMOS, but the spatial distribution outcomes differ due to the distinct working principles and manufacturing of the two sensor types, as depicted in figure 4.13. In particular, the CMOS sensors suffer of pixels *FPN*, so random spatial distribution between pixels, amplified by the inhomogeneities introduced by the pixel transistors. Further, it is also affected by column *FPN* given by the inhomogeneities of column amplifiers, which cause an additional stripes error behaviour. Instead, the CCD sensor suffers only of pixels *FPN*, since the different working principles allow to avoid the pixel transistors and the use of several amplifiers. It is worth pointing out that these are only the main sources of these noises; in addition, the impact and the properties of this noise can vary during the generations of cameras since the manufacturing process improves over the years, as stated from the references regarding CCD-CMOS comparison ([39]-[43]).

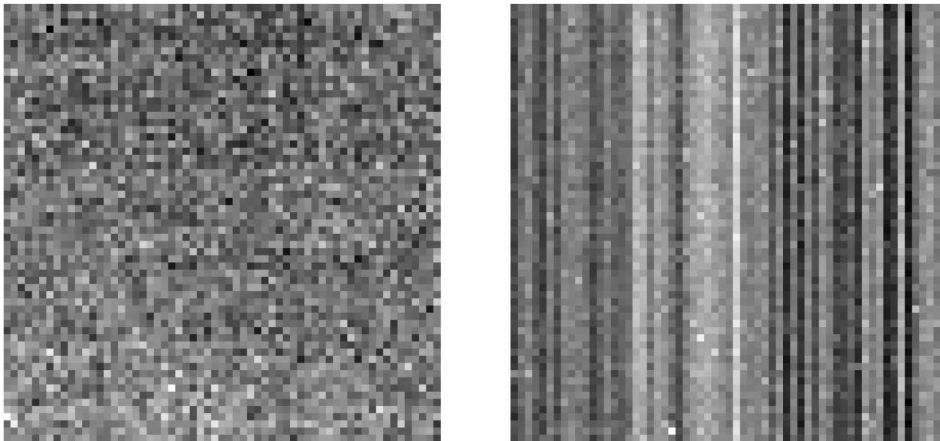


**Figure 4.13:** These figures show the particular pattern of DSNU noise for cameras. In particular, the figure on the left shows the pattern noise of Active Pixel Sensor (APS), typical of CCD detector; the figure on the right shows the pattern noise of Passive Pixel Sensor (PPS), typical of CMOS detector. Source: retrieved from reference [34]

After describing these noises, a model to simulate them is required. Since the outcome of the two noises is similar, the two spatial distributions that represent a Fixed Pattern

distribution can be modelled in the same way. In particular, a non-uniform spatial distribution that represents the defect errors of the pixels is equivalent to a white noise behaviour. This white noise can be modelled through a Gaussian distribution around zero means and with a standard deviation that can represent the intensity level of these noises, as performed in references [28, 72].

The intensity level of both noises, *PRNU* and *DSNU*, are often defined in the datasheet of cameras. In fact, their computation represents one of the standard tests that manufacturers perform to describe the product specifics, as stated in [49, 69]. In particular, in the case of *PRNU* noise, it is evaluated a multiplication coefficient, measured in point percentage [%], to multiply the signal value of the expected image, assessing the *PRNU* noise intensity. Instead, the multiplication noise uses a *DSNU* coefficient, evaluated in [%] or directly in  $[\frac{e^-}{pixel.s}]$ , to multiply the total amount of Dark Signal, assessing the *DSNU* noise intensity.

Finally, these noises are introduced in the simulated image by adding the Gaussian distribution, representing the white noise models, over all the pixels' signal of the image. The computation is performed thanks to the MATLAB command: `normrnd(FPN – Intensity)`. Where, `FPN – Intensity` is the level intensity considered for these two noises, evaluated in  $\frac{e^-}{pixel}$ . It is worth pointing out that in the case of multiple images simulation, it is more accurate to evaluate a fixed Gaussian distribution to simulate the fixed pattern property that remains invariable for images of the same device.

#### 4.3.4. Quantization Noise

The Quantization noise is an *electronic noise*, which means that it derives from the electronic components of the camera. In this case, this is a computational error introduced by the Analog to Digital Converter (*ADC*) component that translates the analog information from the sensor into digital numbers to compose the image. In particular, the quantization noise represents the truncation error given by the effective quantization of the digital signal during its conversion, as depicted in figure 4.14. Note that this particular noise is not dependent on the sensor type, since it is created by an electronic component common to all the cameras. However, it is dependent on some characteristics of the camera, in particular the parameters of *Quantization Bits* used to represent the digital unit of the image, and the *Full Well Charge* of the detector, which defines the maximum number of electrons that a single pixel can collect during the image acquisition.

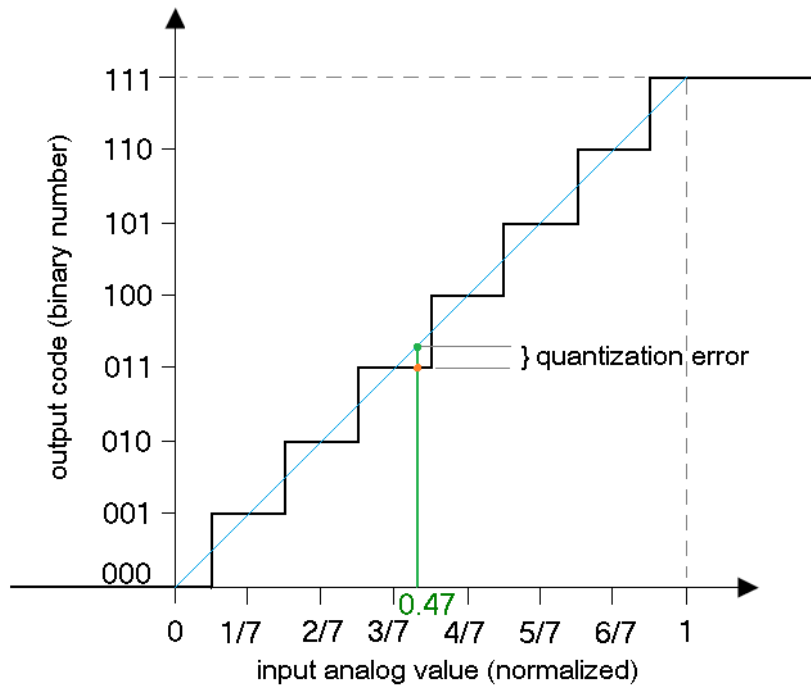


Figure 4.14: An ideal 3 bit A/D converter. A/D response is shown in black, Cyan curve would be the A/D conversion if no quantization error is considered. Source: reference [22]

The modelling of the quantization noise needs to evaluate the two main parameters for the digital conversion, which are selected based on the characteristics of the scenario observed by the camera. Specifically, this noise cannot predict in which direction the rounding error will be performed, so it is necessary to define the resolution of the A/D converter. These parameters are very important to structure the image simulator since they are also needed to perform the analogue-to-digital conversion of the simulated signal. Consequently, a camera datasheet always states the Full Well Charge parameter. Instead, the quantization bits are freely chosen based on the typical application of the camera; for example, since a high signal resolution can be worthwhile for star trackers, the typical values are from 8 up to 16 quantization bits.

Finally, this error must be modelled following a distribution capable of representing a random behaviour of the rounding error around the simulated signal. Then, it is simulated through a Gaussian distribution with zero mean and standard deviation derived by the A/D converter resolution, estimated for every pixel of the image. Thus, the results are added to the signal of the simulated image, and the computation is performed thanks to the MATLAB command: `normrnd( $N_{ADC}$ )`. Where,  $N_{ADC}$  is a statistical evaluation of the ADC resolution.

### 4.3.5. Read-Out Noise

The Read-Out Noise is a particular *electronic noise*, which sums up all the noise of the electronic components that are present in the camera. Expressly, it represents the total electronic noise generated during the production of the image signal, starting from the electron detection in the sensor.

Note that this noise is not dependent on the source or the time acquisition of the image but depends only on the sampling frequency of the device, as shown in figure 4.15. Specifically, this noise is proper for any camera and is generally affected by the same electronic components for CCD and CMOS. Furthermore, it affects more CMOS sensors than CCD sensors due to the working logic of the CMOS sensor, which uses a more significant number of electronic components.

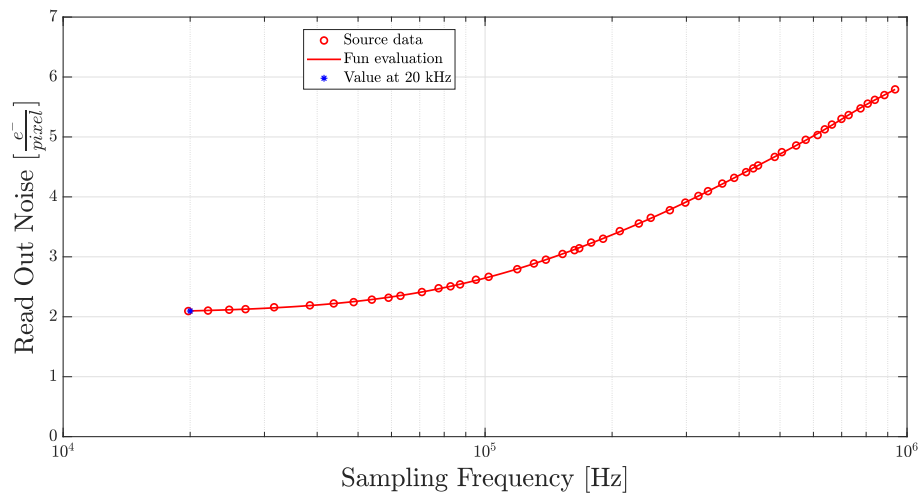


Figure 4.15: This figure shows the trend of Read-Out noise as sampling frequency changes, for the CCD47-20 sensor. Source: retrieved from reference [69]

In general, the Read-Out Noise describes the minimum noise present in a camera for any image acquisition performed and comprises a multitude of different noise sources considered as system electronics noise, like the ones described in this reference [44]. In particular, it is also considered the contribution of the dark *FPN* and shot noises, the quantization noise, and other noises that are already considered independently in this work. Consequently, during the selection of the Read-Out noise, commonly retrieved by the detector datasheet since it represents a basic parameter of every sensor, it is observed from which contributions it is retrieved and corrected to obtain only the general noise of the system electronics components not considered yet.

Finally, to model this noise, it is necessary to consider that electronic noises generate

zero mean noise, which can be modelled as white noise, as stated also in [13, 32, 44]. Then, a Gaussian distribution is used to simulate this model in every pixel of the image, since they are uniformly affected by the same number of electronic components, thanks to the MATLAB command:  $normrnd(N_{\text{readout}})$ . Where,  $N_{\text{readout}}$  is the signal intensity of the Read-Out noise, evaluated in  $\frac{e^-}{\text{pixel}}$ . Note that Read-Out noise, when generated by particular electronic components, like amplifiers, does not have a constant noise value but oscillates around an average value. Then, the intensity of this noise is evaluated through a signal root mean square computation (*r.m.s.*) of the fluctuations, as reported in [69].

### 4.3.6. Application of noise models

The combined application of all the camera noise models described in the previous sections in the star image simulator allows to represent a high-fidelity image simulation for cameras. Especially for the simulation of scenarios observed by a star tracker in a deep-space environment. It is worth pointing out that all the models for camera noise were developed by trying to use only the values available from the sensor datasheets, thus allowing the development of a model with high-fidelity and reliable data and avoiding obtaining the data through camera tests. This choice enables the use of this simulator in all phases of mission design or research while maintaining the trustworthiness of the simulated parameters. Therefore, in order to perform the simulation, it is selected a specific camera sensor, that is, the Teledyne CCD47-20,BI,AIMO [69]. The selected sensor is a very famous high-TRL detector with a long list of missions heritage in Planetary Explorations, Earth Observations, Ground Astronomy and Space Astronomy, often used also as a navigation camera and star tracker, as reported in [70].

## Noise Models Summary

The implementation of the models and their error distribution are already discussed in the previous section, then now are summarized with the complete formulation of the error parameters and their selection. The table 4.1 reports all the implemented noises and the parameters extracted by the sensor datasheet. It is important to point out that the implementation of these noises follows the same workflow<sup>7</sup> depicted in the figure 4.10.

---

<sup>7</sup>Note that the Atmospheric Attenuation is not considered a camera noise model, and is applied only for simulations of ground observations.

Noises	STD Formula	Distribution
Photon Shot Noise	$n_{\text{SHOT}} = \sqrt{S_{\text{avg,SHOT}}}$	Poisson
PRNU Noise	$n_{\text{PRNU}} = \sqrt{S_{\text{avg,SHOT}} \cdot \sigma_{\text{PRNU}}}$	Gaussian (White)
Dark Signal Noise	$n_{\text{DS}} = \sqrt{I_{\text{dark}} \cdot \text{time}}$	Poisson
DSNU Noise	$n_{\text{DSNU}} = \sqrt{I_{\text{DSNU}} \cdot \text{time}}$	Gaussian (White)
Quantization Noise	$n_{\text{ADC}} = \frac{N_{\text{well}}}{2^q \cdot \sqrt{12}}$	Gaussian (White)
Read-Out Noise	$n_R = I_R$	Gaussian (White)

**Table 4.1:** This table reports all the formulas for the Standard Deviation computation of the noise models implemented in this work, along with the distribution model selected for each noise.

Thus, it is reported the definition of the parameters expressed in Table 4.1, and then will be reported the necessary procedures for their computation. Where,  $S_{\text{avg,SHOT}}$  is the average signal value of the simulated image, evaluated in  $[e^-]$ ;  $\sigma_{\text{PRNU}}$  is the multiplication coefficient of the *PRNU* noise;  $I_{\text{dark}}$  is the value of the Dark Current present in the sensor, evaluated in  $[\frac{e^-}{\text{pixel}\cdot\text{s}}]$ ;  $I_{\text{DSNU}}$  is the value of the Dark Current Non-Uniformity<sup>8</sup>, evaluated in  $[\frac{e^-}{\text{pixel}\cdot\text{s}}]$ ; *time* is the simulated observation time of the device, evaluated in  $[\text{s}]$ ;  $N_{\text{well}}$  is the Full Well Charge capacity of the sensor, evaluate in number of  $[e^-]$ ;  $q$  is the quantization bit of the Analog to Digital Converter, evaluated in  $[\text{bit}]$ ;  $I_R$  is the root mean square value of the Read-Out noise, evaluated in  $[\frac{e^-}{\text{pixel}}]$ . While, the computation of the parameters used is performed following the procedures explained in the respective noise section of this work. In particular, it is underlined the computation of the  $S_{\text{avg,SHOT}}$  value, that is performed through the equation 4.13. Where,  $S_{\text{avg,stars}}$  is the average value of all the stars' brightness signal, after the Point Spread Function procedure, evaluated in  $[e^-]$ ;  $S_{\text{avg,background}}$  is the average value of background signal simulated in the image, provided in section 4.3.1. Instead, the summary of the noise values retrieved for the selected camera datasheet, CCD47-20 [69], are shown in table 4.2. It is worth pointing

<sup>8</sup>Note that this value could be reported, in some cases, also as multiplication coefficient and behaves as the PRNU value ( $\sigma_{\text{PRNU}}$ ), but evaluated with the Dark Current ( $n_{\text{dark}}$ )

out that the Standard Deviation (STD) Formula is needed for the computation of all the noise distributions in the simulated image. Furthermore, it is possible to sum all these noises to evaluate the Total Noise Value of the image, through the equation 4.14. Where, all the noises are summed up as variance values and then are retrieved the final STD of the Total Noise ( $n_{TOT}$ ).

$$S_{\text{avg,SHOT}} = S_{\text{avg,stars}} + S_{\text{avg,background}} \quad (4.13)$$

$$n_{TOT} = \sqrt{n_{\text{SHOT}}^2 + n_{\text{PRNU}}^2 + n_{\text{DS}}^2 + n_{\text{DSNU}}^2 + n_{\text{ADC}}^2 + n_R^2} \quad (4.14)$$

Noises	Noise Value
Photon Shot Noise	$n_{\text{SHOT}} = \text{variable}^\dagger \frac{e^-}{\text{pixel}}$
PRNU Coefficient	$\sigma_{\text{PRNU}} = 0.03$
Dark Signal Noise	$I_{\text{dark}}^* = 203 \frac{e^-}{\text{pixel}\cdot\text{s}}$
DSNU Noise	$I_{\text{DSNU}}^* = 60 \frac{e^-}{\text{pixel}\cdot\text{s}}$
Quantization Noise	$n_{\text{ADC}} = \frac{70000 [e^-]}{2^{12[\text{bit}]} \cdot \sqrt{12}} = 4.93 \frac{e^-}{\text{pixel}}$
Read-Out Noise	$I_R = 2 \frac{e^- (r.m.s.)}{\text{pixel}}$

<sup>†</sup> The value of Photon Shot Noise strictly depends by the simulation scenario.

<sup>\*</sup> Computed for a reference sensor temperature :  $T = 293 [K]$ .

Table 4.2: Noise values computed from camera datasheet (CCD47-20).





## 5 | Presentation of results

This chapter will show the outputs of the simulator; the aim of these results is to display the quality of the simulated images and demonstrate the versatility in parameter selection.

In order to simulate some outputs, it is required to select the camera parameters, explained in chapter 4. For this aim, the sensor is selected: Teledyne CCD47-20,BI,AIMO [69]. The choice is consistent with the selection of the parameter noise implemented in section 4.3.6, and follows the same motivations. Thus, the main camera parameters utilized are listed in table 5.1, which are retrieved from the datasheet of the selected sensor [69]. However, not all the parameters are constant in the computations of the following results. In fact, some parameters are chosen singularly to simulate a particular scenario or a specific condition, such as: System Gain ( $Gain$ ), Focal Length ( $f$ ), Optical Aperture Diameter ( $D_{cam}$ ), Acquisition Time ( $time$ ), and Camera Boresight Direction ( $RA_0$ ,  $DEC_0$ ). Instead, other parameters, such as the Quantum Efficiency ( $QE$ ) and the Optical Transmissivity ( $\tau_{opt}$ ), since they are considered as spectral properties, are retrieved from a function evaluation of the data and shown, respectively, in the figures 5.1,5.2.

Subsequently, three different outputs are shown, where the camera parameters will be constant in the first two, while the noise parameters will be different in all of them. Specifically, the noise parameters of the third output are retrieved by the analysis of one picture, performed with the software PixInsight, and information retrieved from the NAVCAM of Rosetta mission, obtained from [4, 27].

Finally, the *first output* shows the simulation of the Orion Constellation from an observer in the deep-space and a low background noise presence, with a typical star tracker configuration; the *second output* shows the Lira Constellation from an observer in the deep-space and a higher background noise presence, with a different, narrowed, star tracker configuration; the *third output* shows the comparison of the simulation with the same scene reported from an image observed by a real camera in space.

Parameter	Value
Size sensor	13.3x13.3 [mm]
n. pixels	1024x1024 [pixel]
size pixel	13 [ $\mu m$ ]
$N_{well}$	10000 [ $e^-$ ]
$q_{bit}$	12 [bit]
$QE(\lambda)$	figure*
$\tau_{opt}(\lambda)$	figure†

\* Reported in figure 5.1.

† Reported in figure 5.2.

Table 5.1: This table listed all the fixed camera parameters used for the outputs computations.

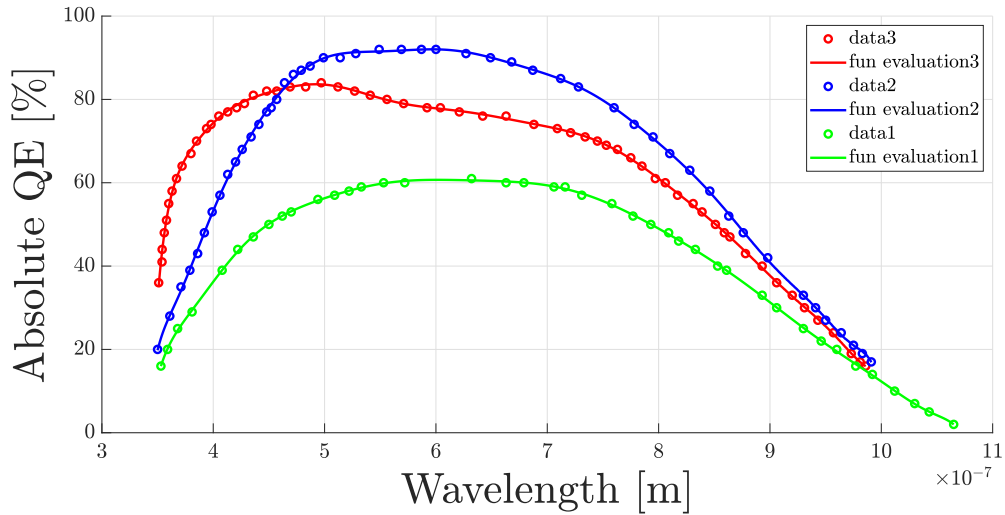


Figure 5.1: This figure shows the Spectral Quantum Efficiency for the CCD47-20, in several versions. In particular, the *red data* represent the Broadband Coated sensor version; the *blue data* represent the Midband Coated sensor version; the *green data* represent the Uncoated sensor version. The  $QE$  selected for the simulations is the Midband Coated version. Source: data retrieved from [69].

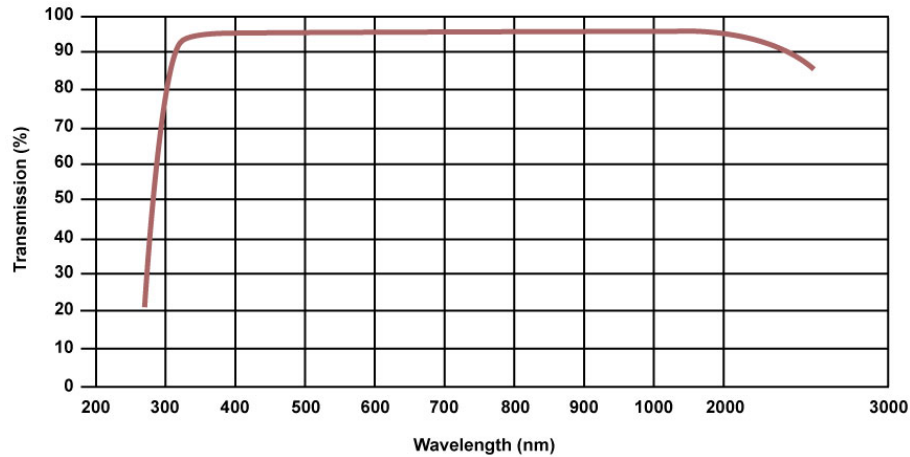


Figure 5.2: This figure shows the Spectral Transmissivity of optical components implemented, the BK-7 optical glass. Source: acquired from [29].

It is worth pointing out that for each output are shown the valuable results that make this simulator particularly worthwhile for the research on star tracker design and their algorithms training. In particular, are shown :

- *Centroid Position*: the plot that represents all the stars' centroid positions of the observed scene, retrieved by the catalog information and transformed in pixel coordinates of the observed scene.
- *Magnitude Stars*: the plot that lists all the stars' visual apparent magnitudes ( $m_v$ ) of the observed scene.
- *Temperature Stars*: the plot that lists all the stars' effective surface temperatures ( $T_{eff}$ ) of the observed scene.
- *Simulated Image - No Noise*: the figure represents the simulated image of the simulator without considering any noise source, then only with the *DGS* model for the brightness of stars.
- *Zoomed Simulated Image - No Noise*: the figure represent an enlarging of the simulated image, without Noise, in order to show details of the specific star simulations.
- *Simulated Image - With Noise*: the figure represents the simulated image of the simulator also considering the noise sources, then showing the complete simulation capability of this simulator.
- *Zoomed Simulated Image - With Noise*: the figure represents an enlarging of the simulated image, with Noise, in order to show details of the specific star and noise simulations.

## 5.1. First Output Simulation

The first output shows the simulation of an image acquisition of a camera in the deep-space with a low-level of background noise, in which is considered only the Zodiacal Light, retrieved in section 4.3.1. For this simulation are used the specific parameters shown in table 5.2. Thus, this output is computed to demonstrate the capability of the simulator to build an image and retrieve information for a very common background scenario. However, it is considered a simulation with some camera parameters that are not strictly characteristic of star trackers, like the large field of view and the focused image, but are typical of cameras used for space observation. Consequently, this result shows a possible simulation of a multipurpose camera that can be used for attitude determination and space observation, and both can be used for design purposes or for algorithms training. It is worth pointing out that the acquisition time (*time*) considered for this simulation is chosen to facilitate the observation of the stars in the reported figures, but it is rare in space cameras different from telescopes.

Parameter	Value
$D_{cam}$	0.03 [m]
$RA_0^*$	84.057 [deg]
$DEC_0^*$	-1.200 [deg]
$Gain$	24 [ $\frac{e^-}{ADU}$ ]
$f$	30 [mm]
$FOV_{x,y}$	25x25 [deg]
$time$	3.5 [s]
$S_{background}^\dagger$	$S_{ZL}$ [ $\frac{e^-}{pixel}$ ]
$\sigma_P SF$	0.55 [-]

\* Value reported in J2000 convention.

† Retrieved by equation 4.11, following the procedure developed in section 4.3.1.

**Table 5.2:** This table listed the variable parameters of camera models for the designed image simulation.

This output shows the capability of the simulator to be profitable for the research of multipurpose cameras. In fact, it is shown in figures 5.7 how is detailed the simulation of stars brightness, which are reported the star signal simulation of every star present in the Field of View (*FOV*), proportionally to their specific Spectral Irradiance during the observation. In figure 5.3, instead, is presented the centroid positions, in pixel coordinates, of all the stars present in the large *FOV*. These data, mixed with the output figures 5.4 and 5.5 can be used in the training of attitude determination algorithms, which usually does not handle this large amount of star simultaneously. For example, one application of these data can be in creating an algorithm that can recognize particular large patterns of stars based on the temperature and magnitude conditions, so on specific spectral Irradiance features. In conclusion, this output shows the capability of the simulator to show a particular scenario that a star tracker could afford during its mission, in the case of a multipurpose camera that varies the strict requirements of the observations.

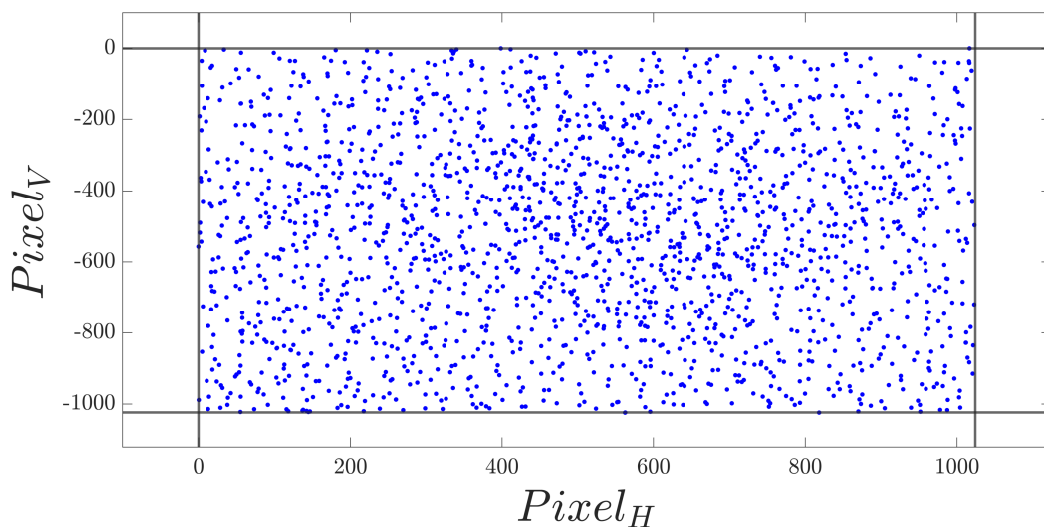


Figure 5.3: This figure shows the centroid stars coordinates (*blue dots*) of the designed image simulation. The black lines represent the limits of the synthetic image.

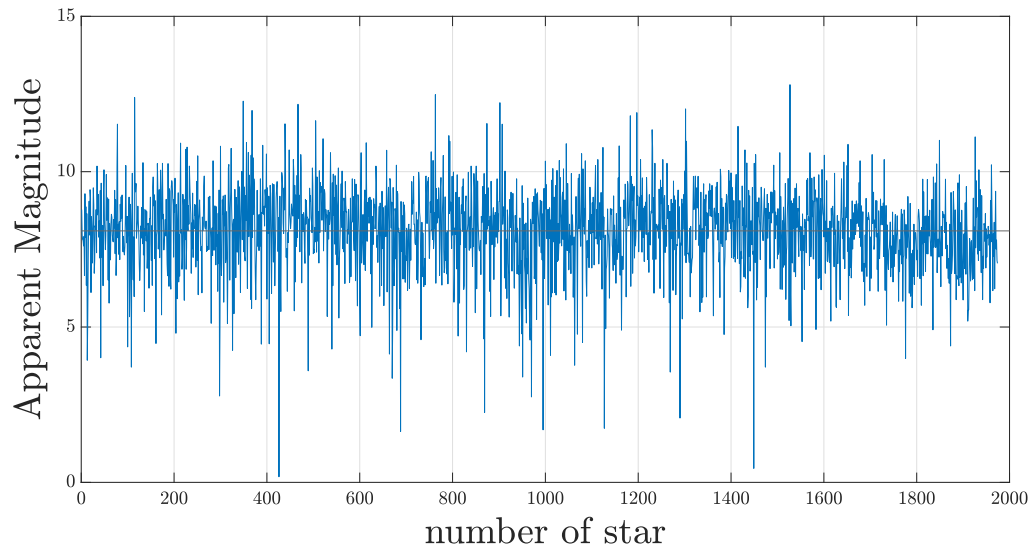


Figure 5.4: This figure shows the visual apparent magnitudes of the star simulated. This output shows the photometric parameters of the detected star for research purposes. The *black line* in the middle represents the average value of apparent magnitude in the scene.

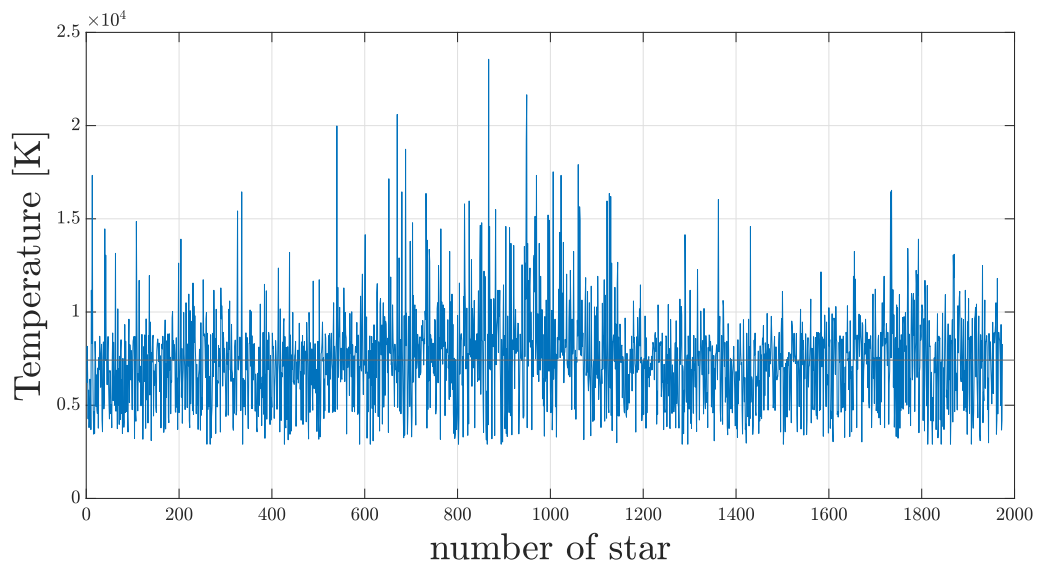
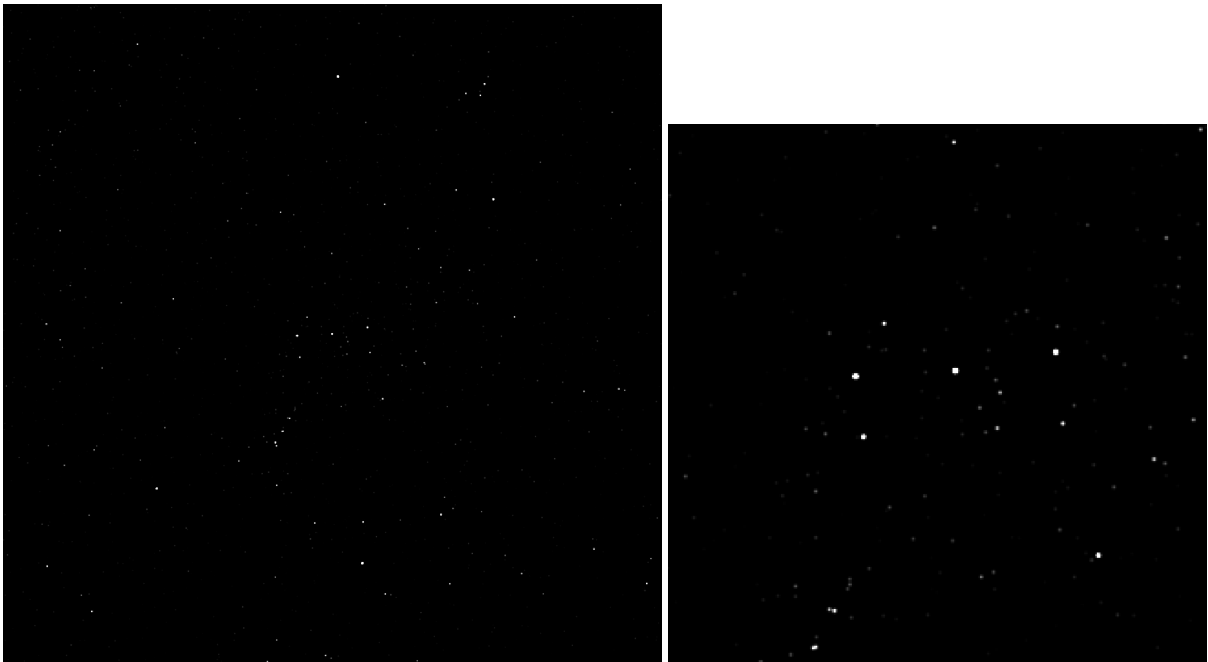


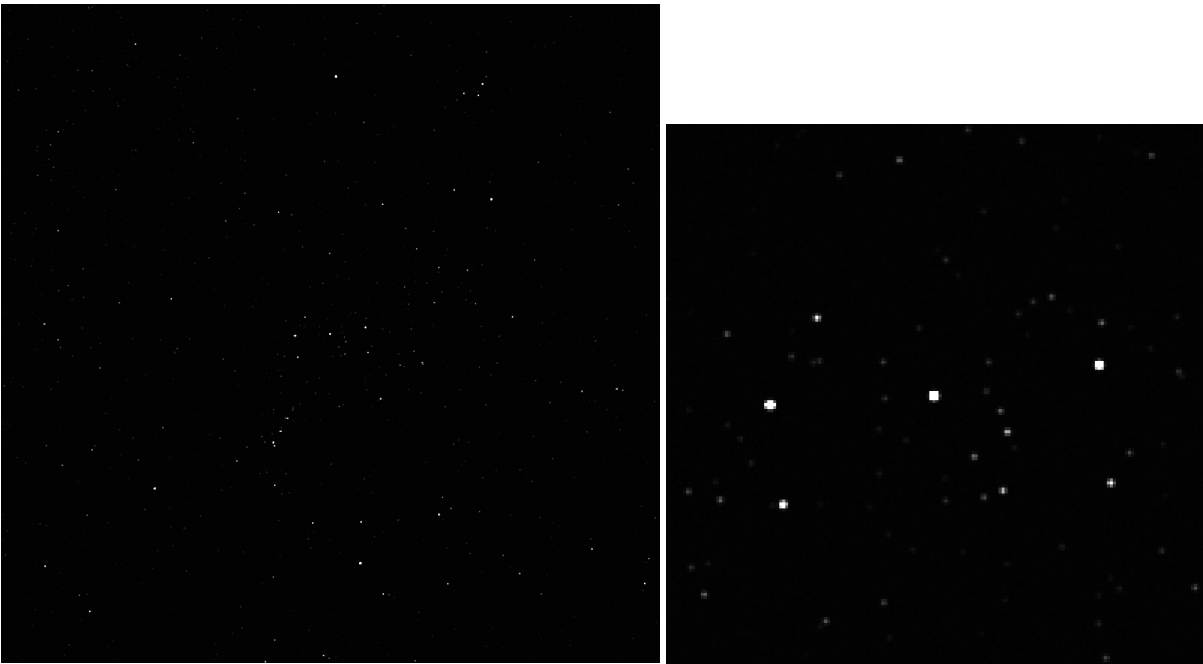
Figure 5.5: This figure shows the Effective Surface Temperatures of the star simulated. This output shows the photometric parameters of the detected star for research purposes. The *black line* in the middle represent the average value of stars temperature in the scene.



(a) This image represents the simulation of the Orion Constellation for a wide FOV camera, which shows almost entirely the constellation. In the center of the image is shown Alnilam, the central star of Orion's belt.

(b) This image shows a zoom of the Orion's belt, which allows to identify the presence of many other smaller stars in that region.

**Figure 5.6:** These images are the outputs of the star image simulator, which represent the simulation of an image acquisition from the modelled camera for a selected scenario, without noises modeling. The image on the left represents the full-size image. Instead, the image on the right represents zooming in on a particular detail. Note that the images are vertically tilted to simplify the visualization of the images.



(a) This image represents the same simulation of the Orion Constellation of figure 5.6a, but also considering the noises modelling. However, the effects of the noises are not easy to observe visually since they are modelled at a low noise level.

(b) This image shows a zoom of the Orion's belt, with the noises modelling included. Since it is modelled a low level of noise, only a slight difference in the shape of stars can be observed with respect to the zoom in image 5.6b.

**Figure 5.7:** These images are the outputs of the star image simulator, which represent the simulation of an image acquisition from the modelled camera for a selected scenario, also considering noises modeling. The image on the left represents the full-size image. Instead, the image on the right represents zooming in on a particular detail. Note that the images are vertically tilted to simplify the visualization of the images.



## 5.2. Second Output Simulation

The Second output shows the simulation of an image acquisition during an interplanetary mission with a middle-level of background noise, in which is considered a further general background source given by the proximity of an hypothetical celestial object. For this simulation are used the specific parameters shown in table 5.3. Thus, this output is computed to demonstrate the capability of the simulator to build an image and retrieve information from different background scenarios, typical for star trackers. In fact, it is considered a simulation with camera parameters strictly characteristic of star tracker, like the narrowed Field of View, the defocused image, and the small optical size. Consequently, this result shows a possible simulation for a star tracker camera and can be used for design and algorithms training. It is worth pointing out that the acquisition time (*time*) considered for the simulation is chosen to facilitate the observation of the stars in the reported figures, but it is not common in space cameras different from telescopes.

Parameter	Value
$D_{cam}$	0.03 [m]
$RA_0^*$	283.021 [deg]
$DEC_0^*$	35.349 [deg]
$Gain$	24 [ $\frac{e^-}{ADU}$ ]
$f$	70 [mm]
$FOV_{x,y}$	10.8x10.8 [deg]
$time$	5 [s]
$S_{background}^\dagger$	3000 [ $\frac{e^-}{pixel}$ ]
$\sigma_{PSF}$	0.85 [-]

\* Value reported in J2000 convention.

† This value is assumed as an average contribution from several background sources.

Table 5.3: This table listed the variable parameters of camera models for the designed image simulation.

These outputs show a classic use of the star image simulator, so the simulation of a stars field in a typical Field of View of a star tracker. Specifically, this classical use of image simulation includes the training of algorithms for attitude determination, star identification, pattern recognition, or centroid extraction for particular scenarios to which the device will be subjected during its mission. In particular, figures 5.11 and 5.12, with the data in figure 5.8, can be inputs of the algorithm training experiment for star identification and centroid extraction. Another feature can be shown by taking into account the difference between the outputs of section 5.1 and the outputs of this section, in which is noticeable the results of the easy parameters modification to produce diverse outputs under different conditions. Another result of these outputs is shown in figures 5.9 and 5.10, in which is possible to characterize the stars' properties for every simulated scenario.

In conclusion, this output shows the capability of the simulator to simulate scenarios with different cameras and background parameters, hence allowing to simulate different phases of a satellite's mission.

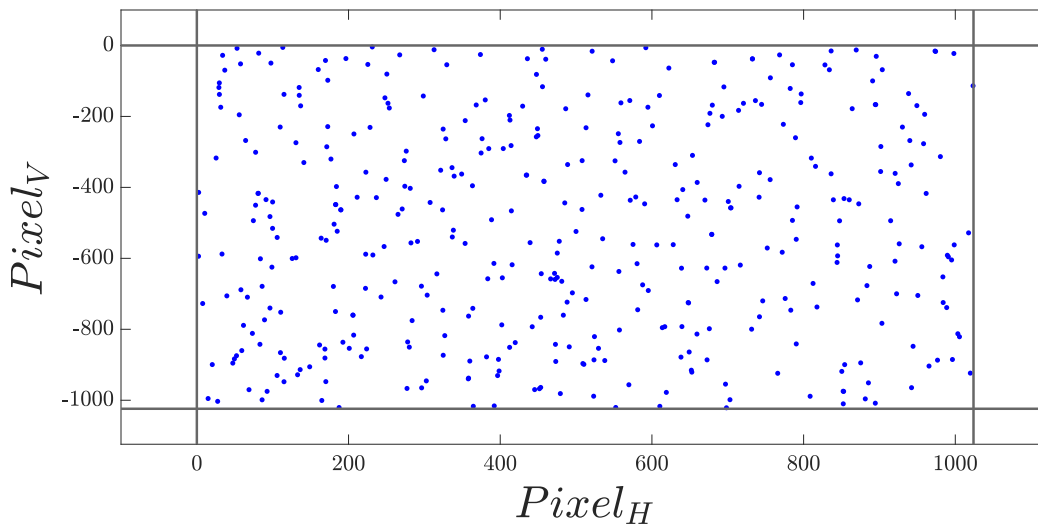


Figure 5.8: This figure shows the centroid stars coordinates (*blue dots*) of the designed image simulation. The black lines represent the limits of the synthetic image.

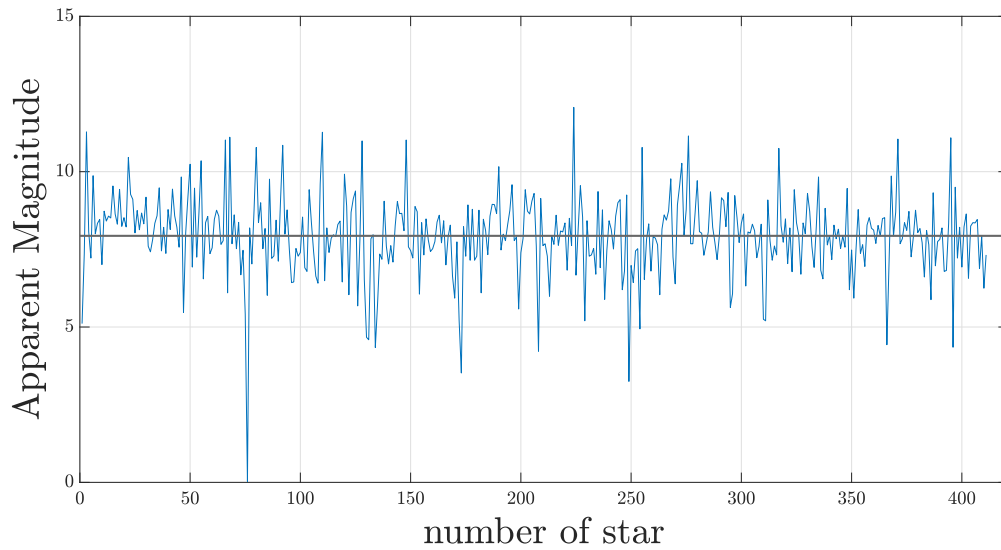


Figure 5.9: This figure shows the visual apparent magnitudes of the star simulated. This output shows the photometric parameters of the detected star for research purposes. The *black line* in the middle represents the average value of apparent magnitude in the scene.

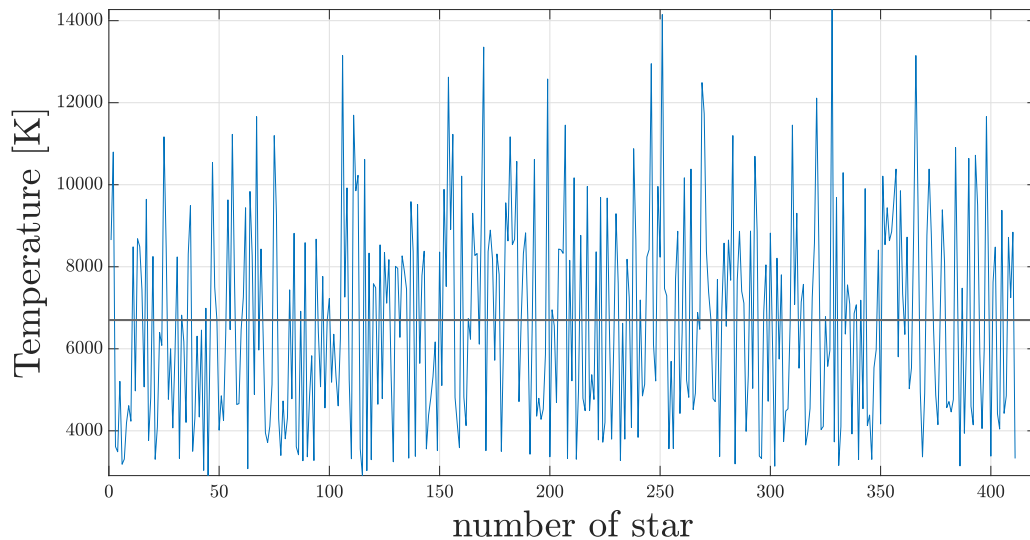
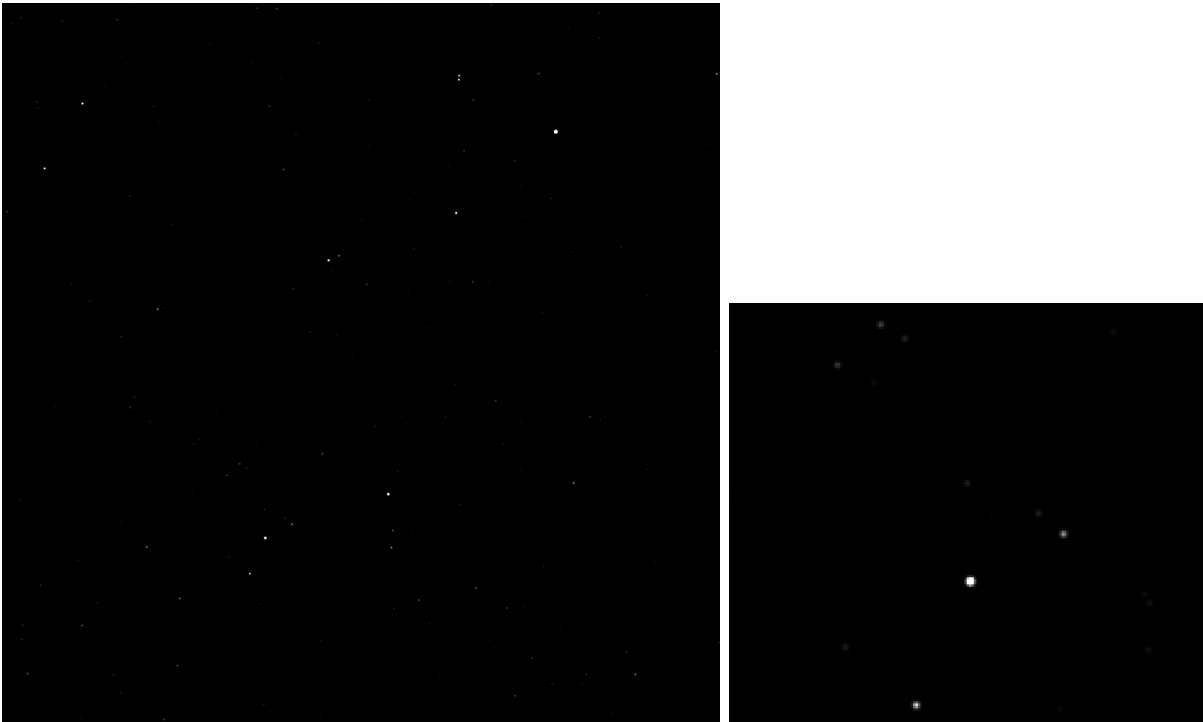


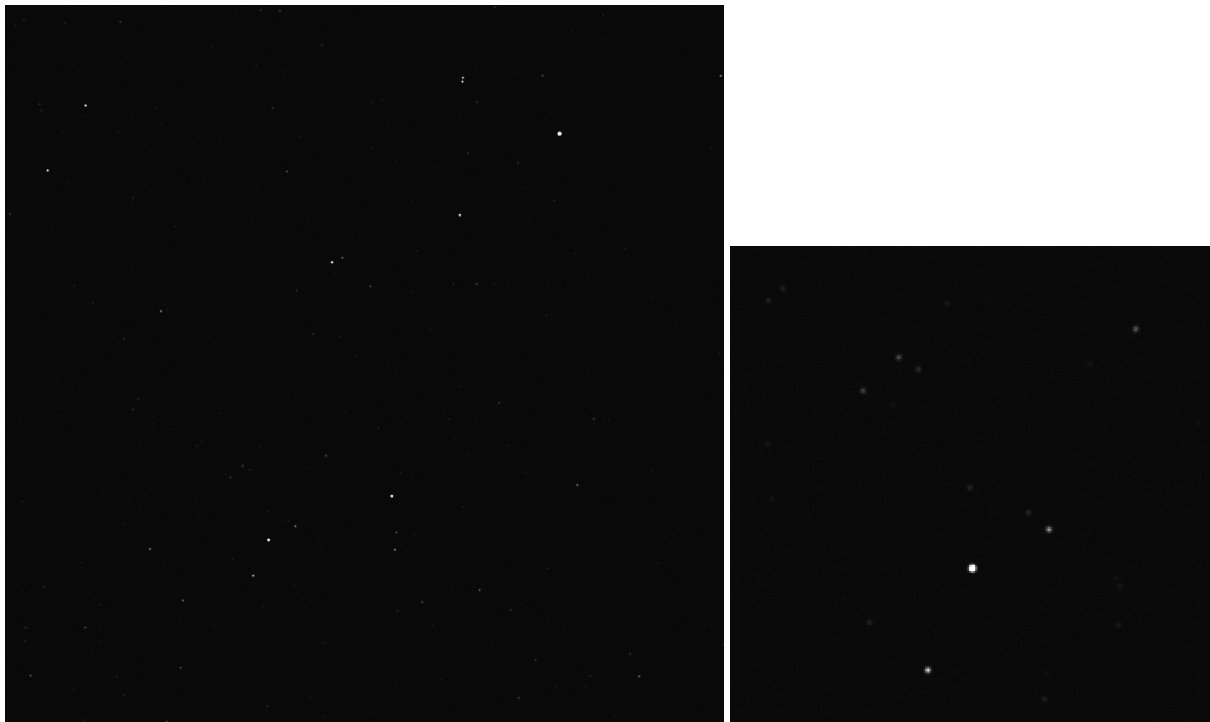
Figure 5.10: This figure shows the Effective Surface Temperatures of the star simulated. This output shows the photometric parameters of the detected star for research purposes. The *black line* in the middle represents the average value of stars temperature in the scene.



(a) This image represents the simulation of the Lira Constellation for a narrowed FOV camera, which still shows the constellation entirely. The image is centred in the middle of the constellation to facilitate the observation, and the brightest star in the up-right corner is Vega.

(b) This image shows a zoom of one corner of the Lira constellation, which allows to observe the details of a particular pattern of stars, as well as the effect of a greater PSF in the simulation. .

**Figure 5.11:** These images are the outputs of the star image simulator, which represent the simulation of an image acquisition of the modelled camera for the selected scenario, without noises modeling. The image on the left represents the full-size image. Instead, the image on the right represents zooming in on a particular detail. Note that the images are vertically tilted to simplify the visualization of the images.



(a) This image represents the same simulation of the Lira Constellation of figure 5.11a, but also considering the noises modelling. However, the effects of the noises start to be observable visually since it is modelled a middle level of noise..

(b) This image shows a zoom of the Lira constellation, with the noise modelling included. Thus, start to be observable the different Signal to Noise Ratio (SNR) what respect to the image in figure 5.6b

**Figure 5.12:** These images are the outputs of the star image simulator, which represent the simulation of an image acquisition of the modelled camera for a selected scenario, also considering noises modeling. The image on the left represents the full-size image. Instead, the image on the right represents zooming in on a particular detail. Note that the images are vertically tilted to simplify the visualization of the images.

### 5.3. Third Output Simulation

The third output shows the comparison of an image simulation with a real image retrieved from the NAVCAM of Rosetta Mission, obtained from [4]. Thus, this comparison shows a scenario for which the simulator is well suited, so the simulation of a multipurpose camera, and gives the possibility to see the differences between the model applied and a real image. In fact, the Rosetta NAVCAM has provided, for navigation purposes, images of star-fields, extended-sources, and celestial objects surfaces, as those reported in figures 5.13.

For this simulation are used the specific parameters of the Rosetta NAVCAM, which also uses the CCD47-20 sensor, are listed in table 5.4. These parameters are retrieved from multiple sources, such as the image description and the reference papers of the camera [26], [27]. In particular, the background noise source is directly retrieved from the image itself, using the PixInsight software. It is worth pointing out that this output shows only the images simulated with the presence of noise, discarding the figure without noise, which are used for a qualitative comparison with the real images.

Thanks to this comparison, it is possible to determine which are the main simplifications of this simulator with respect to real images. In particular, the Rosetta NAVCAM image, named from the source "*ROS – CAM1 – 20140513T202033C*" [4], is a calibration image of the sensor which points towards the star target *Zeta Cas*, a star near the Cassiopeia constellation. The data of this image help us to understand the particular background noise conditions, in fact, this scene was observed during the "PRELANDING MTP003" phase, which means during the comet rendezvous. This peculiar condition is the reason why is present an high level of stray light noise that comes from the comet itself.

Thus, from the analysis of the figures 5.18 and 5.17, it is possible to notice the absence of noise stripes, given by the Fixed Pattern noises of the camera and not simulated in the output images. In addition, it is easy to observe the limitations of the background noise model, which, considering only constant noise, is unable to simulate the stray light progressive diffusion from the comet. Another important difference between the two images is in the model of Point Spread Function, which is simulated following the spread conditions reported in [27], but remain an ideal model that approximates the real geometric aberration of an optical system. Finally, another important difference between the model's output and the real image is the absence, in the model, of fake stars and random defects. In fact, fake stars and random defects, such as burned pixels, are proper of real

image acquisition and are caused by several factors, mainly the presence of cosmic rays or random electronic noises.

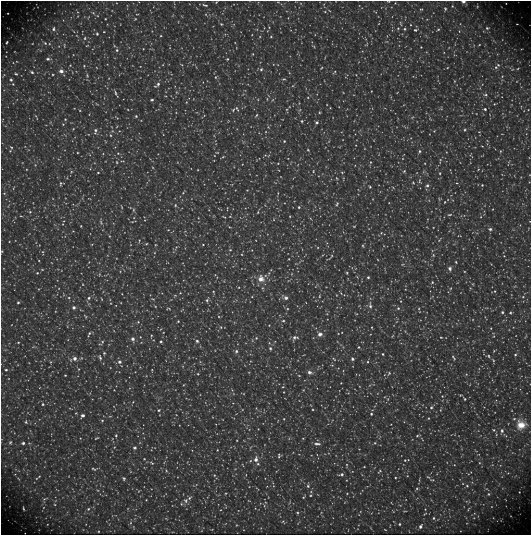
In conclusion, this output gives the possibility to observe several missing features of the simulator, which has to be implemented for a more realistic simulation, as reported in the Future Works section of this thesis.

Parameter	Value
$D_{cam}$	0.07 [m]
$RA_0^*$	9.122 [deg]
$DEC_0^*$	53.817 [deg]
$Gain$	17 [ $\frac{e^-}{ADU}$ ]
$f$	152.5 [mm]
$FOV_{x,y}$	5x5 [deg]
$time$	0.1 [s]
$S_{background}^\dagger$	28000 [ $\frac{e^-}{pixel}$ ]
$\sigma_{PSF}$	0.80 [-]

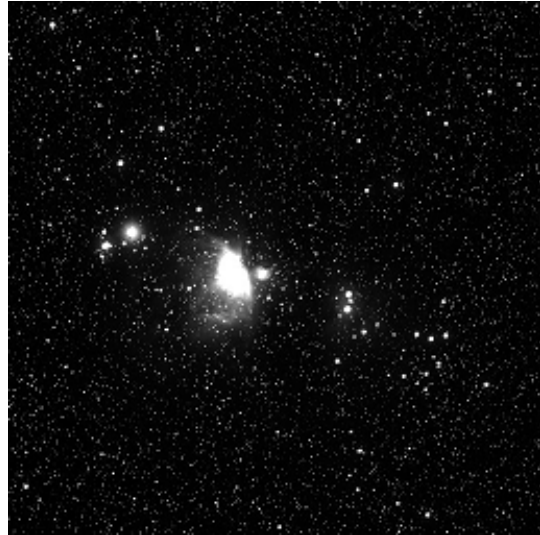
\* Value reported in J2000 convention.

† This value is assumed as an average contribution from several background sources.

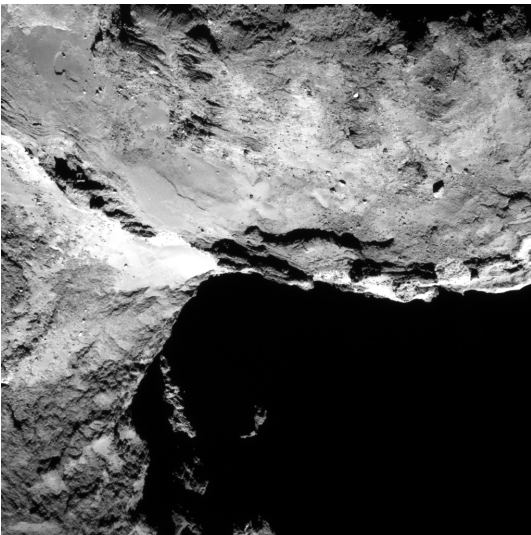
Table 5.4: This table listed the variable parameters of camera models for the Rosetta NAVCAM simulation. Source: data retrieved from images and [26, 27].



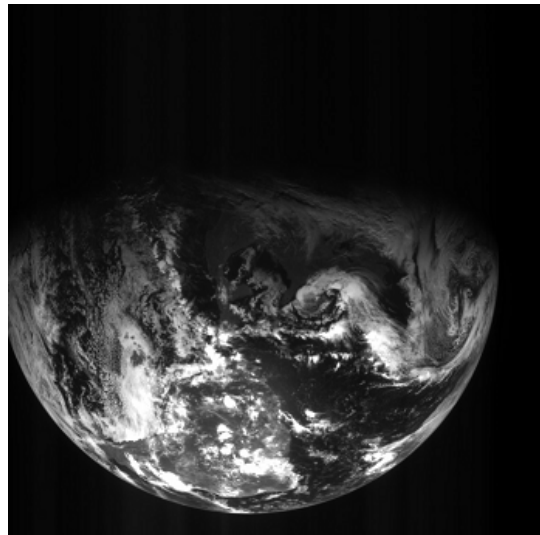
(a) Image acquisition of a stellar target from NAVCAM. It is shown Zeta Cas star, near the Cassiopeia constellation.



(b) Image acquisition of a diffuse target from NAVCAM. It is shown Massier42, nebula in the Orion constellation.



(c) Image acquisition of a space observation target. It is shown 67P/Churyumov comet.



(d) Image acquisition of a planetary observation target. It is shown the Earth from space.

Figure 5.13



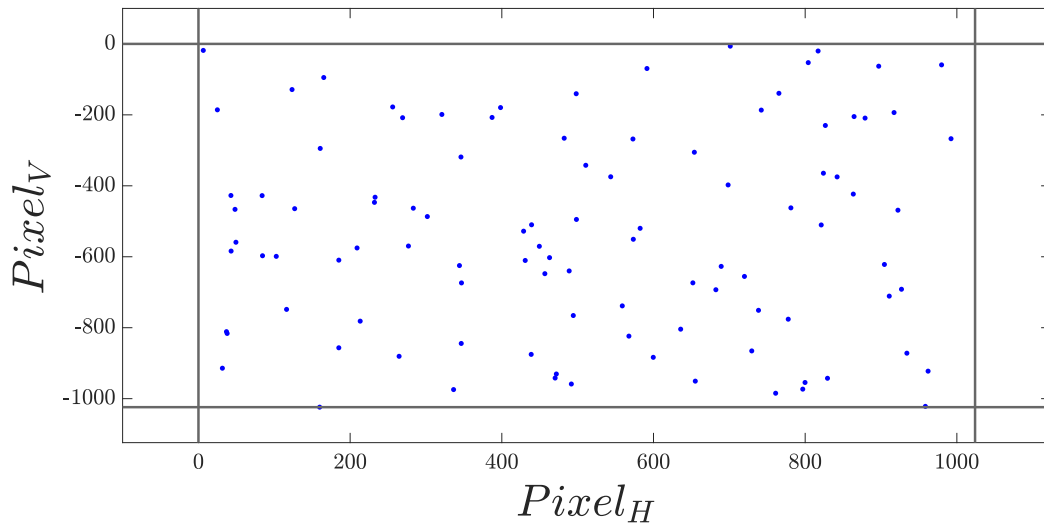


Figure 5.14: This figure shows the centroid stars coordinates (*blue dots*) of the Rosetta NAVCAM image simulation. The black lines represent the limits of the synthetic image.

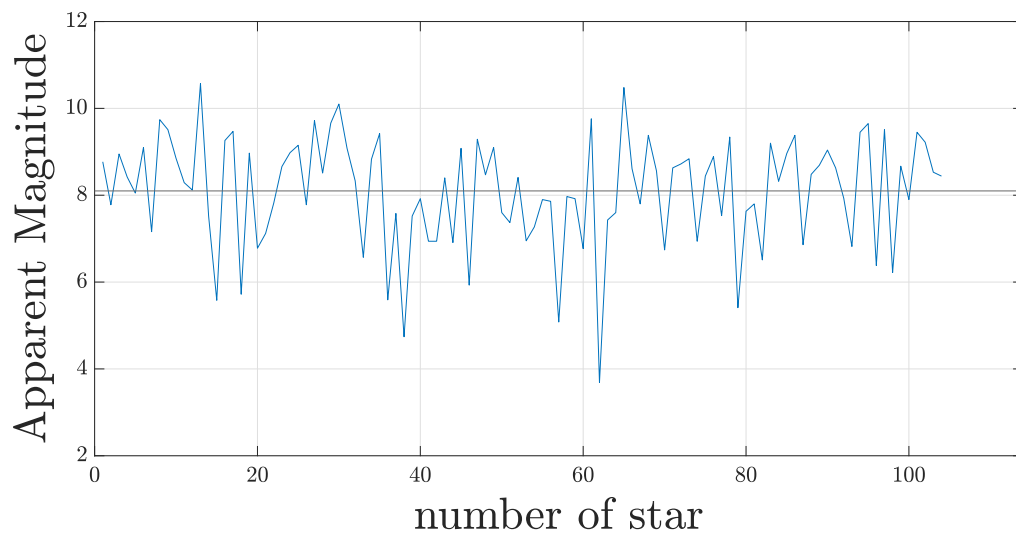


Figure 5.15: This figure shows the visual apparent magnitudes of the Rosetta NAVCAM image simulation. This output shows the photometric parameters of the detected star for research purposes. The *black line* in the middle represents the average value of apparent magnitude in the scene.

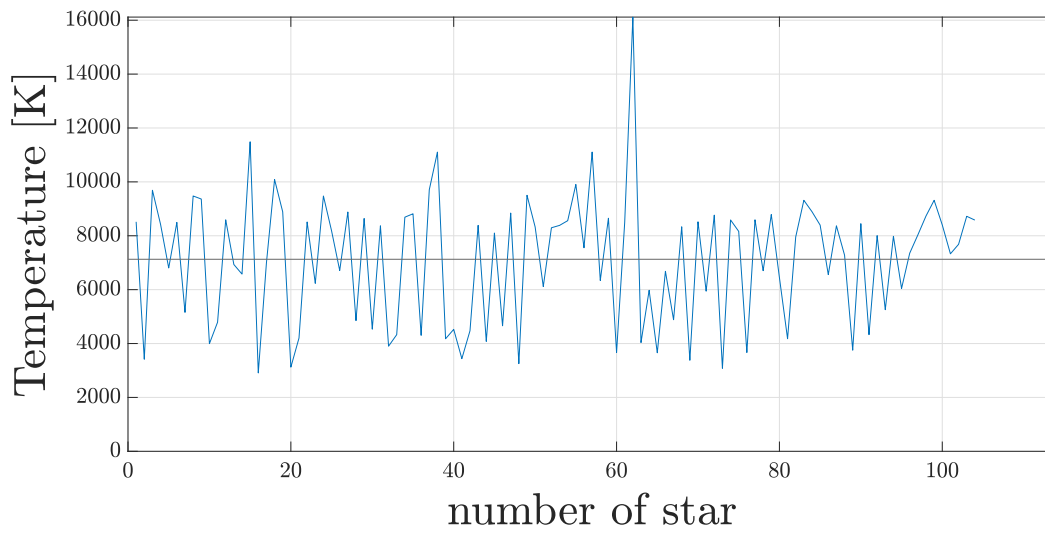
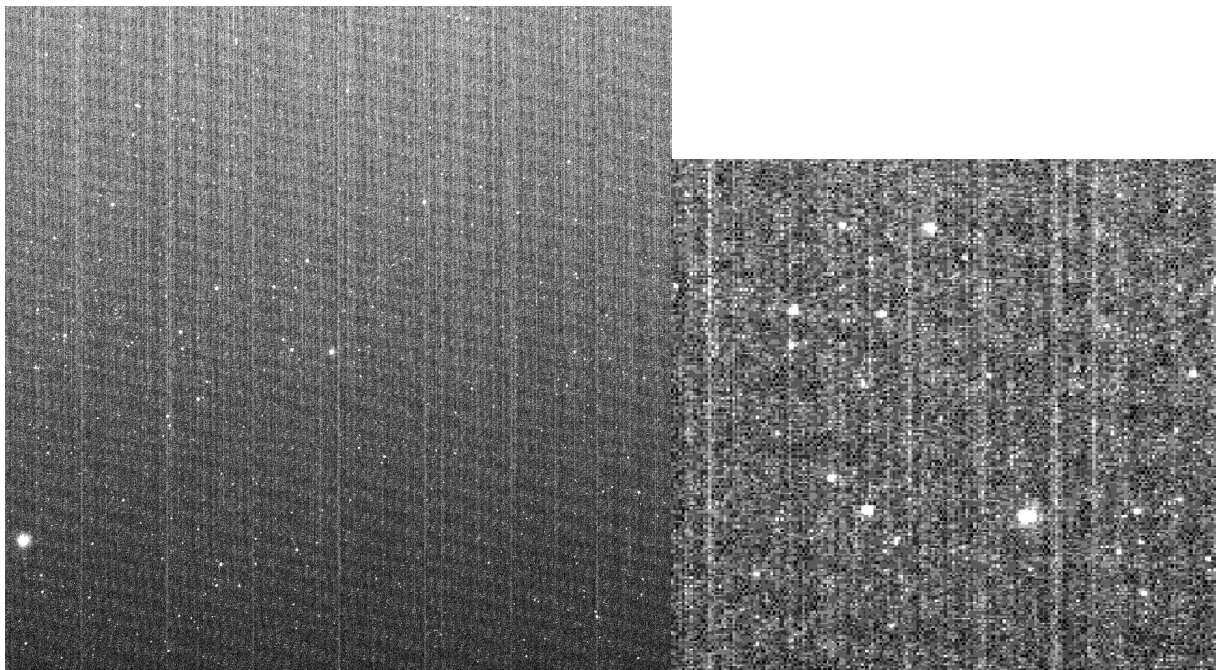


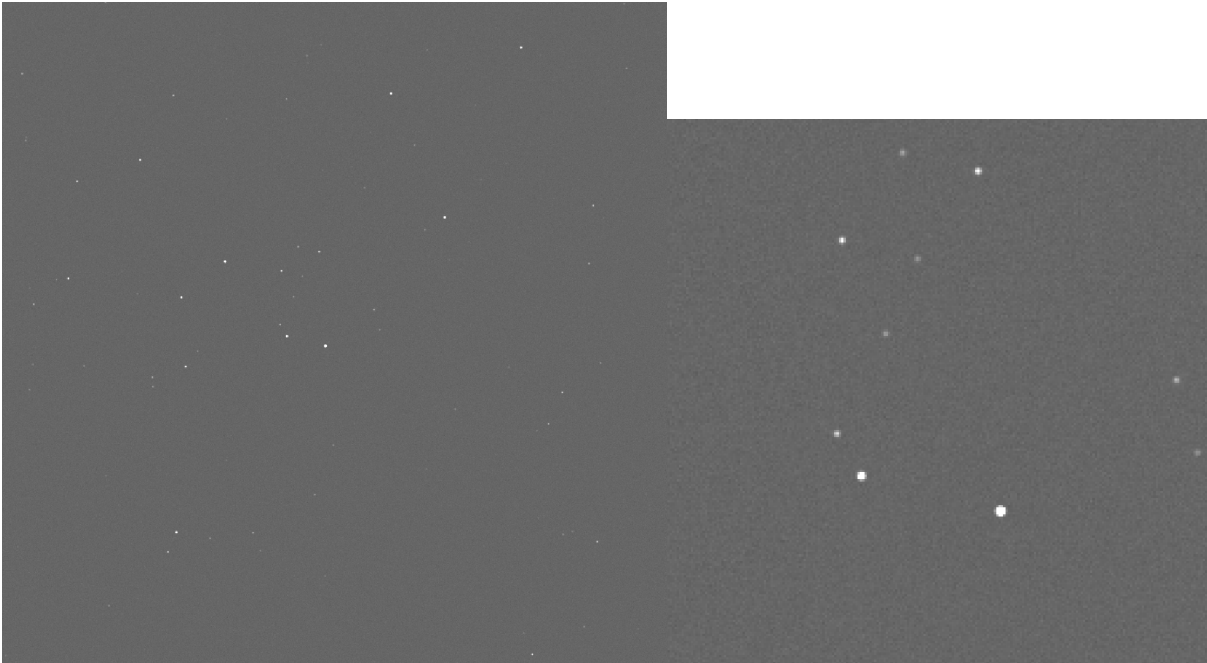
Figure 5.16: This figure shows the Effective Surface Temperatures of the Rosetta NAV-CAM image simulation. This output shows the photometric parameters of the detected star for research purposes. The *black line* in the middle represents the average value of stars temperature in the scene.



(a) This image represents a real acquisition of a star image in space. In particular, it is observed Zeta Cas star, near Cassiopeia constellation, for attitude determination purposes.

(b) This image shows a zoom of the image center, which represents the Zeta Cas star and some easy to recognize stellar pattern on its left.

Figure 5.17: These images are data of the Rosetta mission. The image on the left represents the full-size image. Instead, the image on the right represents zooming in on a particular detail. Note that the images are vertically tilted to simplify the visualization of the images.



(a) This image represents the simulation of Rosetta image acquisition in figure 5.17a. Note that the star patterns are accurately simulated, but the presence of different levels and shapes of background noise makes it difficult to recognize the stars in the entire figure. 5.6a.

(b) This image shows a zoom of the image center, which give the possibility to recognize more easily the same stellar patterns, similar shape of star, and similar differences in the intensity of stars.

Figure 5.18: These images are the outputs of the star image simulator, which represent the simulation of real image acquisition reported in figure 5.17, performed by Rosetta NAVCAM. Thus, this outcome is used to compare the simulator capabilities with respect to a real image. The image on the left represents the full-size image. Instead, the image on the right represents zooming in on a particular detail. Note that the images are vertically tilted to simplify the visualization of the images.

## 5.4. Analysis of Results

In the analysis of the results will be performed a quantitative analysis of the results of the DGS model for star brightness compared with the most known model AGS, commonly used for most of the star image simulator application, as reported in [33]. It is worth pointing out that the final analysis of a star image simulator should include a validation test through real application experiments, data, or well known results. However, this kind of validation process was not performed for this work, as reported in the Conclusion chapter, and will be included in the Future Works of this thesis.

The performed analysis involved the output computation of the DGS and AGS models for the same camera parameters, following the procedures explained in sections 3.5 and 3.1. Once the same output is computed, three equations are developed to compare how the integral computation of the spectral parameters influences the results with respect to the constant selection of average parameters.

In particular, these computations offer the possibility to evaluate individually the improvements that the DGS model offers against the most common and diffuse AGS model, which considers only linear and constant parameters. The three equations are summarized here:

- In equation 5.1 is performed the comparison between the flux densities of the two methods, named  $RAPP_1$  and evaluated in  $[\frac{W}{m^2.s}]$ . Where,  $F_m(\lambda)$  represents the DGS model for the flux density evaluation, reported in equation 3.12;  $F_{m,AGS}$  represents the AGS model for the flux density evaluation, reported in equation 3.16 ;  $\lambda_1$  and  $\lambda_2$  represent, respectively, the minimum and maximum wavelengths of the camera sensor detection, evaluated in  $[m]$ .
- In equation 5.2 is performed the comparison between the photon flux densities of the two methods, named  $RAPP_2$  and evaluated in  $[\frac{photon}{m^2.s}]$ . Where,  $\frac{\lambda}{hc}$  represents the photon energy evaluation, used to convert energy of the detectable flux densities to photons;  $\frac{\lambda_{avg}}{hc}$  represents the constant average evaluation of photon energy, where  $\lambda_{avg}$  is typically the average wavelength of sensor detectable range evaluated in  $[m]$ .
- In equation 5.3 is performed the comparison between the photoelectron flux densities of the two methods, named  $RAPP_3$  and evaluated in  $[\frac{e^-}{m^2.s}]$ . Where,  $QE(\lambda)$  represents the spectral quantum efficiency of the selected camera;  $\tau_{opt}(\lambda)$  represents the spectral optical transmissivity of the selected lens;  $QE_{avg}$  and  $\tau_{opt,avg}$  are the same properties, but evaluated constant for the entire wavelength range of detection.

$$RAPP_1 = \frac{\int_{\lambda_1}^{\lambda_2} F_m(\lambda) d\lambda}{F_{m,AGS}} ; \quad (5.1)$$

$$RAPP_2 = \frac{\int_{\lambda_1}^{\lambda_2} F_m(\lambda) \cdot \frac{\lambda}{hc} d\lambda}{F_{m,AGS} \cdot \frac{\lambda_{avg}}{hc}} ; \quad (5.2)$$

$$RAPP_3 = \frac{\int_{\lambda_1}^{\lambda_2} F_m(\lambda) \cdot \frac{\lambda}{hc} \cdot QE(\lambda) \cdot \tau_{opt}(\lambda) d\lambda}{F_{m,AGS} \cdot \frac{\lambda_{avg}}{hc} \cdot QE_{avg} \cdot \tau_{opt,avg}} ; \quad (5.3)$$

The value ( $RAPP_1$ ) describes how the DGS model increases the accuracy of the stellar flux density calculation, considering also the star's spectral class. Note that the model by which the spectral class of a star influence its spectral emission is explained in section 3.2. Meanwhile, the ( $RAPP_2$ ) value describes the impact of spectral evaluation of photon energy in flux density conversion rather than using a constant average value, such as in the AGS model. Finally, the value ( $RAPP_3$ ) additionally defines the influence of the spectral evaluation of the camera parameters in the computation of the final image signal. In fact, the final evaluation of the signal is performed through linear parameters in both models, as expressed in equation 3.1 .

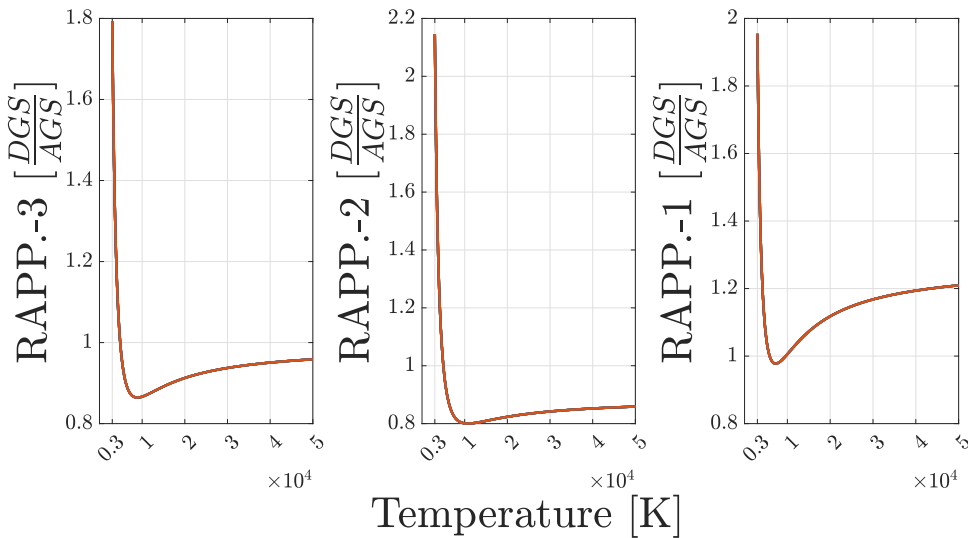


Figure 5.19: These plots represent the comparison analysis between DGS and AGS models as the Effective Surface Temperature of stars changes, for CCD47-20 sensor.

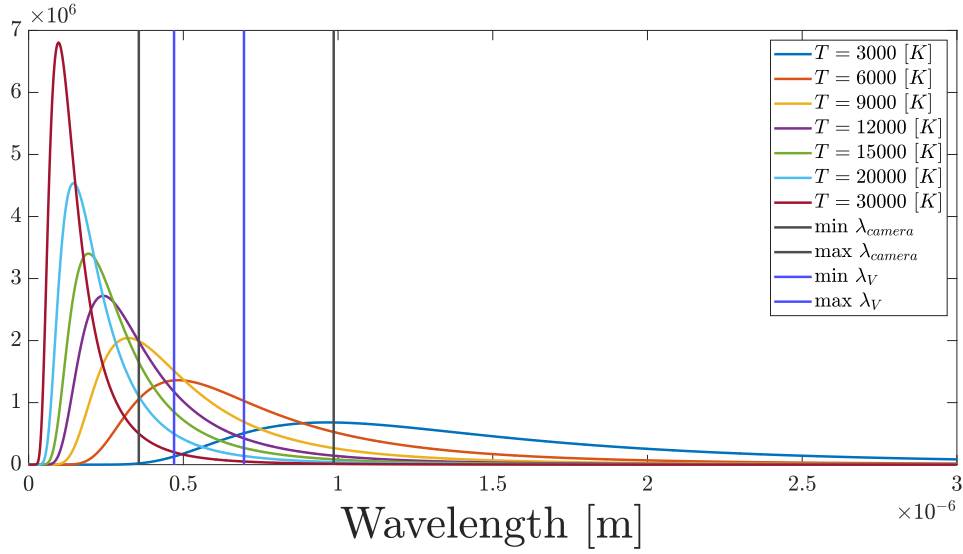


Figure 5.20: This figure shows the various spectral Emittance of stars for different Effective Surface Temperatures. While the *blue lines* represent the Johnson V-band filter wavelengths range and the *black lines* represent the Camera detection wavelengths range.

The results in figure 5.19 show the increase in accuracy of the DGS model, with respect to the AGS model, for the computation of the signal from the star, reported for the range [3000 [K], 50000 [K]] of star temperature measurement (see section 3.3). In particular, it is possible to see that the DGS model provides significantly different values for stars with a surface temperature lower than 5000 [K]. Instead, for stars with surface temperature higher than 9000 [K], there is a slight progression to have results that differ from 15% up to 5%.

The primary motivation for these results is visible in figure 5.20, where the normalized Spectral Radiance of stars at different temperatures are reported, which are explained in section 3.2. In fact, since the Spectra Radiance outlines the spectral emission shape of the stellar flux density, it is possible to see how it behaves in the wavelength detection range of the camera and in the wavelength range of the Johnson V filter, by which are defined the apparent magnitudes of the stars. Thus, it is important to underline three factors that contribute to the high-fidelity of the DGS model:

- The first consideration is that the DGS model can accurately evaluate the proportion between the reference star defined for the visual magnitude measurement system, defined in section 3.4, and the simulated star. In fact, considering the different spectral energies of each star, it is possible to evaluate the exact flux density proportions between the two measured stars.

- The second consideration is that the DGS model is capable of accurately evaluating the spectral flux densities of stars, which also affect the precision of the stellar energy computation over the wavelength detection range of the camera. Indeed, each spectral class of stars radiates differently in a fixed wavelengths range, this means that the temperature of stars will affect the energy that is available for the wavelengths considered.
- The third consideration is that the DGS model can perform the computation with camera spectral properties, which means that the camera device's different photon detection and conversion capabilities will affect the final value of the signal and the differences with the AGS model.

Note that the spectral camera parameters, and their relative averaged values for AGS model, are the same provided for the computation of the output results. Thus, the sensor CCD47-20 and the BK7 optical glass, reported in figures 5.1 and 5.2, are provide to perform this analysis of results.

It is fundamental to underline that the selection of camera spectral parameters produces very significant differences in the DGS model. In fact, the computation of the results analysis for a different camera, which differs only from the spectral Quantum Efficiency, reported in figure 5.21, produces a distinct variation in comparison with the AGS model. In particular, the different behaviour is shown in figure 5.22. The main difference introduced with the new spectral Quantum Efficiency is the non-symmetrical detection capabilities over the wavelengths range<sup>1</sup>. This characteristic mainly influences the behaviour of the DGS model, which respects the AGS one, for stars with surface temperatures higher than 9000 [K]. In fact, for this region, the spectral energy radiated from the star is more sensible to the camera detection capability. Further differences are noted in the maximum intensities of the value ( $RAPP_3$ ), which are lower with respect to the previous computation. This effect is mainly produced by the overall lower capacity of the KAI4021 sensor to detect photons at any wavelength. Instead, the values ( $RAPP_1$ ) and ( $RAPP_2$ ) do not show any difference from the previous computation since the spectral parameter of the camera does not influence those computations.

---

<sup>1</sup>Note that the boundaries of the wavelength detection range of both the sensors are very similar.



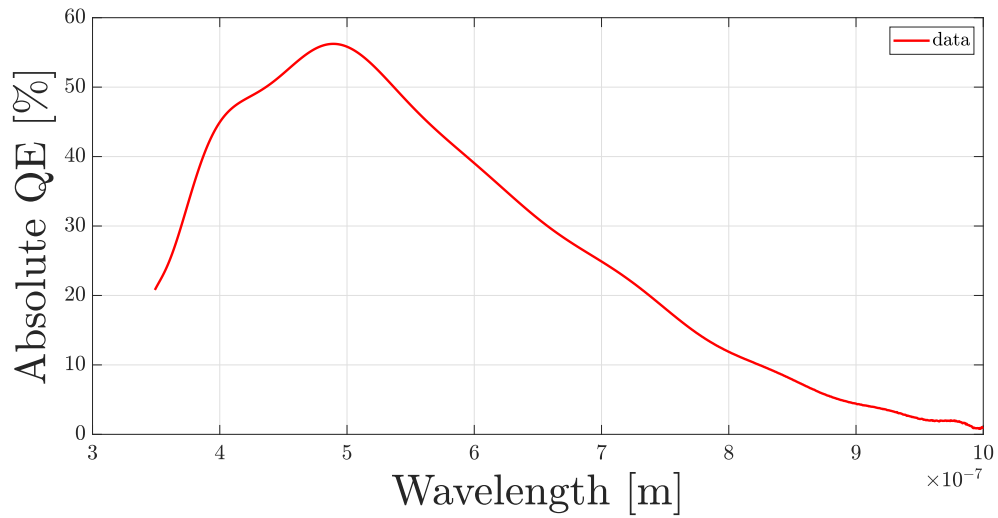


Figure 5.21: This figure shows the Spectral Quantum Efficiency for the KAI4021 sensor. Source: data retrieved from [49]

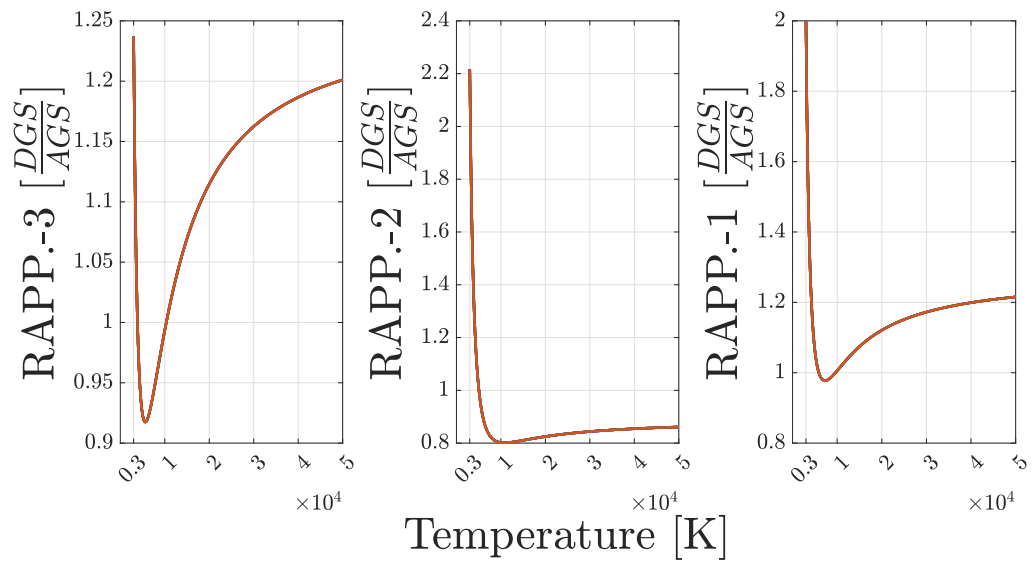


Figure 5.22: These plots represent the comparison analysis between DGS and AGS models as Effective Surface Temperature of stars changes, for KAI4021 sensor.

In conclusion, it is possible to state that the DGS model introduced in this work is capable of performing a high-fidelity computation of the stars' brightness detection, considering the real spectral parameters of the simulated camera and simulated stars.



# 6 | Conclusions and future developments

## 6.1. Final Considerations

This thesis accurately describes all the parameters, procedures and definitions used to implement an original high-fidelity star image simulator, which mainly represents the work in this thesis. Thus, the developed simulator is characterized by an accurate model of star brightness signal computation, which takes into account the effective surface temperature of stars and their specific spectral class radiations emission.

The final result of this work can be properly used to bring forward the research on particular star tracker designs, as well as the common ones, and their algorithms training. Specifically, thanks to the versatility of this simulator, it is possible to test multipurpose camera parameters to perform detailed star image simulations for the purpose of design research and algorithm training for attitude determination.

In particular, the models of this simulator are well suited for the simulation of :

- Detailed Star Image Simulations;
- Image simulations under constant background noise sources;
- Image simulations with various and complex camera parameters;
- Comparison image simulation to detect simple patterns and variables of real image noises.

On the contrary, the models implemented are not suitable for accurate simulations of some scenarios:

- Near Earth observation;
- Celestial objects rendezvous image simulations ;
- Specific space observation simulation, like galaxies of celestial objects surfaces;

- Elevated and complex noise source scenarios.

In general, this work represents an accurate starting point for a complex and realistic star image simulator for several types of cameras. Consequently, it represents a proper baseline for star image simulators that can be expanded based on the specific needs of the process that is necessary to evaluate and simulate. As noted in section 5.4 this simulator does not perform a validation test capable of certifying the complete correctness of the results. Nevertheless, the comparison analysis of the well-known and commonly used AGS model, see references [53, 66, 79], allows to understand the improved accuracy of simulation performed with this work.

## 6.2. Future Works

In this work, there are two main models of simulation, one regarding the stellar simulations and the other regarding the camera simulation.

Considering that the stellar simulations are computed starting from the measurements data of a famous and awarded star catalog, HIPPARCOS catalog, the reliability of this computation is high. However, there are still some strong assumptions and simplifications made to smooth the computation that can be improved and become more realistic. Meanwhile, the camera simulation is also computed starting from reliable data, since are selected almost only manufacturing data reported in camera datasheets, but the models implemented are not accurate for complex noise contribution. In fact, background noise contributions and complex electrical interactions need to be improved to allow a wider range of simulation scenarios.

In general, this simulator needs a validation test to certify the validity of the results. This could be performed through real data images and measurements, such as the Rosetta mission output images, or through several experiments with a well-known camera device. Considering the structure and the characteristics of the implemented models, the best option to proceed with the validation test is through a well-defined camera device, in which it is possible to measure exactly all the camera parameters regarding optical aberrations and distortions, as well as all the camera parameter measurement during the experiment. In fact, the exact definition of sensor temperature, electrical noises behaviour and environment characteristics are needed to perform a simulation with the accurate models of the noises. Another reason to perform this tests, with its own camera, is the possibility to perform several images acquisition to validate as many stars as possible with different photometric parameters.

Specifically, the implementation of models to simulate several typical scenarios in which

star trackers and space observation cameras can operate should be performed to increase the working capability of this simulator. In particular, some priority implementations are:

- The dynamic movements of the camera are actually not considered, but for objects or stars, detection is a very common working situation;
- The model of diffuse celestial objects, like galaxies, nebulae, planets, and moons, are often a source of misunderstanding for star trackers and very common targets for space observation cameras;
- The improvement of the background noise sources, namely the stray light from celestial objects, the planets' atmosphere interaction, the cosmic ray hits, and the random source that produce false star or particular electronic noise;
- The specific optical and geometric aberrations commonly given by the optical heads of a camera are necessary to model the correct projection of the source positions in the simulated images.

Regardless of the unquestionable improvements that the mentioned models could provide to the simulator, some others could be necessary. However, the specific needs of simulation strictly depend on the purpose for which the simulator is used.

In conclusion, the simulator program is designed using MATLAB language, even if the most common programming language to set experiments with physical hardware, in case of hardware-in-the-loop simulations, or to set software simulation of algorithms that will be implemented on physical objects, is commonly the C language, or a language derived from it. Thus, an implementation of this simulator in that programming language should be considered to increase the possible uses of this work.



## Bibliography

- [1] *European Machine Vision Association, EMVA Standard 1288*. Standard for Characterization of Image Sensors and Cameras.
- [2] A. Abarca and A. Theuwissen. A cmos image sensor dark current compensation using in-pixel temperature sensors. *Sensors*, 23(22), 2023. ISSN 1424-8220. doi: 10.3390/s23229109. URL <https://www.mdpi.com/1424-8220/23/22/9109>.
- [3] C. Aerts, J. Christensen-Dalsgaard, and D. W. Kurtz. *Observational Techniques for Asteroseismology*, pages 295–335. Springer Netherlands, Dordrecht, 2010. ISBN 978-1-4020-5803-5. doi: 10.1007/978-1-4020-5803-5\_4. URL [https://doi.org/10.1007/978-1-4020-5803-5\\_4](https://doi.org/10.1007/978-1-4020-5803-5_4).
- [4] Archives ESA. Planetary science archive. URL [https://archives.esac.esa.int/psa/#!Table%20View/NAVCAM%20\(Rosetta\)=instrument](https://archives.esac.esa.int/psa/#!Table%20View/NAVCAM%20(Rosetta)=instrument). Rosetta NAVCAM.
- [5] R. L. Baer. A model for dark current characterization and simulation. In M. M. Blouke, editor, *Sensors, Cameras, and Systems for Scientific/Industrial Applications VII*, volume 6068, page 606805. International Society for Optics and Photonics, SPIE, 2006. doi: 10.1117/12.639844. URL <https://doi.org/10.1117/12.639844>.
- [6] R. L. Baer. A model for dark current characterization and simulation. In M. M. Blouke, editor, *Sensors, Cameras, and Systems for Scientific/Industrial Applications VII*, volume 6068, page 606805. International Society for Optics and Photonics, SPIE, 2006. doi: 10.1117/12.639844. URL <https://doi.org/10.1117/12.639844>.
- [7] M. S. Bessell. Ubvri passbands. *Publications of the Astronomical Society of the Pacific*, 102(656):1181, oct 1990. doi: 10.1086/132749. URL <https://dx.doi.org/10.1086/132749>.
- [8] M. S. Bessell. The hipparcos and tycho photometric system passbands. *Publications of the Astronomical Society of the Pacific*, 112(773):961, jul 2000. doi: 10.1086/316598. URL <https://dx.doi.org/10.1086/316598>.
- [9] M. S. Bessell. Standard photometric systems. *Annual Review of Astronomy and As-*

- trophysics*, 43(1):293–336, 2005. doi: 10.1146/annurev.astro.41.082801.100251. URL <https://doi.org/10.1146/annurev.astro.41.082801.100251>.
- [10] M. S. Bessell, F. Castelli, and B. Plez. Model atmospheres broad-band colors, bolometric corrections and temperature calibrations for O - M stars. 333:231–250, May 1998.
- [11] H. bo Liu, J. chun Tan, H. Jia, X. jian Li, J. qi Wang, and J. kun Yang. Autonomous on-orbit calibration of a star tracker camera. *Optical Engineering*, 50(2):023604, 2011. doi: 10.1117/1.3542039. URL <https://doi.org/10.1117/1.3542039>.
- [12] M. Chen, J. Fridrich, M. Goljan, and J. Lukáš. Source digital camcorder identification using sensor photo response non-uniformity. In E. J. D. III and P. W. Wong, editors, *Security, Steganography, and Watermarking of Multimedia Contents IX*, volume 6505, page 65051G. International Society for Optics and Photonics, SPIE, 2007. doi: 10.1117/12.696519. URL <https://doi.org/10.1117/12.696519>.
- [13] R. Costantini and S. Susstrunk. Virtual sensor design. In N. Sampat, R. J. Motta, and M. M. Blouke, editors, *Sensors and Camera Systems for Scientific, Industrial, and Digital Photography Applications V*, volume 5301, pages 408 – 419. International Society for Optics and Photonics, SPIE, 2004. doi: 10.1117/12.525704. URL <https://doi.org/10.1117/12.525704>.
- [14] L. Dressel. Wide Field Camera 3 Instrument Handbook for Cycle 21 v. 5.0. In *Wide Field Camera 3*, page 5. 2012.
- [15] ESA. ESA website, . URL <https://www.cosmos.esa.int/web/hipparcos/payload>. HIPPARCOS PAYLOAD AND SATELLITE CHARACTERISTICS.
- [16] ESA. ESA website, . URL <https://www.cosmos.esa.int/web/hipparcos/statistics>. HIPPARCOS MEASUREMENTS STATISTIC.
- [17] ESA. ESA website, . URL <https://www.cosmos.esa.int/web/hipparcos/home>. THE HIPPARCOS SPACE ASTROMETRY MISSION.
- [18] ESA. ESA website, June 1997. URL [https://www.cosmos.esa.int/documents/532822/552851/vol11\\_all.pdf/99adf6e3-6893-4824-8fc2-8d3c9cbba2b5](https://www.cosmos.esa.int/documents/532822/552851/vol11_all.pdf/99adf6e3-6893-4824-8fc2-8d3c9cbba2b5). vol.1 - The Hipparcos and Tycho Catalogues MISSION.
- [19] ESA. ESA website, June 1997. URL [https://www.cosmos.esa.int/documents/532822/552851/vol13\\_all.pdf/dca04df4-dc6f-4755-95f2-b1217e539926](https://www.cosmos.esa.int/documents/532822/552851/vol13_all.pdf/dca04df4-dc6f-4755-95f2-b1217e539926). vol.3 - The Hipparcos and Tycho Catalogues MISSION.



- [20] ESA Requirements and Standards Division. ECSS-E-ST-60-Rev.2, Star sensor terminology and performance specification, May 2019. URL <https://ecss.nl/standard/ecss-e-st-60-20c-rev-2-star-sensor-terminology-and-performance-specification-15-may-2019/>
- [21] F. Falchi, P. Cinzano, D. Duriscoe, C. C. M. Kyba, C. D. Elvidge, K. Baugh, B. A. Portnov, N. A. Rybnikova, and R. Furgoni. The new world atlas of artificial night sky brightness. *Science Advances*, 2(6):e1600377, 2016. doi: 10.1126/sciadv.1600377. URL <https://www.science.org/doi/abs/10.1126/sciadv.1600377>.
- [22] M. A. A. Fialho. *Improved star identification algorithms and techniques for monochrome and color star trackers*. PhD thesis, Instituto Nacional de Pesquisas Espaciais São José dos Campos, Brazil, 2017.
- [23] M. A. A. Fialho and D. Mortari. Theoretical limits of star sensor accuracy. *Sensors*, 19(24), 2019. ISSN 1424-8220. doi: 10.3390/s19245355. URL <https://www.mdpi.com/1424-8220/19/24/5355>.
- [24] P. J. Flower. Transformations from Theoretical Hertzsprung-Russell Diagrams to Color-Magnitude Diagrams: Effective Temperatures, B-V Colors, and Bolometric Corrections. 469:355, Sept. 1996. doi: 10.1086/177785.
- [25] D. Futyan, A. Fortier, M. Beck, D. Ehrenreich, A. Bekkelien, W. Benz, N. Billot, V. Bourrier, C. Broeg, A. C. Cameron, et al. Expected performances of the characterising exoplanet satellite (cheops)-ii. the cheops simulator. *Astronomy & Astrophysics*, 635:A23, 2020.
- [26] B. Geiger, M. Barthelemy, and C. Archibald. ROSETTANAVCAM to Planetary Science Archive Interface Control Document. *Planetary Science Archive*, 2016. URL <https://archives.esac.esa.int/psa/ftp/INTERNATIONAL-ROSETTA-MISSION/NAVCAM/RO-C-NAVCAM-3-ESC1-MTP010-V1.0/DOCUMENT/RO-SGS-IF-0001.PDF>.
- [27] B. Geiger, R. Andrés, and T. Statella. Radiometric calibration of the rosetta navigation camera. *Journal of Astronomical Instrumentation*, 10(01):2150004, 2021. doi: 10.1142/S2251171721500045. URL <https://doi.org/10.1142/S2251171721500045>.
- [28] M. Georgiev, R. Bregović, and A. Gotchev. Fixed-pattern noise modeling and removal in time-of-flight sensing. *IEEE Transactions on Instrumentation and Measurement*, 65(4):808–820, 2016. doi: 10.1109/TIM.2015.2494622.
- [29] Glass Dynamics, L.L.C. BK-7 Optical Glass. URL <http://www.glassdynamicsllc.com/bk7.html>. Optical Transmission Range.

- [30] R. Hartley and A. Zisserman. *Multiple view geometry in computer vision*. Cambridge university press, 2003.
- [31] S. S. Hata K. Stanford. URL [https://web.stanford.edu/class/cs231a/course\\_notes/01-camera-models.pdf](https://web.stanford.edu/class/cs231a/course_notes/01-camera-models.pdf). CS231A Course Notes 1: Camera Models.
- [32] G. Healey and R. Kondepudy. Radiometric ccd camera calibration and noise estimation. *IEEE Transactions on Pattern Analysis and Machine Intelligence*, 16(3): 267–276, 1994. doi: 10.1109/34.276126.
- [33] X. M. B. W. X. L. Hongyuan Wang, Zhiqiang Yan and W. Kang. A new high-precision star map simulation model and experimental verification. *Journal of Modern Optics*, 68(16):856–867, 2021. doi: 10.1080/09500340.2021.1955165. URL <https://doi.org/10.1080/09500340.2021.1955165>.
- [34] R. Hornsey. University of waterloo,”. *Noise in Image Sensors*, 1999.
- [35] Q. Hua-Ming, L. Hao, and W. Hai-Yong. Design and verification of star-map simulation software based on ccd star tracker. In *2015 8th International Conference on Intelligent Computation Technology and Automation (ICICTA)*, pages 383–387, 2015. doi: 10.1109/ICICTA.2015.103.
- [36] W. Hubbard. The approximation of a poisson distribution by a gaussian distribution. *Proceedings of the IEEE*, 58(9):1374–1375, 1970. doi: 10.1109/PROC.1970.7939.
- [37] IDS. Star Tracker Datasheet. URL <https://en.ids-imaging.com/store/ui-3180cp-rev-2-1.html>. UI-3180CP Rev. 2.1.
- [38] J. Janesick. *Scientific Charge-coupled Devices*. Press Monographs. Society of Photo Optical, 2001. ISBN 9780819436986. URL <https://books.google.it/books?id=rkgBkbDie7kC>.
- [39] J. Janesick, J. T. Andrews, and T. Elliott. Fundamental performance differences between CMOS and CCD imagers: Part 1. In D. A. Dorn and A. D. Holland, editors, *High Energy, Optical, and Infrared Detectors for Astronomy II*, volume 6276, page 62760M. International Society for Optics and Photonics, SPIE, 2006. doi: 10.1117/12.678867. URL <https://doi.org/10.1117/12.678867>.
- [40] J. Janesick, J. Andrews, J. Tower, M. Grygon, T. Elliott, J. Cheng, M. Lesser, and J. Pinter. Fundamental performance differences between CMOS and CCD imagers: Part II. In T. J. Grycewicz, C. J. Marshall, and P. G. Warren, editors, *Focal Plane Arrays for Space Telescopes III*, volume 6690, page 669003. International Society for

- Optics and Photonics, SPIE, 2007. doi: 10.1117/12.740218. URL <https://doi.org/10.1117/12.740218>.
- [41] J. Janesick, J. Pinter, R. Potter, T. Elliott, J. Andrews, J. Tower, J. Cheng, and J. Bishop. Fundamental performance differences between CMOS and CCD imagers: part III. In P. G. Warren, C. J. Marshall, J. B. Heaney, E. T. Kvamme, R. K. Tyson, and M. Hart, editors, *Astronomical and Space Optical Systems*, volume 7439, page 743907. International Society for Optics and Photonics, SPIE, 2009. doi: 10.1117/12.831203. URL <https://doi.org/10.1117/12.831203>.
- [42] J. Janesick, J. Pinter, R. Potter, T. Elliott, J. Andrews, J. Tower, M. Grygon, and D. Keller. Fundamental performance differences between CMOS and CCD imagers, part IV. In A. D. Holland and D. A. Dorn, editors, *High Energy, Optical, and Infrared Detectors for Astronomy IV*, volume 7742, page 77420B. International Society for Optics and Photonics, SPIE, 2010. doi: 10.1117/12.862491. URL <https://doi.org/10.1117/12.862491>.
- [43] J. Janesick, T. Elliott, J. Andrews, and J. Tower. Fundamental performance differences of CMOS and CCD imagers: part VI. In J. A. Koch and G. P. Grim, editors, *Target Diagnostics Physics and Engineering for Inertial Confinement Fusion IV*, volume 9591, page 959102. International Society for Optics and Photonics, SPIE, 2015. doi: 10.1117/12.2189941. URL <https://doi.org/10.1117/12.2189941>.
- [44] J. R. Janesick. *Photon Transfer: DN to  $[\lambda]$* , volume 170. SPIE Press, 2007. SPIE International Society for Optical Engineering.
- [45] J. R. Janesick, T. Elliott, S. Collins, M. M. Blouke, and J. Freeman. Scientific Charge-Coupled Devices. *Optical Engineering*, 26(8):268692, 1987. doi: 10.1117/12.7974139. URL <https://doi.org/10.1117/12.7974139>.
- [46] J. R. Janesick, T. Elliott, J. Andrews, J. Tower, and J. Pinter. Fundamental performance differences of CMOS and CCD imagers: part V. In R. Widenhorn and A. Dupret, editors, *Sensors, Cameras, and Systems for Industrial and Scientific Applications XIV*, volume 8659, page 865902. International Society for Optics and Photonics, SPIE, 2013. doi: 10.1117/12.2008268. URL <https://doi.org/10.1117/12.2008268>.
- [47] H. Jiang, Y. Xue, G. B. Liu, and X. Y. Fan. Modeling and simulating on star map generation for all-sky. In *Mechanical and Electronics Engineering III*, volume 130 of *Applied Mechanics and Materials*, pages 454–457. Trans Tech Publications Ltd, 1 2012. doi: 10.4028/www.scientific.net/AMM.130-134.454.

- [48] H. L. Johnson. Astronomical measurements in the infrared. *Annual Review of Astronomy and Astrophysics*, 4(1):193–206, 1966. doi: 10.1146/annurev.aa.04.090166.001205. URL <https://doi.org/10.1146/annurev.aa.04.090166.001205>.
- [49] Kodak. Datasheet, January 2006. URL [https://www.1stvision.com/cameras/sensor\\_specs/KAI-4021LongSpec.pdf](https://www.1stvision.com/cameras/sensor_specs/KAI-4021LongSpec.pdf). KAI-4021 image sensor CMOS.
- [50] T. T. Kolehmainen, J. Aikio, M. Karppinen, A.-J. Mattila, J.-T. Makinen, K. Kataja, K. Tukkiniemi, and P. Karioja. Simulation of imaging system’s performance. In M. A. Kahan, editor, *Optical Modeling and Performance Predictions*, volume 5178, pages 204 – 212. International Society for Optics and Photonics, SPIE, 2004. doi: 10.1117/12.504330. URL <https://doi.org/10.1117/12.504330>.
- [51] M. V. Konnik and J. S. Welsh. On numerical simulation of high-speed CCD/CMOS-based wavefront sensors in adaptive optics. In R. K. Tyson and M. Hart, editors, *Astronomical Adaptive Optics Systems and Applications IV*, volume 8149, page 81490F. International Society for Optics and Photonics, SPIE, 2011. doi: 10.1117/12.892667. URL <https://doi.org/10.1117/12.892667>.
- [52] J. Kovalevsky, L. Lindegren, M. a. C. Perryman, P. D. Hemenway, K. J. Johnston, V. S. Kislyuk, J. F. Lestrade, L. V. Morrison, I. Platais, S. Röser, E. Schilbach, H.-J. Tucholke, C. de Vegt, J. Vondrák, F. Arias, A. M. Gontier, F. Arenou, P. Brosche, D. R. Florkowski, S. T. Garrington, R. A. Preston, C. Ron, S. P. Rybka, R.-D. Scholz, and N. Zacharias. The Hipparcos Catalogue as a realisation of the extragalactic reference system. *Astronomy and Astrophysics - A&A*, 323:620–633, 1997. URL <https://hal.science/hal-02053947>.
- [53] Y. Liao, X. Wei, J. Li, and G. Wang. Parameters optimization of image sensor for star sensors. In *2017 IEEE International Conference on Imaging Systems and Techniques (IST)*, pages 1–6, 2017. doi: 10.1109/IST.2017.8261518.
- [54] Y. Liao, X. Wei, J. Li, and G. Wang. Parameters optimization of image sensor for star sensors. In *2017 IEEE International Conference on Imaging Systems and Techniques (IST)*, pages 1–6, 2017. doi: 10.1109/IST.2017.8261518.
- [55] Y. T. Liu. Calculation in Star Charts, May 2023. URL [https://ytliu0.github.io/starCharts/docs/star\\_charts.pdf](https://ytliu0.github.io/starCharts/docs/star_charts.pdf). Publication GitHub Pages.
- [56] E. E. Mamajek, G. Torres, A. Prsa, P. Harmanec, M. Asplund, P. D. Bennett, N. Capitaine, J. Christensen-Dalsgaard, E. Depagne, W. M. Folkner, M. Haberreiter, S. Hekker, J. L. Hilton, V. Kostov, D. W. Kurtz, J. Laskar, B. D. Mason, E. F. Milone, M. M. Montgomery, M. T. Richards, J. Schou, and S. G. Stewart. IAU

- 2015 Resolution B2 on Recommended Zero Points for the Absolute and Apparent Bolometric Magnitude Scales. *arXiv e-prints*, art. arXiv:1510.06262, Oct. 2015. doi: 10.48550/arXiv.1510.06262.
- [57] D. Maneuski, L. Eklund, A. Laing, R. Turchetta, and V. O’Shea. Characterisation of hepaps4—a family of cmos active pixel sensors for charged particle detection. *Nuclear Instruments and Methods in Physics Research Section A: Accelerators, Spectrometers, Detectors and Associated Equipment*, 604(1):404–407, 2009. ISSN 0168-9002. doi: <https://doi.org/10.1016/j.nima.2009.01.096>. URL <https://www.sciencedirect.com/science/article/pii/S0168900209002034>. PSD8.
- [58] M. Marin and H. Bang. Design and Simulation of a High-Speed Star Tracker for Direct Optical Feedback Control in ADCS. *Sensors*, 20(8), 2020. ISSN 1424-8220. doi: 10.3390/s20082388. URL <https://www.mdpi.com/1424-8220/20/8/2388>.
- [59] V. Nardino, D. Guzzi, M. Burrelli, M. Cecchi, T. Cecchi, F. Corti, M. Corti, E. Franci, G. Guidotti, I. Pippi, L. Salvadori, C. Spagnesi, and V. Raimondi. MINISTAR: a miniaturized device for the test of star trackers. In Z. Sodnik, N. Karafolas, and B. Cugny, editors, *International Conference on Space Optics — ICSSO 2018*, volume 11180, page 111807V. International Society for Optics and Photonics, SPIE, 2019. doi: 10.1117/12.2536202. URL <https://doi.org/10.1117/12.2536202>.
- [60] M. a. C. Perryman, L. Lindegren, J. Kovalevsky, E. Høg, U. Bastian, P. L. Bernacca, M. Crézé, F. Donati, M. Grenon, M. Grewing, F. van Leeuwen, H. van Der Marel, F. Mignard, C. A. Murray, R. S. Le Poole, H. Schrijver, C. Turon, F. Arenou, M. Froeschlé, and C. S. Petersen. The Hipparcos Catalogue. *Astronomy and Astrophysics - A&A*, 323(1):49–52, 1997. URL <https://hal.science/hal-02053811>.
- [61] A. Popowicz and B. Smolka. A method of complex background estimation in astronomical images. *Monthly Notices of the Royal Astronomical Society*, 452(1): 809–823, 07 2015. ISSN 0035-8711. doi: 10.1093/mnras/stv1320. URL <https://doi.org/10.1093/mnras/stv1320>.
- [62] REDWIRE. Star Tracker Datasheet. URL <https://redwirespace.com/wp-content/uploads/2023/06/redwire-star-tracker-flysheets.pdf>. Redwire Star Tracker.
- [63] N. Sakaguchi, N. Nakamura, S. Ohsawa, Y. Endo, Y. Matsunaga, K. Ooi, and O. Yoshida. Dark current fixed pattern noise reduction for the 2/3-in two-million pixel hdtv stack-ccd imager, 1997.
- [64] M. A. Samaan, D. Mortari, and J. L. Junkins. Nondimensional star identification

- for uncalibrated star cameras. *The Journal of the Astronautical Sciences*, 54:95–111, 2006.
- [65] V. H. Schulz, G. M. Marcelino, L. O. Seman, J. Santos Barros, S. Kim, M. Cho, G. Villarrubia González, V. R. Q. Leithardt, and E. A. Bezerra. Universal verification platform and star simulator for fast star tracker design. *Sensors*, 21(3), 2021. ISSN 1424-8220. doi: 10.3390/s21030907. URL <https://www.mdpi.com/1424-8220/21/3/907>.
- [66] J. Shen, G. Zhang, and X. Wei. Simulation analysis of dynamic working performance for star trackers. *J. Opt. Soc. Am. A*, 27(12):2638–2647, Dec 2010. doi: 10.1364/JOSAA.27.002638. URL <https://opg.optica.org/josaa/abstract.cfm?URI=josaa-27-12-2638>.
- [67] SSB Downloads. Space Telescope Science Institute, . URL <https://ssb.stsci.edu/cdbs/calspec/>. File, sun-mod-001.fits.
- [68] SSB Downloads. Space Telescope Science Institute, . URL <https://ssb.stsci.edu/cdbs/calspec/>. File, alpha-lyr-stis-008.fits.
- [69] Teledyne. Datasheet, December 2017. URL [https://www.teledyne-e2v.com/en-us/Solutions\\_/Documents/datasheets/4720+aimo+A1A-100041\\_9\\_v1.pdf](https://www.teledyne-e2v.com/en-us/Solutions_/Documents/datasheets/4720+aimo+A1A-100041_9_v1.pdf). CCD47-20 image sensor CMOS.
- [70] Teledyne Website. CCD47-20 Back Illuminated Low Noise Sensor. URL <https://www.teledyneimaging.com/en/aerospace-and-defense/products/sensors-overview/ccd/ccd47-20/>. Mission Heritage.
- [71] H. Wach and E. R. D. Jr. Noise modeling for design and simulation of computational imaging systems. In Z. ur Rahman, R. A. Schowengerdt, and S. E. Reichenbach, editors, *Visual Information Processing XIII*, volume 5438, pages 159 – 170. International Society for Optics and Photonics, SPIE, 2004. doi: 10.1117/12.542258. URL <https://doi.org/10.1117/12.542258>.
- [72] H. B. Wach and E. R. Dowski. Noise modeling for design and simulation of color imaging systems. In *Color and Imaging Conference*, volume 2004, pages 211–216. Society for Imaging Science and Technology, 2004.
- [73] H. B. Wach and E. R. Dowski. Noise modeling for design and simulation of color imaging systems. In *Color and Imaging Conference*, volume 2004, pages 211–216. Society for Imaging Science and Technology, 2004.
- [74] H. Wang, Y. Wang, Z. Li, and Z. Song. Systematic centroid error compensation

- for the simple gaussian psf in an electronic star map simulator. *Chinese Journal of Aeronautics*, 27(4):884–891, 2014. ISSN 1000-9361. doi: <https://doi.org/10.1016/j.cja.2014.03.027>. URL <https://www.sciencedirect.com/science/article/pii/S1000936114000594>.
- [75] Q. Wei and Z. Weina. Restoration of motion-blurred star image based on wiener filter. In *2011 Fourth International Conference on Intelligent Computation Technology and Automation*, volume 2, pages 691–694, 2011. doi: 10.1109/ICICTA.2011.458.
- [76] X. Wei, W. Tan, J. Li, and G. Zhang. Exposure time optimization for highly dynamic star trackers. *Sensors*, 14(3):4914–4931, 2014. ISSN 1424-8220. doi: 10.3390/s140304914. URL <https://www.mdpi.com/1424-8220/14/3/4914>.
- [77] R. Widenhorn, M. M. Blouke, A. Weber, A. Rest, and E. Bodegom. Temperature dependence of dark current in a CCD. In N. Sampat, J. Canosa, M. M. Blouke, J. Canosa, and N. Sampat, editors, *Sensors and Camera Systems for Scientific, Industrial, and Digital Photography Applications III*, volume 4669, pages 193 – 201. International Society for Optics and Photonics, SPIE, 2002. doi: 10.1117/12.463446. URL <https://doi.org/10.1117/12.463446>.
- [78] G. Willmer. European commision, April 2023. URL <https://ec.europa.eu/research-and-innovation/en/horizon-magazine/booming-satellite-market-micro-rockets-are-next-big-thing>. In booming satellite market, micro-rockets are the next big thing.
- [79] Q. Xu, C. Zhao, and X. Li. Stellar radiation modeling and image simulation for airborne daytime star sensor. In *2016 IEEE International Conference on Signal and Image Processing (ICSIP)*, pages 630–635, 2016. doi: 10.1109/SIPROCESS.2016.7888339.
- [80] J. Yan, J. Jiang, and G. Zhang. Dynamic imaging model and parameter optimization for a star tracker. *Opt. Express*, 24(6):5961–5983, Mar 2016. doi: 10.1364/OE.24.005961. URL <https://opg.optica.org/oe/abstract.cfm?URI=oe-24-6-5961>.
- [81] H. Yang, Y. Jin, Y. Hu, D. Zhang, Y. Yu, J. Liu, J. Li, X. Jiang, and X. Yu. Image degradation model for dynamic star maps in multiple scenarios. *Photonics*, 9(10), 2022. ISSN 2304-6732. doi: 10.3390/photonics9100673. URL <https://www.mdpi.com/2304-6732/9/10/673>.
- [82] W. Zhang, W. Quan, and L. Guo. Blurred star image processing for star sensors under dynamic conditions. *Sensors*, 12(5):6712–6726, 2012. ISSN 1424-8220. doi: 10.3390/s120506712. URL <https://www.mdpi.com/1424-8220/12/5/6712>.

